INFORMATION TO USERS

This manuscript has been reproduced from the microfilm master. UMI films the text directly from the original or copy submitted. Thus, some thesis and dissertation copies are in typewriter face, while others may be from any type of computer printer.

The quality of this reproduction is dependent upon the quality of the copy submitted. Broken or indistinct print, colored or poor quality illustrations and photographs, print bleedthrough, substandard margins, and improper alignment can adversely affect reproduction.

In the unlikely event that the author did not send UMI a complete manuscript and there are missing pages, these will be noted. Also, if unauthorized copyright material had to be removed, a note will indicate the deletion.

Oversize materials (e.g., maps, drawings, charts) are reproduced by sectioning the original, beginning at the upper left-hand corner and continuing from left to right in equal sections with small overlaps.

ProQuest Information and Learning
300 North Zeeb Road, Ann Arbor, MI 48106-1346 USA
800-521-0600

NOTE TO USERS

This reproduction is the best copy available.

UMI

Université d'Ottawa • University of Ottawa

PERMISSION DE REPRODUIRE ET DE DISTRIBUER LA THÈSE

PERMISSION TO REPRODUCE AND DISTRIBUTE THE THESIS

NOM DE L'AUTEUR / NAME OF AUTHOR:	GAUTHIER, Michel
ADRESSE POSTALE / MAILING ADDRESS:	10-551 RIVERDALE OTTAWA ON K1S1S3
GRADE / DEGREE:	**ANNÉE D'OBTENTION / YEAR GRANTED**
M.Sc. (Physics)	
TITRE DE LA THÈSE / TITLE OF THESIS:	MODELLING A HIGHLY BIASED RANDOM WALK

L'auteur permet, par la présente, la consultation et le prêt de cette thèse en conformité avec les règlements établis par le bibliothécaire en chef de l'Université d'Ottawa. L'auteur autorise aussi l'Université d'Ottawa, ses successeurs et cessionnaires, à reproduire cet exemplaire par photograhie ou photocopie pour fins de prêt ou de vente au prix coûtant aux bibliothèques ou aux chercheurs qui en feront la demande.

Les droits de publication par tout autre moyen et pour vente au public demeureront la propriété de l'auteur de la thèse sous réserve des règlements de l'Université d'Ottawa en matière de publication de thèses.

The author hereby permits the consultation and the lending of this thesis pursuant to the regulations established by the Chief Librarian of the University of Ottawa. The author also authorizes the University of Ottawa, its successors and assignees, to make reproductions of this copy by photographic means or by photocopying and to lend or sell such reproductions at cost to libraries and to scholars requesting them.

The right to publish the thesis by other means and to sell it to the public is reserved to the author, subject to the regulations of the University of Ottawa governing the publication of theses.

N.B. LE MASCULIN COMPREND ÉGALEMENT LE FÉMININ

10/01/2003

DATE

(AUTEUR) SIGNATURE (AUTHOR)

Université d'Ottawa · University of Ottawa

Université d'Ottawa · University of Ottawa

FACULTÉ DES ÉTUDES SUPÉRIEURES ET POSTDOCTORALES

FACULTY OF GRADUATE AND POSTDOCTORAL STUDIES

GAUTHIER, Michel

AUTEUR DE LA THÈSE - AUTHOR OF THESIS

M.Sc. (Physics)

GRADE - DEGREE

Physics

FACULTÉ, ÉCOLE, DÉPARTEMENT - FACULTY, SCHOOL, DEPARTMENT

TITRE DE LA THÈSE - TITLE OF THE THESIS

Modelling a Highly Biased Random Walk :
Application to Gel Electrophoresis

Gary Slater

DIRECTEUR DE LA THÈSE - THESIS SUPERVISOR

EXAMINATEURS DE LA THÈSE - THESIS EXAMINERS

B. Joos

L. Chen

S. Sundaresan

J.-M. De Koninck, Ph.D.

LE DOYEN DE LA FACULTÉ DES ÉTUDES SUPÉRIEURES ET POSTDOCTORALES

SIGNATURE

DEAN OF THE FACULTY OF GRADUATE AND POSTDOCTORAL STUDIES

Modelling a highly biased random walk: Application to gel electrophoresis

by

Michel Gauthier

A thesis presented to the University of Ottawa
in fulfilment of the thesis requirement for the degree of
Master of Science in Physics

Ottawa, Ontario
January 7, 2003

© Michel Gauthier, Ottawa, Canada, 2003

National Library of Canada
Acquisitions and Bibliographic Services
395 Wellington Street
Ottawa ON K1A 0N4
Canada

Bibliothèque nationale du Canada
Acquisitions et services bibliographiques
395, rue Wellington
Ottawa ON K1A 0N4
Canada

Your file Votre référence

Our file Notre référence

The author has granted a non-exclusive licence allowing the National Library of Canada to reproduce, loan, distribute or sell copies of this thesis in microform, paper or electronic formats.

The author retains ownership of the copyright in this thesis. Neither the thesis nor substantial extracts from it may be printed or otherwise reproduced without the author's permission.

L'auteur a accordé une licence non exclusive permettant à la Bibliothèque nationale du Canada de reproduire, prêter, distribuer ou vendre des copies de cette thèse sous la forme de microfiche/film, de reproduction sur papier ou sur format électronique.

L'auteur conserve la propriété du droit d'auteur qui protège cette thèse. Ni la thèse ni des extraits substantiels de celle-ci ne doivent être imprimés ou autrement reproduits sans son autorisation.

0-612-76526-1

Canada

Abstract

The drift and diffusion motions of biased particles are commonly studied using random walks on lattices. We present a novel theoretical approach that makes it possible to calculate exact mobilities in the presence of lattice obstacles. Several two-dimensional examples are studied and a particular attention is given to separation techniques and how our model can be used to study such devices. We also broach the problems related to the field-dependence of the diffusion coefficient during random walks, and we present new algorithms that remove these difficulties. We develop new Monte Carlo algorithms that make it possible to study both drift and diffusion processes simultaneously, even in presence of very strong fields. Finally, we present two brief discussions about the addition of curved field lines and viscosity gradients to our lattice models. This work opens the door to a wide range of applications, especially for the study of electrophoretic technologies.

Summary

The drift and diffusion motions of biased particles are commonly studied using random walks on lattices. Traditionally, the models used for such studies entail Monte Carlo simulations that allow the researcher to follow the dynamics of millions of particles with a good precision ($\sim 0.1\%$). However, current algorithms are not generally valid for all values of the external force (they are limited to small external fields). In this thesis, we present a novel theoretical approach that makes it possible to calculate exact mobilities in the presence of lattice obstacles. Several two-dimensional examples are studied, including one that includes topological dead-ends that act like traps. A particular attention is given to separation techniques and how our model can be used to study such devices.

We also broach the problems related to the field-dependence of the diffusion coefficient during random walks, and we present new algorithms that remove these difficulties. Current models are often restricted to the calculation of either the mobility or the diffusion coefficient. However, when we are interested in highly biased random walks in the presence of obstacles, these two quantities are needed to correctly describe the dynamics involved. We develop new Monte Carlo algorithms that make it possible to study both drift and diffusion processes simultaneously, even in presence of very strong fields.

Finally, we present two brief discussions about the addition of curved field lines and viscosity gradients to our lattice models. These features are crucial to obtain realistic models for the dynamics of small analytes in microfabricated devices. The work presented in this thesis opens the door to a wide range of applications, especially for the study of electrophoretic technologies.

Sommaire

Les processus de dérive et de diffusion de particules biaisées sont fréquemment étudiés à l'aide de modèles de marche aléatoire sur réseau. Traditionnellement, les simulations de type Monte Carlo, qui permettent de suivre la dynamique de millions de particules avec une grande précision ($\sim 0.1\%$), sont utilisées pour réaliser ce genre d'étude. Cependant, les algorithmes couramment utilisés ne sont pas valides pour toutes les valeurs de la force externe (ils sont en fait limités aux faibles champs externes). La présente thèse présente une approche théorique novatrice qui rend possible le calcul du coefficient de mobilité exact sur réseau en présence d'obstacles. De nombreux exemples bidimensionnels sont analysés, incluant un système comprenant des culs-de-sac agissant comme trappes pour les particules. Nous portons une attention particulière aux techniques de séparation électrophorétiques et à l'application de notre modèle à l'étude de tels procédés.

Nous abordons également les problèmes reliés à la dépendance en champ du coefficient de diffusion durant une marche aléatoire et nous présentons de nouveaux algorithmes nous permettant de surmonter ces contraintes. Les modèles courants sont généralement restreints au calcul soit du coefficient de mobilité soit du coefficient de diffusion. Cependant, ces deux quantités sont nécessaires afin de caractériser correctement la dynamique en jeu lorsque nous nous intéressons aux cas de marches aléatoires fortement biaisées. Nous avons développé de nouveaux algorithmes Monte Carlo qui permettent d'étudier simultanément les processus de dérive et de diffusion et ce, même en présence de champs très forts.

Finalement, nous présentons deux discussions portant sur l'intégration de lignes de champ courbées et de gradients de viscosité dans notre modèle. Ces ajouts sont cruciaux afin d'obtenir un modèle réaliste de la dynamique de petits analytes à l'intérieur d'appareils de séparation opérant à l'échelle microscopique. Le travail présenté dans cette thèse ouvre la porte à de nombreuses applications, particulièrement en ce qui concerne l'étude des technologies de l'électrophorèse.

Statement of originality

The work presented in this thesis is, to the best of my knowledge and belief, new and original. It is my own work, except for Sec. 2.5 where I introduce the calculation technique used in a series of articles published by the group of Dr. Gary. W. Slater during the last 7 years.

The theoretical advances described in this thesis are the fruit of my work during the last two years with the helpful guidance of my supervisor. Also, all analytical and numerical results presented in this thesis were obtained from my own Maple and C++ codes.

The results of chapter 2 to 4 were published in the following journals:

- **M. G. Gauthier** and G. W. Slater "Exactly solvable Ogston model of gel electrophoresis: IX. Generalizing the lattice model to treat high field intensities". *Journal of Chemical Physics* **117**, 6745–6756 (2002).

- **M. G. Gauthier** and G. W. Slater "Calcul exact de la mobilité pour des systèmes avec des conditions frontières périodiques en présence d'un champ externe". *Physics in Canada* **58**, 4, 193–196 (2002).

- **M. G. Gauthier** and G. W. Slater "An exactly solvable Ogston model of gel electrophoresis: X. Application to high-field separation techniques". Accepted by *Electrophoresis*, November 11, 2002 (in press).

We are also currently working on a manuscript about the results presented in chapter 5.

During the last two years, I had the opportunity to communicate the results of my research in the following public communications and conferences:

- **M. G. Gauthier** and G. W. Slater "A Lattice Model of the Ogston regime of gel electrophoresis : Generalization to treat high electric field intensities". Poster presentation at the *Annual meeting of the American Physical Society (APS)*, March 2002, Indianapolis.

- **M. G. Gauthier** and G. W. Slater "A Lattice Model for Gel Electrophoresis". Oral presentation at the *semi-annual graduate student seminars of the Ottawa-Carleton Institute for Physics (OCIP)*, May 2002, Ottawa.

- **M. G. Gauthier** and G. W. Slater "A Lattice Model for Gel Electrophoresis: Exact Calculation of the mobility for systems with periodic boundary conditions under the influence of an external field". Oral presentation at the *Annual meeting of the Canadian Association of Physicists (CAP)*, June 2002, Québec.

Finally, I also had the chance to contribute to two review articles about the theory of electrophoresis written jointly with other students supervised by Dr. Slater:

- G. W. Slater, S. Guillouzic, **M. G. Gauthier**, J.-F. Mercier, M. Kenward, L. C. McCormick and F. Tessier "Theory of DNA Electrophoresis (~1999–2002 ½): a Review". Accepted by *Electrophoresis*, September 4, 2002 (in press).

- G. W. Slater, M. Kenward, L. C. McCormick, **M. G. Gauthier** "Theory of DNA separation by capillary electrophoresis". Submitted to *Current Opinion in Biotechnology*, September 30, 2002.

Remerciements

Je tiens à remercier le Dr. Gary W. Slater pour son soutien tant sur le plan humain qu'académique. Son enthousiasme contagieux et sa curiosité sans borne sont sources de motivation pour tous ceux et celles qui ont la chance de travailler en sa compagnie. Grâce à son encadrement attentif et sa grande patience, je suis convaincu que les deux dernières années passées au sein de son groupe de recherche m'auront permis d'élargir mes connaissances au-delà des objectifs visés par une maîtrise conventionnelle. Je lui en suis extrêmement reconnaissant.

Je me dois également de souligner le support de mes amis et collègues qui m'ont rendu la vie si agréable au cours de ma maîtrise. Je pense notamment à mon grand frère et colocataire Yvan, pour qui j'ai un grand respect. Je réserve aussi un merci particulier à mes amis Jean-François, Martin et Frédéric qui m'ont soutenu durant la réalisation de ce projet.

Un merci spécial à ma mère, à qui je dois beaucoup, dont j'admire la force et l'énergie avec lesquelles elle aborde chaque défi que la vie lui réserve.

Enfin, il faut mentionner que ce projet de recherche a été supporté par des bourses du Conseil de Recherches en Sciences Naturelles et en Génie du Canada (*CRSNG*) et de l'Université d'Ottawa.

Contents

Summary i

Sommaire ii

Statement of originality iii

Remerciements v

Contents vi

List of Figures viii

List of Tables x

1 Introduction 1

1.1 Self-diffusion coefficient in a liquid 1

1.2 Biased random walks and mobility coefficients 3

1.3 Previous work of the Slater group 3

1.4 Presentation of the thesis 7

2 The Generalized Model 9

2.1 The biased random walk in 1D 9

2.2 Extension to 2D systems 10

2.3 Comparison with Brownian Dynamics simulations 14

2.4 Higher dimensions 15

2.5 Calculation of the mobility 17

2.6 Discussion 21

3 Generic Gel Systems 24

3.1 Periodic obstacles 24

3.2 Randomly distributed obstacles 28

3.3 Discussion 38

4 Application to Separation Techniques 42
4.1 The Fundamental Parameters 42
4.2 The Debye Layer 44
4.3 Spatial separations 45
4.4 Angular separations 55
4.5 Jamming in many-particles problems 58
4.6 Discussion 62

5 Diffusion in the Presence of a Drift 66
5.1 Diffusion in one dimension 66
5.2 Time fluctuations with constant time steps in one dimension 69
5.3 Higher-dimensional models 71
5.4 A new set of probabilities 74
5.5 Discussion 80

6 Possible Extensions 82
6.1 Curved field lines 82
6.2 Viscosity gradients 89

7 Conclusions 93

A Maple Code 97

B Negative orthogonal probabilities for $d > 2$ 98

List of Figures

1.1 Schematic representation of gel electrophoresis of charged analytes. 5

2.1 Schematic representation of the discretization of one-dimensional diffusion using a Brownian particle evolving between two absorbing walls. 11
2.2 Scaled mean first passage time T/τ_B and transition probabilities $P_{\pm}$ and $P_{\perp}$ vs the scaled electric field ϵ for a $2D$ system. 16
2.3 Scaled mobility μ_x^* vs scaled electric field ϵ for the example presented in Sec. 2.5. 20

3.1 Obstacle distributions for a periodic gel, a random maze, and a completely random distribution of obstacles. 25
3.2 Scaled mobility μ_x^* vs scaled electric field ϵ for various system sizes $N \times N$. 26
3.3 Scaled mobility μ_x^* vs concentration of obstacles C for periodic distributions of obstacles. 27
3.4 Scaled mobility μ_x^* vs concentration of obstacles C for random maze distributions of obstacles. 30
3.5 Scaled mobility μ_x^* vs concentration of obstacles C for random distributions of obstacles. 33
3.6 Concentrations C^* and C_0 vs scaled electric field ϵ for a pure random distribution of obstacles. 35
3.7 Three different *trap* systems. 37
3.8 Scaled mobility μ_x^* vs scaled electric field ϵ for pure random distributions of obstacles. 37

4.1 Schematic representation of the Debye length λ_D. 45
4.2 Scaled velocities of 1×1 and 2×2 particles in a periodic distribution of obstacles (DC field). 47
4.3 Separation of 1×1 and 2×2 particles in a sieving distribution of obstacles. 49
4.4 The square pulse AC field used in chapter 4. 50
4.5 Scaled velocities of 1×1 and 2×2 particles in a trapping distribution of obstacles (DC field). 51
4.6 Scaled velocities of 1×1 and 2×2 particles in a trapping distribution of obstacles (AC field). 53

4.7 Scaled velocities of 1×1 particles with different charges in a trapping distribution of obstacles. 54
4.8 Scaled velocities of 1×1 and 2×2 particles in a funnelling distribution of obstacles. 55
4.9 Deflection angle of 1×1 and 2×2 particles in a distribution of tilted obstacles (first example). 57
4.10 Comparison of the field-free trajectories of 10000 particles for a free-solution case and a distribution of deflectors. 59
4.11 Deflection angle of 1×1 and 2×2 particles in a distribution of tilted obstacles (second example). 60
4.12 Scaled velocities vs scaled external field for 2×2 particles in jamming and non-jamming distributions of obstacles. 61

5.1 Equations 5.3 and 5.7 (in units of $a^2/2\tau_B$) vs the scaled field ϵ. 68
5.2 (a) Representation of all the possible paths that the particle can follow during a time step τ' if the jumps in all the directions are tried in free-solution. (b) The resulting transition probabilities. 76
5.3 (a) Representation of all the possible paths that the particle can follow during a time step τ' if the jumps in all the directions are tried in presence of an obstacle. (b) The resulting transition probabilities. 78
5.4 Variation of the lattice parameter ξa to study continuum limit ($\xi \to 0$). . . 79
5.5 Scaled mobility μ_x^* vs the mesh size ξ for four different scaled fields ϵ. . . . 79

6.1 The free-solution scaled diffusion coefficients vs the scaled field ϵ for two different values of θ_ϵ. 85
6.2 Illustration of the resulting displacements for two different orientations of the allowed jumps for three different values of the lattice parameter. 86
6.3 Lattice representation of the two continuum limits ($\xi \ll \zeta \ll 1$) with locally curved field lines where both the lattice parameter ξa and the length of a jump ζa are reduced. 88
6.4 Example of a domain structure. The different zones have different viscosity properties. 89

B.1 Probability $P_-(\epsilon)$ (Eq. B.7) vs the probability to stay put, $S(\epsilon)$, for different values of the dimension d and the external field ϵ. 101

List of Tables

3.1 Fitting parameters for the field-dependent mobilities in periodic systems of obstacles. 28
3.2 Fitting parameters for the field-dependent mobilities in random mazes. . . . 31
3.3 Fitting parameters for the field-dependent mobilities in random distributions of obstacles. 34

Chapter 1 Introduction

Random walk based algorithms are commonly used as simulation tools for theoretical studies of a wide range of problems in physics, chemistry and biology. As examples, we can mention the simulation of the motion of Brownian particles, diffusion controlled chemical reactions or the trajectory of a protein in a liquid, and so many others. All the theoretical models used to study these problems share the basic idea of describing a physical process using a probabilistic perspective. Even continuous processes can be studied stochastically using an appropriate discretization of the phenomenon. In fact, the work presented in this thesis treats such a continuous dynamical process: the biased motion of a Brownian particle. More precisely, we will focus our attention on the calculation of the mobility and diffusion coefficients of particles submitted to an external force using discrete random walks on a grid.

1.1 Self-diffusion coefficient in a liquid

In absence of a driving force, a random walker evolving in a viscous medium will move around its initial position due to thermal agitation. This means that if we look at a great number of walkers, the average position will not change with time but the cloud of particles will spherically spread around the starting position. The diffusion coefficient D is the measure of the time evolution of the spatial fluctuations of the particles. Over a long period of time, the behavior of a large population of particles can be described using the *diffusion equation* [1]:

$$\frac{\partial P(x,t)}{\partial t} = D\frac{\partial^2 P(x,t)}{\partial x^2}\,. \tag{1.1}$$

where $P(x,t)dx$ is the probability for a particle to be in the interval between x and $x+dx$ at time t. In more than one dimension, the derivative $\partial^2/\partial x^2$ is replaced by the Laplacian ∇^2.

Solving Eq. 1.1 with for the initial condition $P(x, t = 0) = \delta(x)$ yields to the following result [1]:

$$\langle x \rangle = 0 , \tag{1.2}$$

$$\langle x^2 \rangle = 2Dt , \tag{1.3}$$

where x_0 is the initial position. The one-dimensional diffusion coefficient is then given by [2]:

$$D = \frac{\langle x^2 \rangle - \langle x \rangle^2}{2t} = \frac{\langle \Delta x^2 \rangle}{2t} . \tag{1.4}$$

or

$$\langle \Delta x^2 \rangle = 2Dt . \tag{1.5}$$

In d dimensions, the distance r from the origin is given by $r^2 = x^2 + y^2 + \ldots$ and the diffusion coefficient is thus given by:

$$\langle \Delta r^2 \rangle = \langle \Delta x^2 \rangle + \langle \Delta y^2 \rangle + \ldots = 2dDt . \tag{1.6}$$

In a stationary situation (no external force, no driving current, ...), the spatial fluctuations are controlled by the thermal noise and the frictional force f due to the viscous environment. Detailed calculation of the mean-square displacement starting from the Langevin equation leads to the following fundamental relation [2]:

$$D = \frac{k_B T}{f(R)} . \tag{1.7}$$

where k_B is Boltzmann's constant, T is the temperature and R is the size of the particle. Notice that Eq. 1.7 is a general expression which is not based on assumptions about the shape of the particle. In the case of a spherical particle of radius R, the frictional coefficient is simply given by the Stokes-Einstein relation [2]:

$$f(R) = 6\pi\eta R , \tag{1.8}$$

where η is the solvent viscosity. The self-diffusion coefficient is then given by:

$$D = \frac{k_B T}{6\pi\eta R} . \tag{1.9}$$

Note that for non-spherical objects like polymers, we normally use the hydrodynamic radius R_H, which is an indicator of the apparent size of the object in the solvent.

1.2 Biased random walks and mobility coefficients

Let's now consider the situation in which an external force is applied to the particle. In the steady-state, the particle then moves with a constant drift velocity v given by the ratio of the driving external force F_{ext} and the frictional retardation coefficient $f(R)$ due to the viscosity of the surrounding media [2]:

$$v = \frac{F_{ext}}{f(R)}. \tag{1.10}$$

As an example, we can assume that the particle carries a charge Q, and that an electric field E is applied. For this particular case, the velocity is given by:

$$v = \frac{F_{ext}(Q.E)}{f(R)} = \frac{QE}{f(R)}. \tag{1.11}$$

We now define the mobility coefficient μ, which is the linear relation between the external field E and the corresponding steady-state velocity v [2]:

$$\mu \equiv \frac{v}{E}. \tag{1.12}$$

This last equation, combined with Eqs. 1.7 and 1.11, leads to the *Nernst-Einstein* relation valid for a charged analyte moving in a liquid [2]:

$$D = \frac{k_B T}{Q}\mu. \tag{1.13}$$

1.3 Previous work of the Slater group

In order to better understand the starting point and the motivations of the work presented in this thesis, it is necessary to briefly summarize the work done by the group of Dr. Gary W. Slater on their novel Ogston model of gel electrophoresis.

Free-solution and gel electrophoresis

Electrophoresis is a common technique used to separate and analyze charged particles in solution. In free-solution, charged particles can be dragged by an external electric field with

a drift velocity given by Eq. 1.11. Since this velocity is a function of the particle charge and size, electrophoresis can be used for separation purposes. Generally, electrophoresis is performed in the presence of a sieving medium or gel to increase the separation quality. The collisions of the particles with the gel induce a retardation factor which is function of the analyte's physical properties. It is thus relevant to understand the mechanisms involved in these cases in order to develop new and better separation technologies.

The Ogston Regime

The Ogston regime of gel electrophoresis is key to a number of technologies [3]. This regime corresponds to the situation where the analyte is smaller than the *mean* pore size (R_p) of the sieving medium (see Fig. 1.1). In the case of rigid, globular analytes, this generally means that the particle's radius $R < R_p$. The model is also often used to interpret experimental data for polyelectrolyte molecules such as small DNA molecules; in such cases, the relevant size R is presumably proportional to the mean radius-of-gyration R_g of the polymer. As an example, the recent emphasis on single nucleotide polymorphism (or SNP) [4] analysis means that fairly small DNA molecules must be analyzed very rapidly (i.e., at high field intensitiy) by capillary electrophoresis in entangled polymer solutions: in this situation, separation is probably through Ogston-like sieving. Our understanding of this last situation is embryonic, at best.

The OMRC hypothesis

In a series of articles published during the last 7 years [5, 6, 7, 8, 9, 10, 11, 12], the group of Dr. Slater discussed the traditional Ogston-Morris-Rodbard-Chrambach (OMRC) model [13, 14, 15, 16] of gel electrophoresis in detail. In short, the OMRC model assumes that the electrophoretic mobility $\mu(C)$ of the analyte in a gel of concentration C is, in the $R < R_p$ limit, simply given by the expression:

$$\frac{\mu(C)}{\mu_0} = f(C)\,, \tag{1.14}$$

where $\mu_0 \equiv \mu(C = 0)$ is the free-solution mobility of the analyte and $f(C)$ is the fraction of the total gel volume where the centre-of-mass of the particle can be located without violating

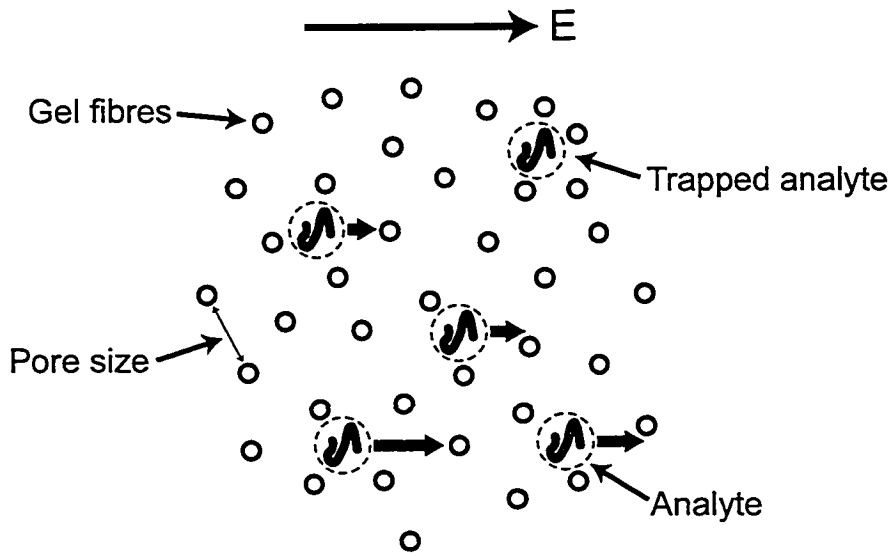

Figure 1.1: Schematic representation of gel electrophoresis of charged analytes. These analytes could be either spherical particles of radius R or macromolecules of hydrodynamic radius R_H.

the condition of volume exclusion between the analyte and the gel fibres. Calculating the mobility is thus reduced to calculating the fractional gel volume $f(C)$ for a given analyte size R and a given gel structure and concentration C. Ogston's calculation of the fractional volume $f(C)$ for a three-dimensional random array of long and thin sticks (the gel) and a sphere (the analyte) provides the simple formula:

$$\frac{\mu(C)}{\mu_0} = \exp\left\{-\frac{\pi}{4} \times \left(\frac{R}{R_p(C)}\right)^2\right\}. \tag{1.15}$$

As we can see, the intensity E of the applied electric field does not enter this theory at all. In fact, the OMRC model is a mean-field model that considers an annealed gel at zero-field intensity.

In the presence of disorder, one would expect to have dead-ends in the gel. In such cases, an analyte with a non-zero size R could get trapped (see Fig. 1.1). In order to continue its net migration in the direction of the applied electrostatic force, it would first have to move against this force and then choose another path. At vanishingly low field intensity ($E \to 0$), this does not involve the thermally activated movement of the analyte above the potential barrier corresponding to the depth of the trap, and the dead-ends should not affect the net

motion of the particle except for their percolation properties. In other words, the dead-ends then lead to a field-independent geometrical contribution to the tortuosity of the pathways taken by the analyte. At high fields, however, the electric forces push the analyte deep inside the dead-ends and the probability of escape should decrease exponentially with the field intensity. The relative contributions of the small probability of falling into such a trap and the large escape times from these traps must then lead to a field-dependent mobility. One thus conclude that the OMRC model is indeed a zero-field model of gel electrophoretic sieving. Another restrictive assumption of the OMRC model is the hypothesis that the field is uniform in the solution.

The Guo-Mercier-Slater model

In the previously mentioned series of articles, a new lattice model of the Ogston regime of gel electrophoresis was introduced. In the low field limit $E \to 0$, this alternative model can be solved exactly (i.e., both the mobility $\mu(C)$ and the fractional volume $f(C)$ can be calculated exactly) for a large variety of gel structures and analyte shapes. The results clearly indicated that Eq. 1.14 is not generally valid. Instead, the following general polynomial expression was suggested:

$$\mu^* \equiv \frac{\mu(C,R)}{\mu_0} = 1 + a_1(R)C + a_2(R)C^2 + a_3(R)C^3 + \ldots \tag{1.16}$$

where μ_0 is the free-solution mobility ($C = 0$). The coefficients $a_{i=1,2,\ldots}$ can then be used to characterize a given sieving system. For example, it was found that the sign of the a_2 coefficient is related to the degree of randomness in the gel while a_1 depends on the sizes of both the analyte and the gel fibres. Note that Eq. 1.14 is in principle included in Eq. 1.16, although it has proven impossible to find any gel-analyte pair for which Eq. 1.16 actually reduced to Eq. 1.14.

However, this lattice model was also restricted to low field intensities. This was explicit in the method used to solve the mathematical matrix equations generated by the model [8, 9, 10, 11, 12]. In particular, it was assumed that the rate at which the analyte jumped from site to site on the lattice remained isotropic and unchanged in the presence of the field. What made this assumption valid was the fact that while the directional bias of the random-walk increases linearly with the intensity E of the external field, the jumping

rate increases only as the square of the field intensity (E^2). In the zero-field limit, one can then neglect the latter because it is of second order. With isotropic jumping rates, the problem can be rewritten simply as linear rate equations whose solution directly leads to an exact value of the zero-field electrophoretic mobility μ. Equivalently, this gives the exact diffusion coefficient D since the Nernst-Einstein (Eq. 1.13) relation establishes a link between D and μ when $E \to 0$ [17, 18, 19]. Thus, the exact calculation technique developed for the zero-field electrophoretic mobility turns out to be an exact calculation method for the equilibrium ($E = 0$) diffusion coefficient as well. The results obtained with this new technique are valid even in the presence of non-conducting fibres which produce curved field lines because the Nernst-Einstein relation must be universally valid at low field intensity [12].

Unfortunately, the situation is far from being trivial when the field intensity is high. The jumping frequency becomes anisotropic (one obviously has more jumps per unit time in the field direction) and the previous approach cannot be used anymore. The zero-field approach is actually equivalent to solving exactly the equations of motion that correspond to a Monte Carlo simulation that would be using the Metropolis algorithm. However, a simplistic use of the latter would fail miserably at high field. For example, let's take a free particle in one dimension. If the field were infinitely high, all the jumps would be in the direction of the field. The velocity would then cease to increase with the field intensity and the diffusion coefficient would be zero. These are two artifacts of the fact that the standard simulation approach only biases the jumps without taking into account the reduced jumping times. In $d \geq 2$ dimensions, one must also consider the anisotropic jumping rates.

1.4 Presentation of the thesis

At the beginning of this project, our main interest was to develop a generalized biased random walk model in order to extend the previously obtained results to any values of the external bias E. Indeed, all the results presented in the series of articles mentioned in the previous section share a common and fundamental limitation: they are only valid in the limit of vanishing external bias ($E \to 0$). In chapter 2, we will derive the biased transition probabilities and jump duration for a random-walk model for all spatial dimensions $d \geq 1$,

compare these dynamical equations with Brownian dynamics simulations, and describe the calculation technique used to obtain exact mobilities. In the following chapter, we will apply this model to generic gel systems in order to study the effect of the bias on sieving properties. Chapter 4 will present specific examples of gels that can be used for separation purposes. The problems related to the calculation of the diffusion coefficients in the presence of a field will be treated in chapter 5. Finally, chapter 6 will discuss two major limitations of our model (the curvature of the field lines and the variation of the viscosity of the surrounding media) and present detailed suggestions on how we can treat such problems.

Chapter 2 The Generalized Model

In this chapter, we will generalize the lattice model previously developed by the group of Dr. Gary W. Slater. This model is only valid in the zero-field limit $E \to 0$. This limitation of the Guo-Mercier-Slater model is the starting point of the work presented in this thesis. We will begin by revisiting the foundations of this model before we propose a major improvement that allows the field to take an arbitrary value. We will also show an example illustrating how to use this new version of the model to compute exact velocities as a function of the applied field intensity. In this thesis, we will treat the case of charged analytes subjected to an external electric field E, but our derivation can also be interpreted in different contexts and, consequently, can be adapted to other kinds of biasing fields.

2.1 The biased random walk in 1D

Consider a charged particle of dimension a diffusing on a one-dimensional (1D) lattice with a lattice parameter a:

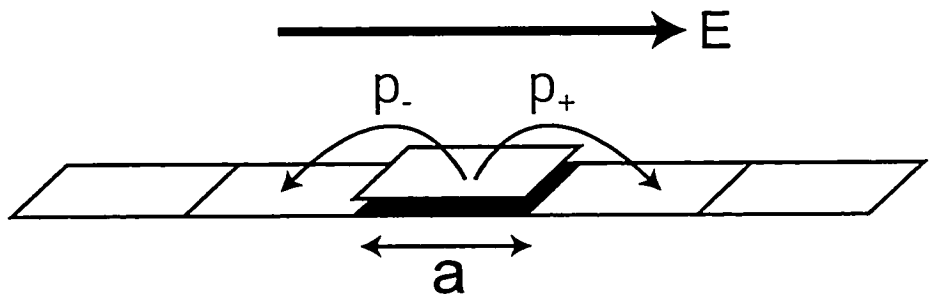

At each step of an unbiased random walk, the particle simply moves to one of the two neighboring sites (noted $\pm x$). In this situation, the transition probabilities are 1/2 for each direction and the mean time duration of a jump is given by the Brownian time $\tau_B \equiv$

The results of this chapter were published in: **M. G. Gauthier** and G. W. Slater "Exactly solvable Ogston model of gel electrophoresis: IX. Generalizing the lattice model to treat high field intensities". *Journal of Chemical Physics* **117**, 6745–6756 (2002).

$a^2/(2D_0)$ (see Eq. 1.4), where D_0 is the free-solution diffusion coefficient of the particle. However, if the random walk is biased by the addition of an external electric field in the $+x$ direction, the mean time duration τ of a $\pm x$ transition is now given by [20]:

$$\tau = \frac{\tanh \epsilon}{\epsilon} \tau_B \,, \tag{2.1}$$

where ϵ is the scaled field intensity given by

$$\epsilon = \frac{QEa}{2k_B T} \,. \tag{2.2}$$

where Q is the charge of the particle, E is the electric field intensity, k_B is Boltzmann's constant and T is the temperature. Note that this transition time is the same in both directions ($\pm$). Finally, the probabilities for the next jump to be in the $\pm x$ direction (noted p_+ and p_- respectively) are given by [20]:

$$p_\pm = \frac{1}{1 + e^{\mp 2\epsilon}} \,. \tag{2.3}$$

It is easy to verify that the normalization condition is respected: $p_+ + p_- = 1$. It is also easy to verify that the mean free-solution velocity (i.e. without obstacles) is then given by:

$$v_0(\epsilon) = \frac{(p_+ - p_-)a}{\tau} = \frac{\epsilon a}{\tau_B} \,. \tag{2.4}$$

for all field intensities, as it should for this type of model. Eqs. 2.1 and 2.3 come from the exact analytical solutions of the first passage problem of a Brownian point-like particle evolving between two absorbing walls (see Fig. 2.1a for a schematic explanation of the process). This exact calculation actually corresponds to the space and time discretization of the continuous one-dimensional displacement of a random walker and it is clearly described in Ref. [20].

2.2 Extension to 2D systems

We now consider a particle of dimension $a \times a$ diffusing on a two-dimensional ($2D$) square lattice. The problem consists now in evaluating the transition probabilities to jump to each of the four adjacent sites (noted $+x$, $-x$, $+y$ and $-y$) while taking into account the fact that the transition time is not the same in the two directions. For example, if the electric

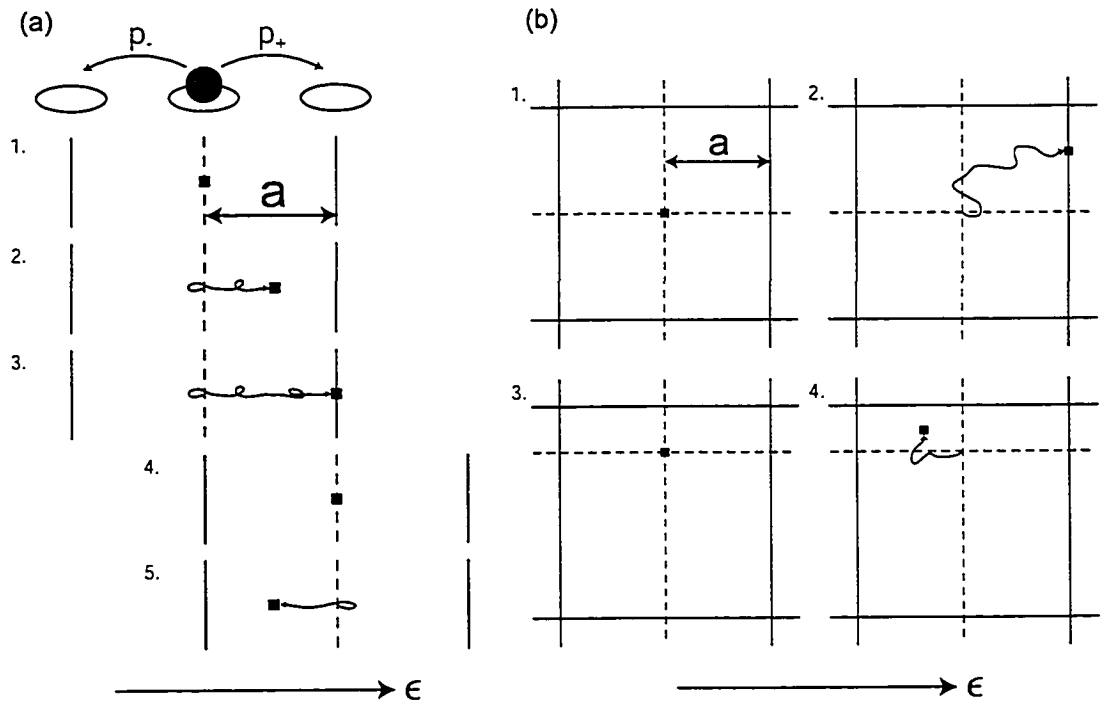

Figure 2.1: (a) Schematic representation of the discretization of one-dimensional diffusion using a Brownian particle evolving between two absorbing walls. The transition time and probabilities can be obtained either exactly or numerically. In the later case, the simulation steps will be the following. (1) The particle is placed in the middle of the two walls, which represent the two neighboring sites. (2) The particle evolves via Brownian Dynamics (Eq. 2.15) (3) until it reaches a wall (which corresponds to a discrete transition to this site). (4) and (5) These steps are repeated starting from the new site. At each iteration, the time duration of the transition and the identity of the wall reached are recorded for statistical purposes.
(b) Same problem as in (a) with a two-dimensional system. Here, only a numerical solution can be obtained. In this case, the simulation steps will be: (1) The particle is placed in the middle of the four neighboring sites (2) and evolves using Eqs. 2.15 and 2.16 until it reaches a wall. The transition time and the identity of the wall reached are recorded. (3) and (4) For the next iteration, the particle is placed back at the center of the box, but only in the direction of the previous step. In other words, the accumulated displacement in the other direction is kept for the next iteration. This is a crucial point, necessary to get the proper dynamics of the particle.

field is applied in the $+x$ direction ($\epsilon_x = \epsilon$ and $\epsilon_y = 0$), the two transition times are then given by (using Eq. 2.1):

$$\tau_x = \left.\frac{\tanh \epsilon_x}{\epsilon_x}\tau_B\right|_{\epsilon_x=\epsilon} = \frac{\tanh \epsilon}{\epsilon}\tau_B = \tau \,. \tag{2.5}$$

$$\tau_y = \left.\frac{\tanh \epsilon_y}{\epsilon_y}\tau_B\right|_{\epsilon_y=0} = \tau_B \,. \tag{2.6}$$

In order to generalize our model to treat high field intensities, we need to rewrite the problem in such a way that all transitions take the same amount of time. Indeed, the use of master equations implicitly requires that all possible jumps are of equal duration. It is thus necessary that this difference between the mean durations of the jumps (Eqs. 2.5 and 2.6) intervenes when we derive the new effective transition probabilities in each of the two dimensions from those previously derived for one dimension. First, it is important to note that we can decouple the x and y directions and evaluate the number of jumps per unit time in each direction. With the electric field applied in the $+x$ direction, the one-dimensional transition probabilities are given by Eq. 2.3 for the $\pm x$ jumps and by $p_{\pm y} = p_\perp = 1/2$ for $\pm y$ jumps (these jumps are not biased because they are orthogonal ($\perp$) to the field). Since the number of jumps per unit time ($\phi_\pm$ and $\phi_\perp$) in each direction are (using Eqs. 2.3, 2.5 and 2.6):

$$\phi_\pm = \frac{p_\pm}{\tau_x} = \frac{1}{\tau(1+e^{\mp 2\epsilon})} \,, \tag{2.7}$$

$$\phi_\perp = \frac{p_\perp}{\tau_y} = \frac{1}{2\tau_B} \,. \tag{2.8}$$

the total number of jumps per unit time (ϕ) is given by:

$$\phi = \phi_+ + \phi_- + 2\phi_\perp = \frac{1}{\tau} + \frac{1}{\tau_B} \,. \tag{2.9}$$

We note that ϕ^{-1} corresponds to the average period of time between jumps, whatever the direction. We will thus use this as the time duration T of all four possible jumps in our modified biased random-walk scheme:

$$T \equiv \frac{1}{\phi} = \frac{\tau\tau_B}{\tau+\tau_B} \,. \tag{2.10}$$

The modified transition probabilities are then given by the product of the various transition rates ϕ with the mean transition time T. This provides the following probabilities:

$$P_{\pm} = T\phi_{\pm} = \frac{1}{(1+e^{\mp 2\epsilon})(1+\tau/\tau_B)}. \tag{2.11}$$

$$P_{\perp} = T\phi_{\perp} = \frac{1}{2(1+\tau_B/\tau)}. \tag{2.12}$$

Note that $P_+ + P_- + 2P_\perp = 1$. We also notice that without obstacles, the free-solution velocity in the direction of the electric field is still given by:

$$v_0 = \frac{(P_+ - P_-)a}{T} = \frac{\epsilon a}{\tau_B}. \tag{2.13}$$

for all field intensities (like Eq. 2.4), a necessary constraint for any model.

Another constraint that our model has to satisfy is the fact that, in a free-solution, the lateral diffusion coefficient (along the y-axis) should not be affected by the presence of an electric field along the x-axis. This could be verified by calculating the net jumping rate in the y-direction:

$$\frac{2P_\perp}{T} = \frac{1}{\tau_B}. \tag{2.14}$$

which is independent of ϵ. So our new probabilities do not affect the rate of lateral transitions and, consequently, the lateral free-solution diffusion coefficient. This is important because lateral diffusion will affect the sequence of collisions with the obstacles in a gel.

Our approach assumes that the electric field lines are parallel to one of the axes, so that the diffusion in the other direction(s) is not affected. This last point is crucial because the generalization of our method to other field orientations (any angle different from 0 or 90 degrees) leads to incorrect conclusions. For example, if we apply the electric field at a 45 degree angle with the x-axis, the transition times and probabilities will be the same in both the x and y directions, and the jumping rates (in both directions) will be a function of ϵ. However, because every displacement then has a component perpendicular to the direction of the electric field, the free-solution lateral diffusion coefficient will also be function of ϵ, which is incorrect. In summary, the only transitions that can be allowed are those that are either parallel or perpendicular to the field lines. For instance, a biased random-walk cannot use a triangular lattice when the field intensity ϵ is non-negligible. However, the limitation

of the lattice representation does not imply a limitation of the systems that we can study. It was previously demonstrated [19] that in the zero-field limit, square and triangular lattices lead to the same results when they are used in the continuum limit (which is the standard procedure to represent realistic systems). The same must be true for finite field intensities.

The aim of our approach is to produce an efficient Monte Carlo algorithm with two different (orthogonal) processes that satisfy two fundamental constraints for free particles: the velocity must increase linearly with the field intensity ϵ for all values of ϵ (we assume that the system remains overdamped and linear), and the lateral diffusion coefficient must remain unaffected by the field. An alternative approach is to choose a time scale τ_f that corresponds to the period of the fastest process and to reduce the probability of acceptance of the slower processes such that their effective rates take the right values. This approach thus adds, in effect, a probability to stay put during a time step of duration τ_f. Instead, our approach is equivalent to distributing the latter probability on all the other processes in proportion to their relative rates. Therefore, the particle makes a jump at each time step, but the mean duration $T < \tau_f$. Our technique is thus more efficient for Monte Carlo simulations: jumps are never rejected, except, of course, if an obstacle is blocking the motion. However, as we will demonstrate in Sec. 2.5, there is no need for Monte Carlo simulations because this stochastic model can actually be solved exactly.

2.3 Comparison with Brownian Dynamics simulations

Contrary to the $1D$ case, we cannot obtain an exact analytical solution of the first passage problem for the $2D$ system. In order to confirm that our equations 2.10 to 2.12 properly represent a discretized version of a continuous process, we used Brownian Dynamics [21] computer simulations to evaluate the probabilities and time durations for a $2D$ first passage problem in a single lattice cell. We studied the $2D$ biased random walk of a particle in a square box of dimensions $2a \times 2a$ with an electric field applied along the x-axis (see Fig. 2.1b). The starting point of the particle was the center of the box and the displacement of the

particle at each time step was obtained from the following equations (dimensionless):

$$\delta x = \delta\tau \times \epsilon + \sqrt{\frac{\delta\tau}{2}} \times \varphi_x(0,1)\,. \tag{2.15}$$

$$\delta y = \sqrt{\frac{\delta\tau}{2}} \times \varphi_y(0,1)\,. \tag{2.16}$$

Here, ϵ is the scaled electric field mentioned previously and $\varphi(0,1)$ is a standard Gaussian probability density function (mean of 0 and variance of 1). We then simulated the displacement of the particle until it reached one of the walls of the box by calculating the displacements δx and δy of the particle during the small time intervals $\delta\tau$. After a wall was reached, the particle was replaced at the center of the box, but only in the direction of this wall. In other words, the accumulated displacement in the other direction was kept for the next iteration. For example, if the particle reached the $+x$ wall with a total displacement $(\Delta x = +a, \Delta y = -a/5)$, the next iteration was started at $(0, -a/5)$ instead of $(0,0)$. This point is very important if we don't want to lose any information about the dynamics of the system when a *jump* is completed. For each completed transition, the identity of the wall reached by the particle as well as the transition time were stored in order to compute average values. With a large statistical sample and a small integration time step $\delta\tau$, the results agree nicely with those of Eqs. 2.10 to 2.12, as we can see in Fig. 2.2. This validates our generalized lattice biased random-walk model because the latter can accurately reproduce the results of lattice-free simulations. In other words, our model properly decouples and discretizes the motion along the x AND y directions.

2.4 Higher dimensions

Our transition probabilities can easily be generalized to systems of higher dimensions. If we work in d dimensions with an electric field applied along one of the cartesian axes, the total number of jumps per unit time becomes:

$$\phi = \frac{1}{\tau(1+e^{-2\epsilon})} + \frac{1}{\tau(1+e^{+2\epsilon})} + \sum_{1}^{d-1}\left(\frac{1}{2\tau_B} + \frac{1}{2\tau_B}\right) = \frac{1}{\tau} + \frac{d-1}{\tau_B}\,. \tag{2.17}$$

So the mean transition time is now given by:

$$T = \frac{\tau\tau_B}{\tau(d-1)+\tau_B}\,. \tag{2.18}$$

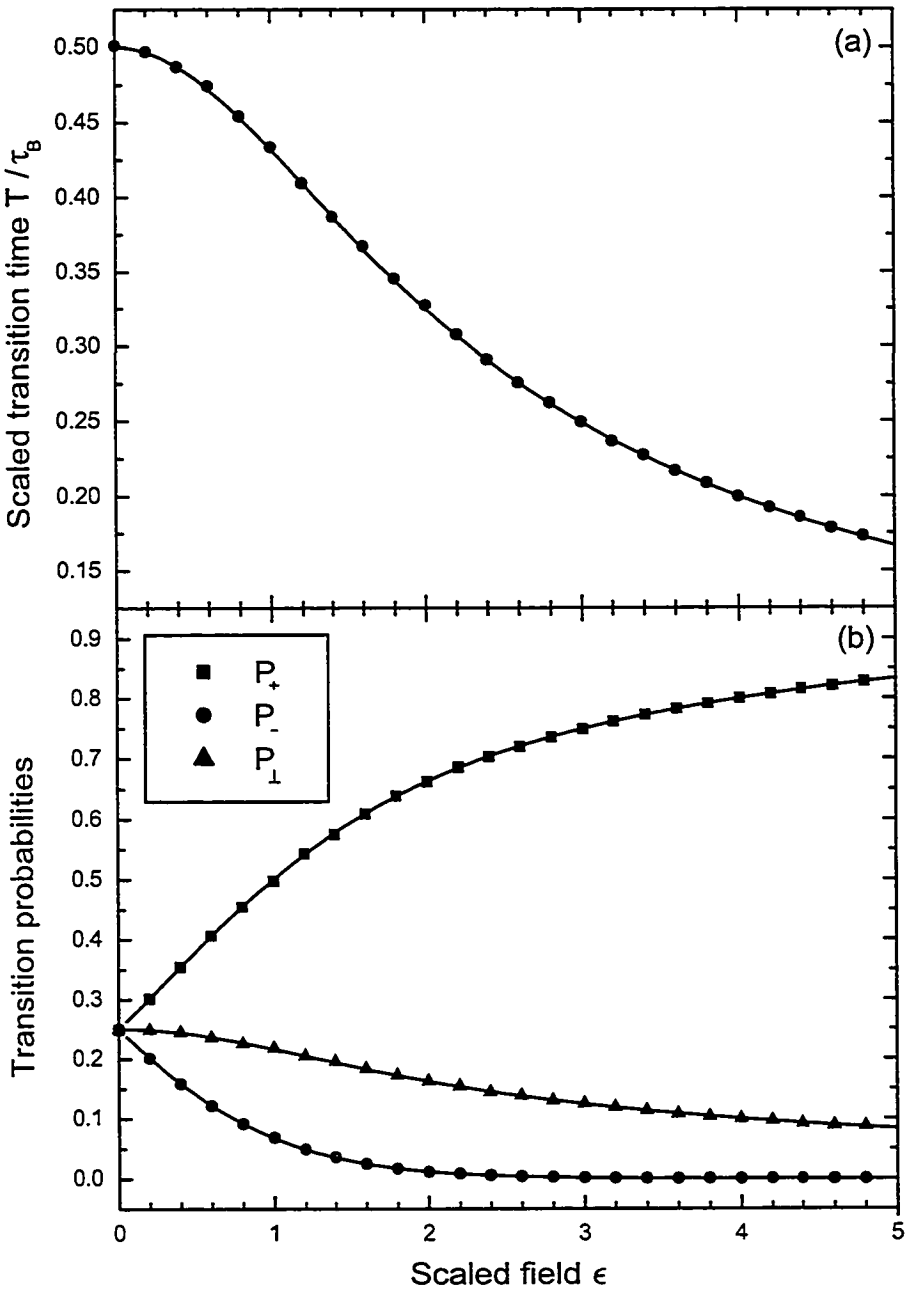

Figure 2.2: Scaled mean firstpassage time T/τ_B and transition probabilities $P_{\pm}$ and $P_{\perp}$ vs the scaled electric field ϵ for a $2D$ system. The solid line in (a) represents Eq. 2.10 and the solid lines in (b) represent Eqs. 2.11 and 2.12. In both (a) and (b), the data points are the results of the Brownian Dynamics simulations. The error bars on the simulation points are smaller than the symbols.

The transition probabilities in the dimension parallel to the electric field ($+x$ for example) are then:

$$P_{\pm} = T\frac{p_{\pm}}{\tau} = \frac{1}{(1+e^{\mp 2\epsilon})(1+(d-1)\tau/\tau_B)}. \tag{2.19}$$

Finally, the transition probabilities in each of the other $d-1$ (orthogonal) directions are:

$$P_{\perp} = T\frac{p_{\perp}}{\tau_B} = \frac{1}{2((d-1)+\tau_B/\tau)}. \tag{2.20}$$

All the results presented in this thesis will be for two-dimensional ($d = 2$) systems.

2.5 Calculation of the mobility

As mentioned previously, the biased random-walk model derived in Sec. 2.2 can be used to carry out Monte Carlo simulations. In this section, we show that it is actually possible to find the exact solution using a mathematical approach similar to the one used in Refs. [5, 6, 7, 8, 9, 10, 11, 12].

General description

To use our transition probabilities and calculate the electrophoretic mobility $\mu(\epsilon) = v(\epsilon)/\epsilon$ (defined in Sec. 1.2), we have to work with a finite-size lattice and periodic boundary conditions (PBCs). The first step is to calculate the steady-state probabilities of presence on each site of the lattice. If there are obstacles, these probabilities are not uniformly distributed unless the field is zero. The second step consists in computing the local velocities on these sites and to use the probabilities of presence to evaluate the mean (weighted) velocity. Lastly, the mobility is obtained from the mean velocity $v(\epsilon)$ and the value of the applied electric field ϵ (see Eq. 1.12).

Example for a simple periodic system

In order to describe our method in detail, we will apply it to the anisotropic system shown in the inset of Fig. 2.3. The obstacles are distributed periodically with periods $\lambda_x = 3a$ and $\lambda_y = 2a$. The periodic cell is thus made of two rows and three columns and it contains one obstacle. The particle moves between five different sites (see Fig. 2.3) under the influence of

the electric field applied along the x-axis. The dynamics can be described by the transition probabilities developed in Sec. 2.2. For example, the probability of presence on site #2 at a certain time $t+T$ is related to the probabilities of presence on the adjacent sites at the earlier time t via the relation:

$$n_2(t+T) = P_+ n_2(t) + P_+ n_1(t) + P_\perp n_5(t) + P_\perp n_5(t)\,. \tag{2.21}$$

where T is given by Eq. 2.10. The first term is due to the reflection on the obstacle and the three others are due to the probability of arriving from the empty adjacent sites (#1 and #5). In the steady-state, the probabilities of presence are independent of the time, so we have $n_i(t+T) = n_i(t) \equiv n_i$. The coupled linear equations for each site $i = 1 \ldots 5$ can then be rewritten as the following matrix equation:

$$A|n\rangle = |n\rangle\,. \tag{2.22}$$

where

$$A = \begin{pmatrix} P_- & P_- & 0 & 2P_\perp & 0 \\ P_+ & P_+ & 0 & 0 & 2P_\perp \\ 0 & 0 & 2P_\perp & P_- & P_+ \\ 2P_\perp & 0 & P_+ & 0 & P_- \\ 0 & 2P_\perp & P_- & P_+ & 0 \end{pmatrix}\,, \tag{2.23}$$

and

$$|n\rangle = \begin{pmatrix} n_1 \\ n_2 \\ n_3 \\ n_4 \\ n_5 \end{pmatrix}\,. \tag{2.24}$$

Note that we use the Dirac notation where $|n\rangle$ and $\langle n|$ represent column and row vectors, respectively, while matrices are denoted by capital letters and scalar by lower case letters. In addition to these equations, our probabilities n_i must satisfy the condition of normalization:

$$\sum_{i=1}^{5} n_i = 1\,. \tag{2.25}$$

This system of equations can easily be solved either analytically or numerically for $|n\rangle$. The exact results, which are ratios of sums of exponentials, are huge and not relevant enough to be presented here. The only result that we will present is the mobility. The local

velocities for the x and y directions are respectively given by:

$$\dot{x}_i = \frac{P_+\sigma_{+i} - P_-\sigma_{-i}}{T}, \tag{2.26}$$

$$\dot{y}_i = \frac{P_\perp\sigma_{+i} - P_\perp\sigma_{-i}}{T}. \tag{2.27}$$

where the displacements are $\sigma_{\pm i} = a$ if there is no obstacle in the given direction and zero otherwise. For our lattice, we thus find the following local velocities, written as column vectors:

$$|\dot{x}\rangle = \begin{pmatrix} \dot{x}_1 \\ \dot{x}_2 \\ \dot{x}_3 \\ \dot{x}_4 \\ \dot{x}_5 \end{pmatrix} = \frac{a}{T}\begin{pmatrix} P_+ \\ -P_- \\ P_+ - P_- \\ P_+ - P_- \\ P_+ - P_- \end{pmatrix}. \tag{2.28}$$

and

$$|\dot{y}\rangle = \begin{pmatrix} \dot{y}_1 \\ \dot{y}_2 \\ \dot{y}_3 \\ \dot{y}_4 \\ \dot{y}_5 \end{pmatrix} = \frac{a}{T}\begin{pmatrix} 0 \\ 0 \\ 0 \\ 0 \\ 0 \end{pmatrix}. \tag{2.29}$$

Finally, the mobilities in x and y are given by the mean velocity ($\sum \dot{x}_i n_i = \langle \dot{x}|n\rangle$ and $\sum \dot{y}_i n_i = \langle \dot{y}|n\rangle$) divided by the scaled electric field ϵ (see Eq. 1.12). Note that in our notation $\langle \dot{x}|n\rangle$ is the scalar product or row $\langle \dot{x}|$ and column $|n\rangle$. For our example (Fig. 2.3), the results are (see Appendix A for the Maple code):

$$\mu_x^*(\epsilon) \equiv \frac{\mu_x(\epsilon)}{\mu_0} = \frac{\langle \dot{x}|n\rangle}{\mu_0\epsilon} = \frac{6\sinh 3\epsilon + 3\epsilon\,(\cosh 3\epsilon + 2\cosh\epsilon)}{8\sinh 3\epsilon + \sinh\epsilon + 5\epsilon\,(\cosh 3\epsilon + 2\cosh\epsilon)}. \tag{2.30}$$

$$\mu_y^*(\epsilon) \equiv \frac{\mu_y(\epsilon)}{\mu_0} = \frac{\langle \dot{y}|n\rangle}{\mu_0\epsilon} = 0, \tag{2.31}$$

where μ_x^* and μ_y^* are the scaled mobilities in the x and y directions, respectively, and μ_0 is the mobility in absence of obstacles:

$$\mu_0 = \frac{v_0(\epsilon)}{\epsilon}\frac{(P_+ - P_-)a}{\tau\epsilon} = \frac{a}{\tau_B}. \tag{2.32}$$

As expected, the mobility in the y direction is zero because there is no net displacement along this direction. Figure 2.3 shows the variation of the scaled mobility μ_x^* as a function of ϵ. The exact asymptotic values are

$$\mu_x^*(\epsilon \to 0) = \frac{27}{40} = 0.675, \tag{2.33}$$

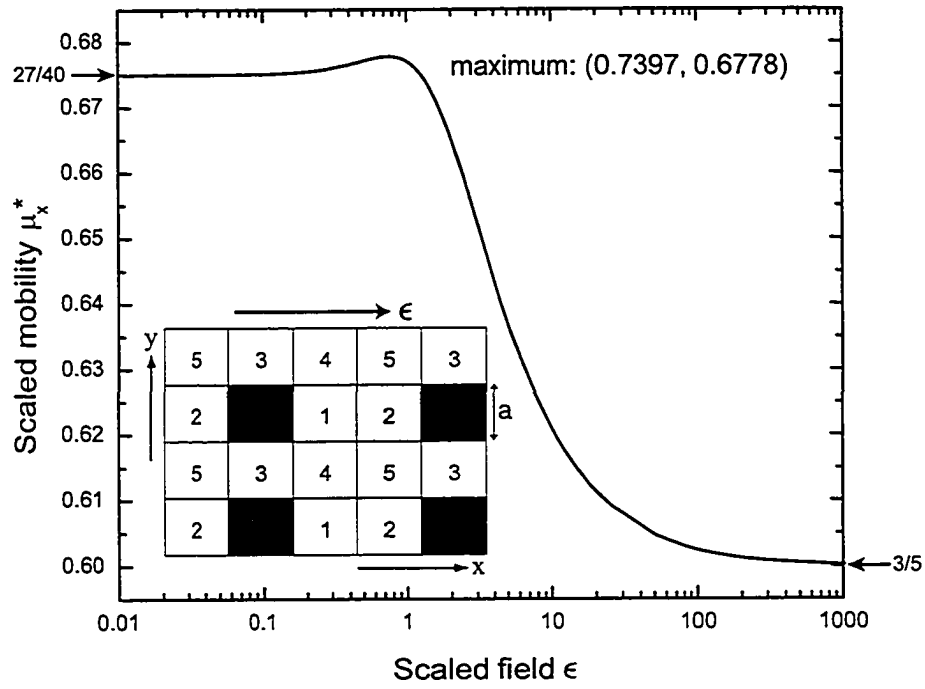

Figure 2.3: Scaled mobility μ_x^* vs scaled electric field ϵ for the example presented in Sec. 2.5 (Eq. 2.30). The labelling scheme used for this example is shown in inset. The filled squares represent obstacles. The analyte can only move between numbered sites. The periodic cell of the lattice contains only 5 sites, as shown in gray.

and

$$\mu_x^*(\epsilon \to \infty) = \frac{3}{5} = 0.6\,, \tag{2.34}$$

as shown. The series expansions of Eq. 2.30 around $\epsilon \to 0$ and $\epsilon \to \infty$ give:

$$\mu_x^*(\epsilon \to 0) \cong \frac{27}{40} + \frac{21}{1600}\epsilon^2 - \frac{1477}{64000}\epsilon^4 + O(\epsilon^6)\,, \tag{2.35}$$

$$\mu_x^*(\epsilon \to \pm\infty) \cong \frac{3}{5} \pm \frac{6}{25}\epsilon^{-1} - \frac{48}{125}\epsilon^{-2} + O(\pm\epsilon^{-3})\,. \tag{2.36}$$

Note that all terms in Eq. 2.35 are even power of ϵ, as expected due to the symmetry of the distribution. Since the second term is positive, the mobility increases with ϵ to reach a maximum value of $\mu_x^* \simeq 0.6778$ at $\epsilon \simeq 0.7397$ (see Fig 2.3). For higher values of ϵ, the mobility smoothly decreases to its asymptotic value of 3/5, as described by Eq. 2.36.

The low field part of this curve can be explained by the fact that when the particle hits an obstacle and then goes around, the probability to hit the next one is slightly lower

due to the field-driven drift (an obstacle masks the next one because they are aligned). We call this very small increase of the mobility (here $\simeq 0.4\%$) the *corridor effect*. At higher field, however, the probability to hit the same obstacle several times before going around it increases with ϵ, and this makes the mobility decrease. This is an artifact of this model (or more precisely, of the geometry of the obstacles) and it is due to the fact that our obstacles are flat: in such a case, the analyte does not roll on the surface of the obstacle and there is no net tangential force that can increase this rolling motion. Instead, an analyte is forced to collide with the same obstacle many consecutive times until a lateral random jump allows it to move beyond the obstacle and continue its journey. However, this obstacle-shape effect is always small ($\lesssim 10\%$).

2.6 Discussion

In this chapter, we have developed a generalized version of the Guo-Mercier-Slater lattice model of gel electrophoresis that includes non-negligible field intensities. This required a fundamental modification to the elements of the model because at high fields the analyte jumping rate is not isotropic anymore. The use of master equations to calculate the probability of presence on each of the lattice sites requires a uniform jumping rate in all spatial directions. Using a field at a 45 degree angle would solve this issue, but we showed that it changes the free-solution diffusion coefficient in the direction transverse to the field (which is incorrect), with a direct effect on the frequency of analyte-obstacle collisions. This approach, which has been used by several authors in the past to carry out Monte Carlo simulations, would at best allow us to study very weak field intensities. Another approach would have been to define a probability S to stay on the same site. If S is chosen to be large enough, modified master equations can again be written and solved using methods similar to the ones used here. Instead, we chose to modify the jumping frequencies and the mean jumping time in order to be able to use $S = 0$. The final mobility results actually do not depend on the value of S (results not shown). Using $S = 0$ allows for much more efficient Monte Carlo simulations to be carried out if such simulation studies are required. The unified jumping rates required by the master equations does not allow us to use stochastic time increments. Such variable time steps are often used in Monte Carlo simulations to

get a realistic physical model [22]. In our particular case, stochastic jumping rates are not needed to calculate the mobility of a particle but might be necessary to study some physical proprieties like the diffusion coefficient. As we will discuss in chapter 5, this problem can be solved if we use a field-dependent probability to stay on the same site ($S = S(\epsilon)$).

We checked the modified jumping rules using Brownian Dynamics simulations and we found that the meaning of discrete jumps in lattice models is rather subtle: discretization of the space into square (or cubic) cells means that one must conserve fractional displacements in the various directions when defining the jumping probabilities and durations. It should be noted that we cannot generalize the model to other lattice structures (such as hexagonal [18]) because of the problem with the transverse diffusion coefficient mentioned previously, but this is not a problem since we will eventually be interested in the continuum limit where the lattice representation is not relevant anymore. We also showed how our model can be used in higher dimensional spaces with the use of hypercubic lattices.

Finally, we want to point out that the time scale derived here is not the same as the one used in the popular repton model of electrophoresis[23]. First, the repton model is based on the Metropolis algorithm and makes assumptions regarding the jump rates and their anisotropy in the presence of an external field. In contrast, our model is a discretization of a continuous process based on a microscopic description of the dynamics on a lattice of square cells. Secondly, the time unit used in the repton model, which is inversely proportional to $\cosh\epsilon$ [23], does not give the proper velocity for a single particle, even in a free solution, if the field is arbitrarily large (as we discussed above, this velocity should always be linearly proportional to the external field ϵ). Indeed, the repton model gives the right velocity only up to the second order in ϵ. Several studies with non vanishing field intensities used this repton model in the past, but we believe that this approach is limited to small values of ϵ (probably $\epsilon \ll 1$). Equations 2.10 to 2.12, on the other hand, clearly make our biased random-walk model valid for arbitrarily high field intensities.

In conclusion, we have derived a generalized lattice model of gel electrophoresis that allows us, for the first time, to study high-field separations. This required several modifications to our previous zero-field model. In order to obtain valid results, one must make sure that the transverse diffusion properties and the free-solution velocity are not affected by the algorithm chosen to represent the field-driven bias. As far as we know, this is the

first tractable model that treats the case of Ogston sieving at non-zero field intensity. This generalization opens the door to many interesting studies where disorder, trapping and nonlinear effects compete in the presence of a high external driving force. We will present several examples of such effects in the next chapters.

Chapter 3 Generic Gel Systems

In this chapter, we will use the calculation technique presented in the previous chapter to study the dynamics of particles in simple generic systems. We will investigate the effect of the field ϵ and the concentration C of obstacles with periodic and random distributions of obstacles. We will thus extend the results previously obtained using the Guo-Mercier-Slater model in the limit of vanishing fields ($\epsilon \rightarrow 0$) to arbitrary values of ϵ. In particular, we will show that we can study trapping problems in random gels, such as the particle trapping effect reported by Serwer *et al.* [24].

3.1 Periodic obstacles

In this section, we investigate the effect of an electric field ϵ on the mobility of a small $a \times a$ analyte in an isotropic system with periodic obstacles and PBC. Our periodic cell is of dimensions $Na \times Na$, where N is the numbers of sites in both the x and y directions, and we have only one obstacle of dimension $a \times a$. The concentration of obstacles is thus given by $C = 1/N^2$. An example for $N = 5$ is showed in Fig. 3.1a.

The exact mobility $\mu_x^*(\epsilon)$ for system sizes N between 3 and 10 is presented in Fig. 3.2 for a wide range of field intensities ϵ. For all concentrations, the scaled mobility starts by increasing slightly with ϵ to reach a maximum value; this is similar to the behavior observed in Fig. 2.3 (barely visible in Fig. 3.2). As the concentration decreases, the amplitude of this maximum also decreases and its position moves towards lower values of ϵ. Remember that the existence of this maximum is due to what we called the *corridor effect* where an obstacle masks the next one on the same row (going around an obstacle reduces the probability to hit the next obstacle). However, as the concentration is reduced, the distance between two

The results of this chapter were published in: **M. G. Gauthier** and G. W. Slater "Exactly solvable Ogston model of gel electrophoresis: IX. Generalizing the lattice model to treat high field intensities". *Journal of Chemical Physics* **117**, 6745–6756 (2002).

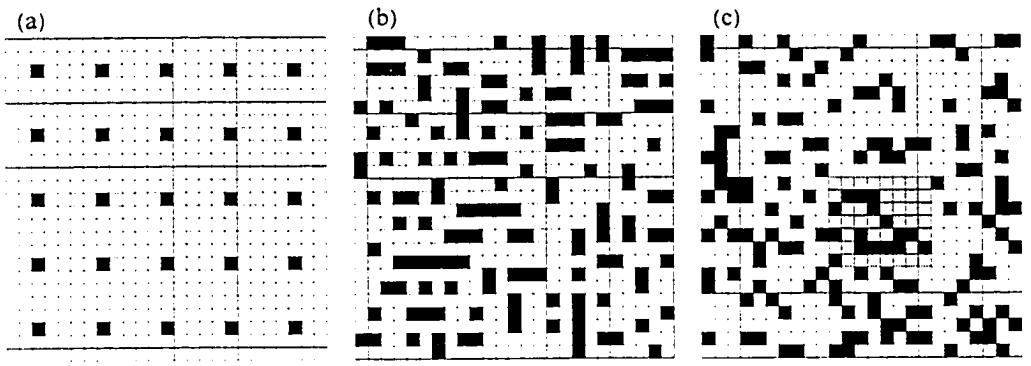

Figure 3.1: Obstacle distributions for a periodic gel (a), a random maze (b), and a completely random distribution of obstacles (c). (a) is a $N = 5$ example of the systems studied in Sec. 3.1, while (b) and (c) are examples of random distributions with 150 obstacles placed on a 25×25 lattice. In (c) we clearly see a trapping region (shaded), the kind of region that we wanted to avoid in (b).

consecutive obstacles increases and the *corridor effect* becomes less important.

Figure 3.2 also shows that the effect of the electric field on the mobility is not very important. In fact, the *artifact* difference between $\mu_x^*(\epsilon = 0)$ and $\mu_x^*(\epsilon \to \infty)$ is always lower than 10%. As $C \to 0$, we expect that $\mu_x^* = 1$ even at high electric field. This can be verified by calculating the asymptotic values of $\mu_x^*(\epsilon \to \infty)$. Results obtained from $N = 3$ to 10 indicate that the mobility at infinite electric field is in fact given by the exact result:

$$\mu_x^*(N, \epsilon \to \infty) = \frac{N(N-1)}{N^2 - 1} = \frac{N}{N+1}, \tag{3.1}$$

which is the ratio between the number of sites in the rows without obstacles and the total number of sites without obstacles. This is due to the fact that, when $\epsilon \to \infty$, the probability $P_\perp$ for the analyte to go from one row to another tends towards zero. So only rows without obstacles then contribute to the effective mobility. In the limit of zero concentration ($N \to \infty$), the rhs Eq. 3.1 is equal to unity, as it should.

The effect of the concentration on the mobility is more clearly presented in Fig. 3.3. This graph shows the variation of the mobility as a function of the obstacle concentration C for different values of ϵ. Previous studies on periodic systems were made in the zero-field limit ($\epsilon \to 0$) [5, 6, 8, 11, 25]. These studies showed that the relation between the mobility

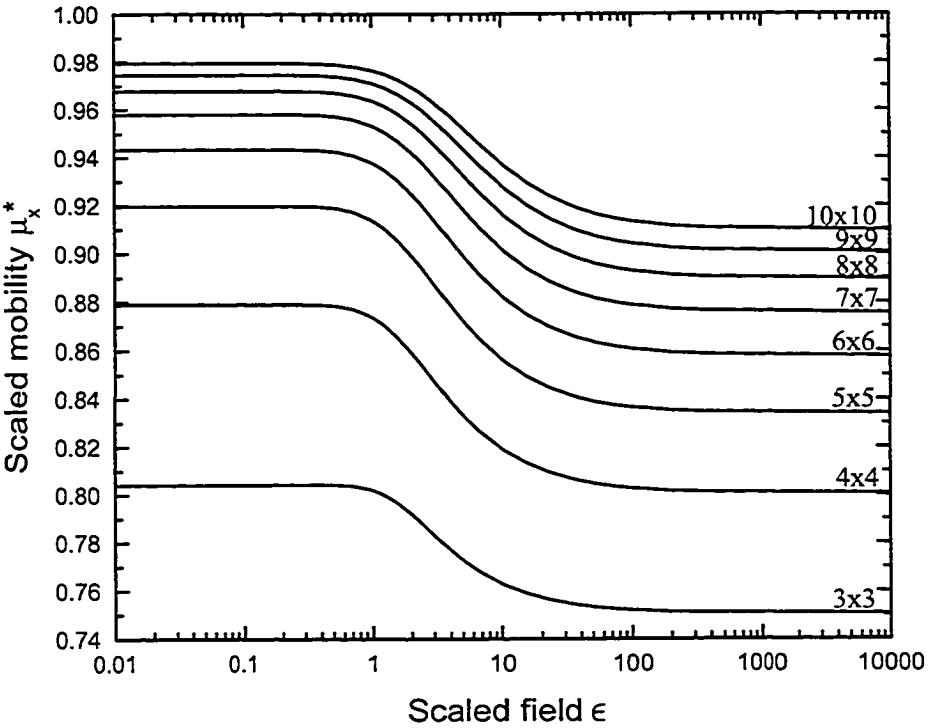

Figure 3.2: Scaled mobility μ_x^* vs scaled electric field ϵ for various system sizes $N \times N$ (as indicated). Each system has a single obstacle, so that the concentration of obstacles is $C = 1/N^2$.

μ_x^* and the concentration C can be expressed as a polynomial function:

$$\mu_x^*(C, \epsilon \ll 1) = 1 + a_1(\epsilon)C + a_2(\epsilon)C^2 + a_3(\epsilon)C^3 + \ldots \tag{3.2}$$

Figure 3.3 shows that although the mobilities decrease at higher fields, the curves remain concave, a characteristic of periodic gels that was discovered previously for $\epsilon \to 0$ [6]. However, the functional form for $\epsilon \to \infty$ is easily obtained from Eq. 3.1 (replacing N by $1/C^{1/2}$):

$$\mu_x^*(C, \epsilon \to \infty) = \frac{1 - C^{1/2}}{1 - C} \simeq 1 - C^{1/2} + C - C^{3/2} + \ldots \tag{3.3}$$

This equation is represented in Fig. 3.3 by the dashed line and we clearly see that it corresponds to the asymptotic curve for increasing values of the electric field ϵ. Strangely enough, Eq. 3.3 shows that the series changes from integer powers of C (see Eq. 3.2) to half-integer powers of C when ϵ increases. This fundamental qualitative change is a direct consequence of the geometric flatness of our obstacles.

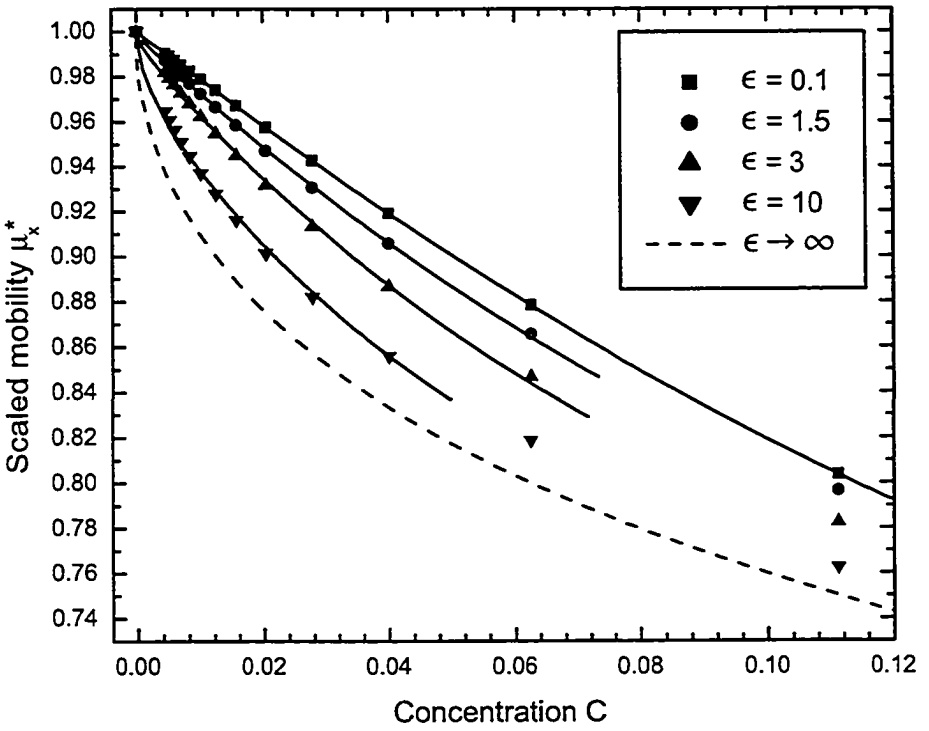

Figure 3.3: Scaled mobility μ_x^* vs concentration of obstacles C for periodic distributions of obstacles. The solid lines show the best fits obtained for low concentrations using Eq. 3.4 (the parameters are presented in Table 3.1). The dashed line is the asymptotic function given by Eq. 3.3.

In order to follow the continuous evolution of the power series expansion of μ_x^* between $\epsilon = 0$ and $\epsilon \to \infty$, the data points of Fig. 3.3 were fitted (solid lines on the graph) with the following expression:

$$\mu_x^*(C,\epsilon) \simeq \frac{(1 + b_1(\epsilon)C + b_2(\epsilon)C^2) \times (1 + b_{1/2}(\epsilon)C^{1/2})}{1 - C}. \tag{3.4}$$

The results of these fits are presented in Table 3.1. For the smallest value of ϵ studied, the two first integer coefficients are $b_1(\epsilon = 0.05) = -3.1522$ and $b_2(\epsilon = 0.05) = 5.213$. These values are close to the exact results $b_1(\epsilon = 0) \simeq -3.1416$ and $b_2(\epsilon = 0) \simeq 4.9348$ previously calculated (see Refs. [5, 6, 7] for details). The presence of the denominator $1 - C$ in Eq. 3.4 has for consequence that the series expansion of this expression has a term for every power of C, even when $\epsilon \to 0$ ($b_{1/2} \to 0$). Thus, we can evaluate effective higher expansion coefficients $(a_3, a_4, \ldots)$. For $\epsilon = 0.05$, we obtain a third order coefficient of $a_3 = 1 + b_1 + b_2 = 3.0608$

while the previously calculated exact value for $a_3(\epsilon = 0)$ is 2.4665. So even if we fit our data up to the second order (b_2), the expansion for the third order is quite close to the real value: this is why fitting with a form $(1+b_{1/2}C^{1/2})/(1-C))$ is better than $1/(1+b_{1/2}C^{1/2})$. We also notice that the half-integer coefficient $b_{1/2}(\epsilon = 0.05) = 0.0008$ converges toward zero when $\epsilon \to 0$, as it should. Finally, Table 3.1 shows that the coefficients slowly converge to the $\epsilon \to \infty$ value of -1 and 0 (for half-integer and integer coefficients, respectively), as predicted by Eq. 3.3. In other words, the transition from Eq. 3.2 to Eq. 3.3 is remarkably continuous.

ϵ	b_1	b_2	$b_{1/2}$
0[1]	$-\pi \simeq -3.1416$	$\frac{\pi^2}{2} \simeq 4.9348$	0
0.05	-3.1522 ± 0.0009[2]	5.213 ± 0.006	0.0008 ± 0.0001
0.1	-3.1525 ± 0.0009	5.215 ± 0.006	0.0008 ± 0.0001
0.2	-3.151 ± 0.001	5.215 ± 0.007	0.0005 ± 0.0001
0.4	-3.145 ± 0.002	5.23 ± 0.02	-0.0032 ± 0.0003
0.6	-3.152 ± 0.008	5.40 ± 0.05	-0.0095 ± 0.001
0.8	-3.18 ± 0.02	5.7 ± 0.1	-0.017 ± 0.002
1	-3.22 ± 0.02	6.2 ± 0.2	-0.024 ± 0.003
1.5	-3.35 ± 0.04	7.4 ± 0.3	-0.047 ± 0.006
3	-3.5 ± 0.1	9.4 ± 0.7	-0.14 ± 0.02
10	-2.6 ± 0.2	7.7 ± 1	-0.48 ± 0.02
50	-0.68 ± 0.05	1.6 ± 0.3	-0.872 ± 0.006
100	-0.36 ± 0.03	0.8 ± 0.1	-0.933 ± 0.003
300	-0.117 ± 0.009	0.23 ± 0.04	-0.978 ± 0.001
∞[3]	0	0	-1

[1] The results for $\epsilon = 0$ were taken from [6].

[2] The uncertainties presented in this Table were obtained from the software (Origin) used to performed the fits.

[3] See Eq. 3.3.

Table 3.1: Fitting parameters for the field-dependent mobilities in periodic systems of obstacles (Eq. 3.4). Some of these fits are shown in Fig. 3.3.

3.2 Randomly distributed obstacles

In the previous section we demonstrated that the electric field does not really have a major influence on the mobility of our small analytes for systems with periodically distributed

obstacles. Now we will investigate the case where the obstacles are randomly distributed. We will distinguish between two kinds of random distributions. The first one is a conditional random distribution where obstacles are placed such that we avoid the formation of trapping regions. In the second case we impose no restriction on the random distribution of obstacles (compare Figs. 3.1b and 3.1c). The results presented here were obtained using a numerical implementation of the technique described in Sec. 2.5 (algebraic solutions of the matrix equations for arbitrary values of ϵ are not possible for large random systems).

Random maze distributions

With the aim of avoiding the formation of trapping regions (dead-ends), we generated random distributions of obstacles with the following additional simple constraint:

The diagonal sites adjacent to an obstacle had to be free of obstacles.

This formed random mazes of linear walls (Fig. 3.1b) that do not possess any dead-ends. We then calculated the mobility of our 1×1 analyte on $N \times N$ (with $N = 100$) lattice systems for various values of C and ϵ. For a given pair (C, ϵ), we calculated the mobility for an ensemble of $\Omega = 500$ different systems. So the results presented here are averages over Ω exact solutions. Uncertainties on these average values were obtained from the standard deviation of our exact results divided by $\Omega^{1/2}$. Typically, these uncertainties were smaller than 0.1%: this is why we do not show error bars on our graphs.

Figure 3.4 shows the scaled mobility μ_x^* vs the concentration of obstacles for different values of the field ϵ. We observe that the mobility decreases when the concentration C or the electric field ϵ increase. In both cases, this could be explained by the increasing number of collisions between the analyte and the obstacles. In the first case, it is due to the increased number of obstacles while in the second it is due to the increasing number of successive collisions per obstacle (the flatness of the obstacles is now dominating the dynamics because of the existence of very long *walls* aligned along the y-axis).

Solid lines in Fig. 3.4 are the best third order polynomial fits (see Eq. 3.2). The coefficients $a_1(\epsilon)$, $a_2(\epsilon)$ and $a_3(\epsilon)$ are given in Table 3.2. For all the values of ϵ studied here, the fits have a positive curvature, a result that we also obtained for the periodic distributions (see Fig. 3.3 and Table 3.1). This similarity is the reason why we used Eq. 3.2 to fit our

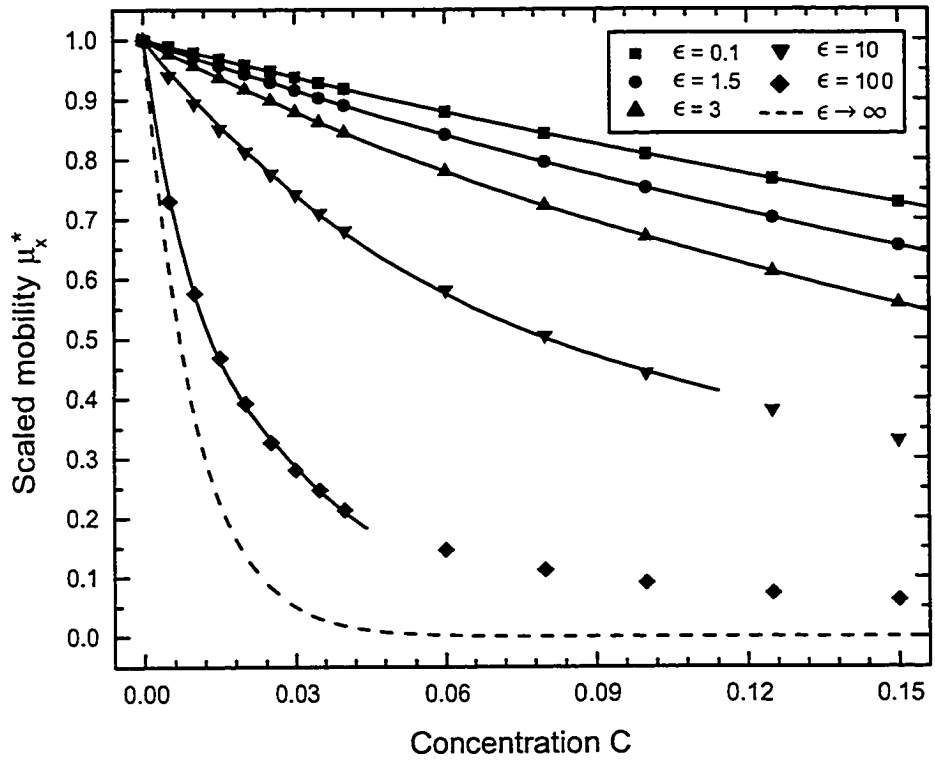

Figure 3.4: Scaled mobility μ_x^* vs concentration of obstacles C for random maze distributions of obstacles (no trapping regions). The solid lines show the best third order polynomial fits for low concentrations (Eq. 3.2) (the parameters are presented in Table 3.2). The dashed line is the finite-size asymptotic function $\mu_x^*(C, N, \epsilon \to \infty)$ with $N = 100$ (Eq. 3.5).

data. In fact, the coefficient $a_1(\epsilon)$ approaches the value of $1 - \pi$ found for the periodic system when $\epsilon \to 0$ [5, 6, 7]. Therefore, this kind of random system is qualitatively (but not quantitatively, of course) similar to periodic systems.

The dashed line in Fig. 3.4 represents the asymptotic limit of $\mu_x^*(C)$ when $\epsilon \to \infty$. This line is given by the following function:

$$\mu_x^*(C, N, \epsilon \to \infty) \simeq (1 - C)^{N-1} \simeq 1 - (N - 1)C + \frac{(N - 1)(N - 2)C^2}{2} - \ldots \qquad (3.5)$$

This relation is obtained using the logic that led to Eq. 3.1, i.e. that at infinite field intensity ($\epsilon \to \infty$), there is no lateral communication between the rows of the system and the mobility is then given by the ratio of the number of free sites on rows without obstacles and the number of free sites in the whole system. Here, we estimated that the probability to get an empty row is $(1 - C)^N$, so that the average number of empty rows $\langle N_e \rangle$ is given

ϵ	a_1	a_2	a_3
0.05	-2.1390 ± 0.0009[1]	2.39 ± 0.02	-1.36 ± 0.09
0.1	-2.141 ± 0.001	2.43 ± 0.03	-1.6 ± 0.1
0.2	-2.1504 ± 0.0009	2.43 ± 0.02	-1.61 ± 0.09
0.4	-2.200 ± 0.001	2.61 ± 0.02	-2.2 ± 0.1
0.7	-2.342 ± 0.001	3.13 ± 0.03	-3.4 ± 0.1
1	-2.542 ± 0.002	3.89 ± 0.03	-4.9 ± 0.2
1.5	-2.955 ± 0.002	5.63 ± 0.05	-8.4 ± 0.3
3	-4.38 ± 0.02	13.4 ± 0.4	-25 ± 2
10	-10.5 ± 0.1	68 ± 3	-187 ± 15
100	-63 ± 2	2660 ± 199	-64859 ± 7896
∞[2]	-99	4851	−156849

[1] The uncertainties presented in this Table were obtained from the software (Origin) used to performed the fits.

[2] Expansion coefficients of Eq. 3.5 with $N = 100$.

Table 3.2: Fitting parameters for the field-dependent mobilities in random mazes (third order polynomial, Eq. 3.2). Some of these fits are presented in Fig. 3.4.

by:

$$\langle N_e \rangle = N(1-C)^N. \tag{3.6}$$

Then, Eq. 3.5 is obtained dividing the number of free sites in empty rows $N\langle N_e \rangle$ by the total numbers of free sites $N_{free} = N^2(1-C)$:

$$\frac{N\langle N_e \rangle}{N_{free}} = \frac{N^2(1-C)^N}{N^2(1-C)} = (1-C)^{N-1}. \tag{3.7}$$

Obviously, this expression is an approximation which takes into account the finite size N of the system. In order to verify the validity of this expression, we simulated 10000 random distributions of obstacles (with $N = 100$) in which we calculated the average number of rows without obstacles. We did this for different values of C and fitted the data using Eq. 3.5 with N as a free parameter. We obtained a value of $N = 100.428 \pm 0.007$. Therefore, Eq. 3.5 is expected to be an excellent approximation of the asymptotic behavior of $\mu_x^*(C, N, \epsilon \to \infty)$. In the thermodynamic limit ($N \to \infty$), this function becomes a straight vertical line at $C = 0$, i.e. there is no net mobility because there is no empty row anymore (note, however, that the velocity $v\epsilon = \mu(\epsilon) \times \epsilon$ still diverges in this limit). Finally, Eq. 3.5 shows that the series expansion of μ_x^* retains only integer powers of C at high electric field ϵ. This is the

reason why we used Eq. 3.2 (integer series) instead of Eq. 3.4 (half-integer series) to fit the random maze results. In fact, when the electric field ϵ increases, the coefficients presented in Table 3.2 slowly converge toward those of the asymptotic prediction ($\epsilon \to \infty$), given in the last row.

Pure random distributions

The same calculations as the one described in the previous section were performed for unconditional random systems like the one shown in Fig. 3.1c. The dependence of μ_x^* upon C is shown in Fig. 3.5 for several values of ϵ. Obviously, these random systems are much more affected by an increase of the concentration. This is due to the random formation of trapping regions, like the one shaded in Fig. 3.1c. The only way to escape out of this kind of trap is to move against the electric field. Therefore, the probability to escape is directly related to the backward jump probability P_-. In the previous case, the decrease of the mobility was due to collisions with flat obstacles, and escape was then solely through the probability $P_\perp$ of lateral motion around these obstacles. However, the dependence upon the field intensity ϵ is significantly different between these two probabilities (compare P_- and $P_\perp$ in Fig. 2.2b). In fact, the probability P_- is almost zero (< 0.01) for $\epsilon > 2$ while $P_\perp$ is non negligible (> 0.01) for ϵ up to 50. Moreover, if a trap is of depth h, the particle has to move backward a minimum of h times which leads to an even lower probability $\sim {P_-}^h$ (one has $h = 3$ in Fig. 3.1c for example).

A striking characteristic of the curves presented in Fig. 3.5 is that there is a critical concentration (C^*) above which the curvature is changed (i.e., there is an inflection point at $C = C^*$). Therefore, these curves can be divided into two regions: the low concentration region could be fitted with a polynomial expression as we did for the random mazes, while the high concentration region could be described by an exponential decay. In order to fit the data shown in Fig. 3.5, we thus represent these two characteristics within a single empirical interpolating function:

$$\mu_x^*(C,\epsilon) \simeq \frac{1 + a(\epsilon)C + b(\epsilon)C^2}{\exp\left\{\left(\frac{C}{C_0(\epsilon)}\right)^{\delta(\epsilon)}\right\}}. \tag{3.8}$$

The results of these fits are presented in Table 3.2 and Fig. 3.5. At low values of the electric

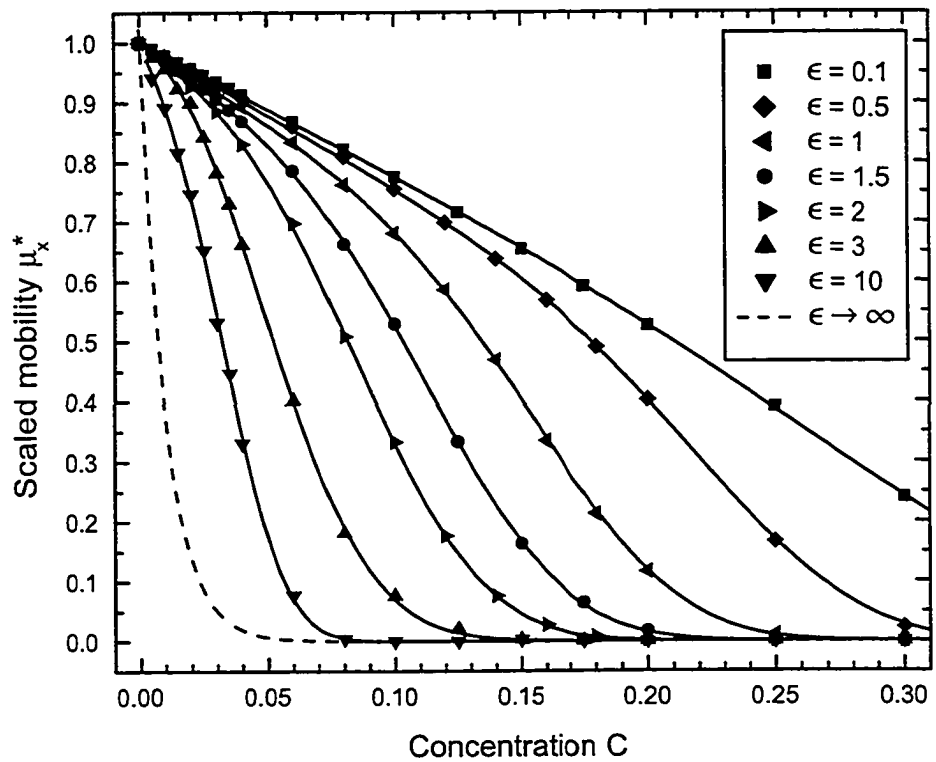

Figure 3.5: Scaled mobility μ_x^* vs concentration of obstacles C for random distributions of obstacles. The solid lines show the best fits obtained from Eq. 3.8 (the parameters are presented in Table 3.2). The dashed line is the finite-size asymptotic function $\mu_x^*(C, N, \epsilon \rightarrow \infty)$ with $N = 100$ (Eq. 3.5).

field, only the polynomial part of the fit (we then fix the denominator in Eq. 3.8 to 1) is necessary to represent the data (for the studied range of concentrations C). Similarly, for high values of ϵ, it is the second order polynomial that becomes useless to fit the data. Notice that since the value of the exponent δ is always greater than 2, the two terms of the polynomial part of Eq. 3.8 always remain meaningful. We find that the two first coefficients approach the previously obtained zero-field values [25] of $1 - \pi$ and -0.8558.

The infinite electric field limit (Eq. 3.5 with $N = 100$) is also presented by a dashed line in Fig. 3.5. Equation 3.5 is applicable for both kinds of random systems because the major cause for the reduced mobility at $\epsilon \rightarrow \infty$ is the presence of an obstacle on a row (the formation of traps is not the main retardation factor anymore). So the difference between these two distributions is only important at finite values of ϵ where the decrease of μ_x^* with

ϵ	a	b	C_0	δ
0[1]	$1-\pi \simeq -2.1416$	-0.8558		
0.01[2]	-2.118 ± 0.004[3]	-1.17 ± 0.02		
0.1	-2.092 ± 0.009	-1.43 ± 0.04		
0.5	-2.232 ± 0.008	-1.84 ± 0.08	0.2672 ± 0.0007	5.96 ± 0.04
1[4]	-2.68 ± 0.03		0.1853 ± 0.0005	4.34 ± 0.06
1.5	-3.00 ± 0.03		0.1426 ± 0.0004	3.52 ± 0.04
2	-3.27 ± 0.09		0.1120 ± 0.0007	3.03 ± 0.05
3	-2.8 ± 0.4		0.069 ± 0.001	2.28 ± 0.07
10	-9.6 ± 0.6		0.048 ± 0.001	2.7 ± 0.1

[1] The results for $\epsilon = 0$ were taken from [25].

[2] For $\epsilon = 0.01$ and $\epsilon = 0.1$, only the polynomial part of Eq. 3.8 was used to fit the data.

[3] The uncertainties presented in this Table were obtained from the software (Origin) used to performed the fits.

[4] For $\epsilon \geq 1$, the parameter b is useless to fit the curves (the error of b is larger than b for $\epsilon \geq 1$).

Table 3.3: Fitting parameters of Eq. 3.8 for the data of Fig. 3.5 (random distributions of obstacles).

the concentration C is amplified by the formation of trapping regions. Finally, Fig. 3.6 shows the variation of both C^* and C_0 with ϵ. We can see that these two concentrations are close to each other for all values of ϵ, as expected. However, this graph suggests that, even at very high electric field ϵ, there always exists an inflection point at a finite concentration C^*. This is also due to finite-size effects (see below).

All the cases studied in Sec. 3.2 are based on finite $N \times N$ (with $N = 100$) lattice systems with PBCs. In fact, the value of N has an influence on the calculation of the mobility (especially with random distributions of obstacles): this is called the finite-size effect of the PBCs. The value of N has to be as large as possible to represent truly infinite and random systems, but this is limited by the fact that the computational time increases extremely rapidly with N. For instance, when N increases by a factor 2, the number of variables and equations to solve increase by a factor 4. When we perform the same calculations for different values of N, we see that the mobility decreases slowly with N (see, e.g., the inset of Fig. 3.6). However, this variation is negligible at low concentrations or for low electric fields. Our results are thus overestimated and this error increases with both C and ϵ. Consequently, the correct method to reach the asymptotic (or thermodynamic)

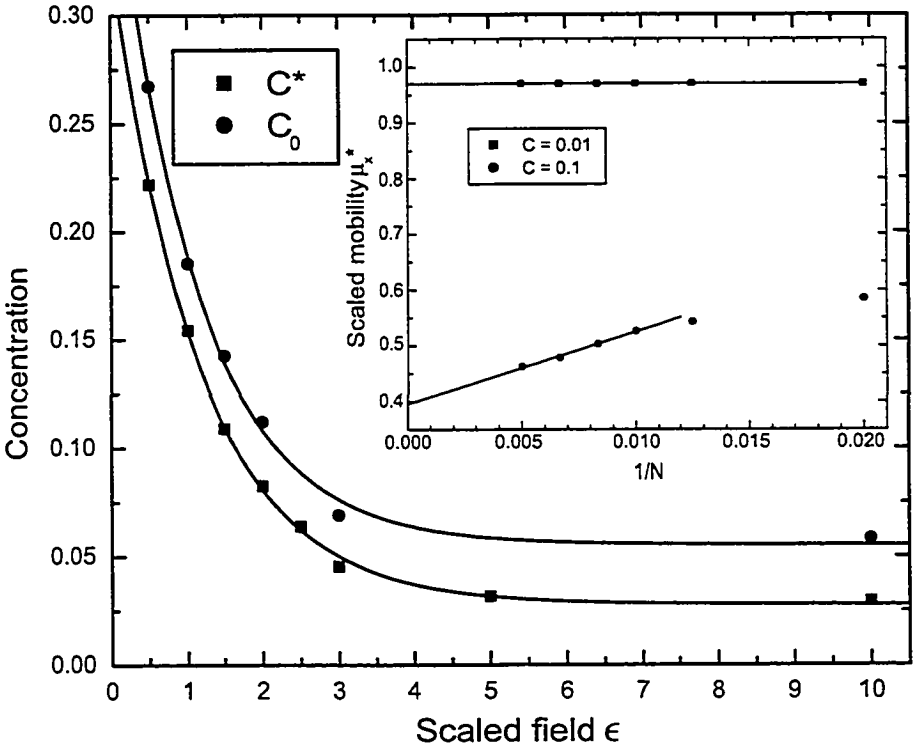

Figure 3.6: Concentrations C^* and C_0 vs scaled electric field ϵ for a pure random distribution of obstacles. Solid line are the best fits using empirical, shifted exponential decay curves given by $C^* = 0.02766 + 0.29982\exp(-0.86563\epsilon)$ and $C_0 = 0.05522 + 0.33578\exp(-0.92395\epsilon)$. The inset shows the variation of the scaled mobility μ_x^* vs $1/N$ for two different concentrations and a high scaled field intensity $\epsilon = 1.5$.

limit ($N \to \infty$) is to perform calculations for several values of N and to extrapolate the mobility on a μ_x^* vs $1/N$ graph (inset of Fig. 3.6). Although straightforward, this approach is clearly beyond the scope of this thesis since our main goal was to develop the theoretical tools to study sieving at non-negligible field intensities. Furthermore, the results presented here are just for two-dimensional *toy models* of gel sieving. A realistic study would require three-dimensional gels and as well as a study of finer mesh sizes, similar to the one carried out previously for the $\epsilon \to 0$ limit [19].

Effect of the high electric field

In random mazes and pure random systems, we linked the reduction of the mobility to the decrease of the probabilities $P_\perp$ and P_- with ϵ. These probabilities are directly related to the time needed to avoid a wall of obstacles or to go out of a trapping region.

In random maze systems, the decrease of the mobility when $\epsilon \to \infty$ at constant concentration is due to the decrease of the lateral motion probabilities $P_\perp$ and, consequently, should be similar to the one observed for periodic systems. The example presented in Sec. 2.5 told us that this decrease is inversely proportional to the external field ϵ (see Eq. 2.36). On the other hand, in pure random systems, the formation of trapping regions should increase the decay of the mobility by an exponential factor due to the necessary backward jumps. Moreover, this exponential factor should increase with the average depth h of the traps present in the system.

In order to confirm these predictions, we calculated the exact analytical mobilities of 1×1 particles in three different systems (Fig. 3.7). The corresponding asymptotic mobilities are respectively:

$$\text{(a)} \quad \mu_x^*(\epsilon \to +\infty) \cong \epsilon^{-1} - \frac{5}{4}\epsilon^{-2} + \frac{25}{16}\epsilon^{-3} + O(\epsilon^{-4}) . \tag{3.9}$$

$$\text{(b)} \quad \mu_x^*(\epsilon \to +\infty) \cong \exp(-2\epsilon)\left\{2\epsilon^{-1} - \epsilon^{-3} + O(\epsilon^{-4})\right\} . \tag{3.10}$$

$$\text{(c)} \quad \mu_x^*(\epsilon \to +\infty) \cong \exp(-4\epsilon)\left\{2\epsilon^{-1} - \epsilon^{-2} + \frac{1}{2}\epsilon^{-3} + O(\epsilon^{-4})\right\} . \tag{3.11}$$

From these results, we can see that the leading term of the asymptotic decrease of the mobility in random systems is given by:

$$\mu_x^*(\epsilon \to +\infty) \propto \frac{\exp(-2\epsilon h)}{\epsilon} . \tag{3.12}$$

which nicely confirms our explanation. Furthermore, Eq. 3.9 is indeed similar to Eq. 2.36, which applied to trap-free, periodic systems.

According to these results, the decrease of the mobility with increasing field ϵ (at constant concentration C) must become exponential for large field intensities in our pure random distributions of obstacles. Figure 3.8 shows the scaled mobility $\mu_x^*(\epsilon)$ vs ϵ at $C = 0.1$.

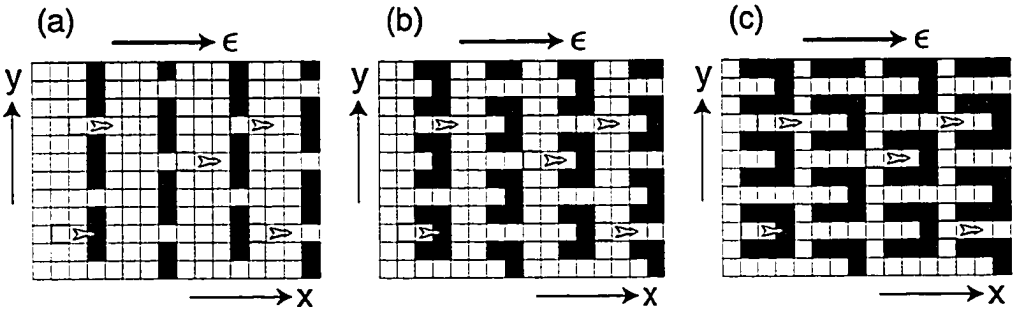

Figure 3.7: Three different *trap* systems. In (a), the trap depth is $h = 0$ and this distribution is similar to our random maze distributions. The average trap depths are $h = 1$ and $h = 2$ for (b) and (c) respectively.

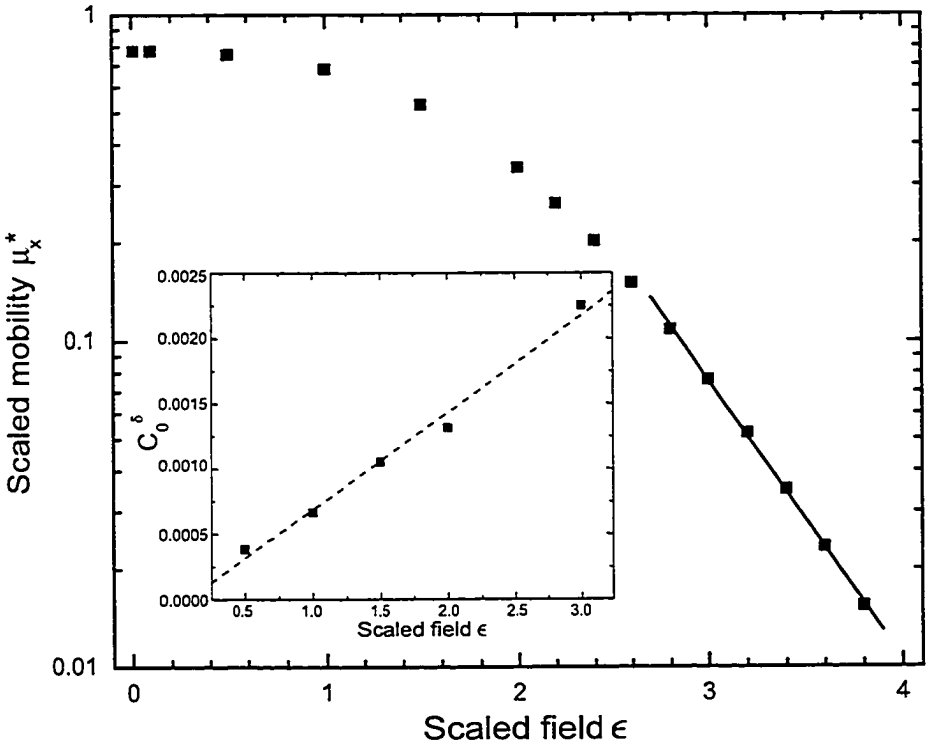

Figure 3.8: Scaled mobility μ_x^* vs scaled electric field ϵ for pure random distributions of obstacles. These data were obtained for a 100 × 100 site lattice with 1000 obstacles ($C = 0.1$). The inset shows the linear relation between $C_0(\epsilon)^{\delta(c)}$ and ϵ (see Table 3.2).

The straight line confirms the fact that $\ln \mu_x^*(\epsilon) \propto -\epsilon$ in the asymptotic limit ($\mu_x^* < 1/10$ and $\epsilon > 5/2$). At lower field intensities, other factors enter the problem. The exponential behavior of $\mu_x^*(C, \epsilon)$ at high electric field is also illustrated by the inset in Fig. 3.8, which shows the linear variation of the combined empirical fitting parameters $C_0(\epsilon)^{\delta(\epsilon)}$ vs the scaled electric field ϵ.

3.3 Discussion

Sieving models for small particles, such as the OMRC model, are typically based on equilibrium arguments. Consequently, these models do not include the intensity of the electric field used to drive the electrophoretic separation. Indeed, many of them have been borrowed from theories of diffusion in random systems [26, 27, 28], where the field is zero by definition. In previous studies [5, 6, 7, 8, 9, 10, 11, 12], the goup of Dr. Slater developed a complete mathematical framework to compute exact electrophoretic mobilities for model particles migrating on various lattice systems in the limit of vanishing fields ($\epsilon \to 0$). This model allowed our group to refute the main assumptions of the OMRC/mean field models, namely that the mobility is linearly proportional to the free available volume. Even in the zero-field limit, the correlations between the positions of the obstacles play an important role in the problem, and the mobility of a given analyte can be quite different in gels of different architectures that otherwise would offer the same free available volume. In other words, the gel structure does matter even if $\epsilon \to 0$.

At finite field intensities, random gels offer dead ends that severely reduce the mobility of non-deformable analytes because of the trapping phenomenon. This effect has been studied experimentally by the group of Serwer [24, 29, 30, 31, 32, 33]. For example, charged beads were observed to be completely trapped (over the duration of the experiment) in agarose gels when the field exceeded a given critical value. The mobility-field-size relationship that characterizes such trapping phenomena was then exploited to create ratchet-based separation systems. To and Boyde [34] reported that pulsed fields can free the trapped beads from the dead ends if the duration of the reverse pulse is properly chosen. As far as we know, there is currently no theory of electrophoretic sieving that can be used to analyze such experimental situations, not even in an approximate way. The next chapter uses the

method developed here to investigate such problems.

Furthermore, the effect of individual analyte-obstacle (e.g., gel fibres) collisions can be modified at finite field intensities because the electric force may induce repetitive collisions between an analyte and the obstacle(s) in its path. If an obstacle is non-conducting, the field lines will curve around it and this will reduce the steric effects of the collisions (note that it was previously shown that this is not the case when $\epsilon \to 0$).

For simple periodic systems, our approach can lead to exact, analytical results when a software such as Maple is used to solve the matrix equations algebraically. However, this is restricted to rather small systems (Sec. 3.1). Our results showed two interesting phenomena:

1. The corridor effect wherein an obstacle casts a shadow on the next obstacle behind it, thus reducing the probability for the analyte to collide with it. This leads to a slight increase of the mobility with increasing field intensities.

2. The flat-obstacle effect wherein the shape of the obstacle (and the direction of the local field lines) may lead to multiple consecutive collisions with the same obstacle. This leads to a decrease of the mobility.

However, neither of these two effects has a strong effect on the mobility of the analyte. In fact, given the magnitude of these effects (at most 1% and 10%, respectively), it is clear that they would become essentially negligible if we were to use finer mesh sizes, round obstacles, curved field lines and/or non-periodic gel systems. This explains the experimental observation that the mobility of small analytes is usually field-independent in absence of trapping effects. It is only with very large flat obstacles, which form random mazes, that we could observe very large effects of the obstacle shape.

Random gels, on the other hand, lead to quite a different behaviour. Dead-ends represent traps in which the field-driven motion stops for very long periods of time, in agreement with Serwer's experimental results. We indeed observed an exponential decrease of the mobility at large field intensities (Fig. 3.8), a clear indication of thermally activated escape from traps of depth $\sim \epsilon$. We proposed a simple empirical interpolating fitting formula for the mobility as a function of the concentration of obstacles.

In order to model realistic gel systems using our new model of finite-field electrophoretic sieving, we would need to make several straightforward changes: a) first, we must use three-dimensional systems; b) second, we would need to take the limit towards the continuum by using finer meshes and extrapolating towards infinitely small mesh sizes, a technique that was used successfully in the zero-field limit [19]; c) third, we would need to use obstacles with more conventional shapes such as cylindrical gel fibres; d) finally, for random systems, we would need to correct for finite-size effects using the extrapolating method discussed in Sec. 3.2 (see also [19]). Although all these changes are rather simple, they require considerable computing power.

Two more changes can be envisaged. Although the mobility of a point-like analyte can be computed quite easily, analytes with finite volumes and arbitrary shapes (such as ellipsoids or oligomers [10]) may lead to subtle problems. For instance, the different forces on the different parts of the analyte may generate torques, hence rotations. Also, non-conducting gel fibres lead to non-parallel field lines and inhomogeneous field intensities. As we mentioned previously, our approach requires that the local electric field points along a cartesian axis so that the motion along the various axes are perfectly decoupled. Non-parallel field lines thus represent a challenge. We will discuss this issue in more details in chapter 6.

Finally, calculating the diffusion coefficient D in the presence of a non-negligible field intensity is also a challenge since the Nernst-Einstein relation is not valid in such cases. It is well-known that the diffusion coefficient actually increases rapidly with the field intensity, especially in the presence of trapping. This increase is due to the random nature of the thermally-activated escape process: when a particle is trapped, all the non-trapped particles move away from it very quickly if the field is high, and this leads to a field-driven contribution to the diffusion coefficient that increases like the square of the velocity [35]. As far as we know, there is no simple method for calculating $D(\epsilon)$. In fact, even the obstacle-free case is subtle. For example, our current approach predicts a field-dependent diffusion coefficient for a free particle because all the jumps are assumed to take the same amount of time. This is also the case of all Metropolis-based Monte Carlo simulations, although very few articles or textbooks mention this. We believe that it is possible to correct for this by adding a probability $S = S(\epsilon)$ of not moving per unit time, but generalizing this

approach to more than one dimension and to systems with obstacles is not straightforward. This will be the topic of chapter 5 in this thesis. This would be a very important addition to our theoretical tools since high-field electrophoretic migration is known to lead to very broad bands [30]. Understanding and controlling this increased band broadening is key to optimizing trapping-based separation systems.

Chapter 4 Application to Separation Techniques

Most of the new developments in biotechnology and molecular biology share a common basic key experimental tool: the electrophoretic sorting of particles and molecules. Simulation techniques that can be used to study these separation processes become indispensable to search for novel procedures or to simply optimize the existing ones. In the last two chapters, we presented a calculation technique that can be used to study the velocity of particle in a given distribution of obstacles. However, we were restricted to studying the evolution of the velocity of a single particle as some system parameter was varied (e.g., the field or the gel concentration). Of course, in order to understand and model separation processes, one must be able to compare the velocity of different types of particles. The current chapter has for objective to describe how our model can be further generalized and used to compare the dynamics of different charged or sized particles. We will show how this extension allows us to study both the spatial and angular separation of particles. Finally, we will also demonstrate that, in principle, our calculation technique can also be used to study the influence of the concentration of analytes on their average velocity.

4.1 The Fundamental Parameters

The velocities that we can calculate using the equations of chapter 2 are actually functions of the scaled external field ϵ and the Brownian time τ_B (the lattice parameter a can be chosen arbitrarily). However, ϵ is not only the external field applied on the system (E) since it is also proportional to the analyte's charge Q (see Eq. 2.2). Obviously, it would be quite useful to know how the velocity depends on some physical parameters like the electric charge Q, the field intensity E or the size R of the particle. In other words, since we want

The results of this chapter were published in: **M. G. Gauthier** and G. W. Slater "An exactly solvable Ogston model of gel electrophoresis: X. Application to high-field separation techniques". Accepted by *Electrophoresis*, November 11, 2002 (in press).

to compare the electrophoretic velocity of particles with different characteristics, we need to know the relation between the two model variables (ϵ and τ_B) and the particle properties Q and R. At the very least, we need simple scaling relations to relate the numerical results to actual experimental conditions. In order to compare different particles, we must define a reference size R_0 and a reference charge Q_0. All velocities in this chapter will be expressed in terms of ϵ_0 and τ_{B_0}, which are respectively functions of Q_0 and R_0. We will fix the reference size R_0 equal to the lattice parameter a (the smallest particle that we can represent), a natural choice.

Since $\epsilon = QEa/(2k_BT)$, the scaled field intensity ϵ is a function of the particle's charge Q but not of its size (radius) R. Therefore, when the charge of the particle is changed by a factor α from Q_0 to Q, the external field is also changed by the same multiplicative factor:

$$\text{if} \quad Q = \alpha Q_0 , \qquad \text{then} \quad \epsilon = \alpha \epsilon_0 . \tag{4.1}$$

We also need the relation between the size R of the particle and its zero-field Brownian time τ_B. For a small analyte (see Sec. 4.2 below), the diffusion coefficient D_{0_R} is given by the Stokes relation $D_{0_R} = k_BT/6\pi\eta R$ (see Eq. 1.9), thus giving the scaling law $D_{0_R} \sim 1/R$. Since $D_{0_R} \sim a^2/\tau_B$, we have that $\tau_B \sim R$. This indicates that we can take into account the size of the particle simply by changing the value of its Brownian time. Therefore, when the (linear) size of particle is changed, the Brownian time is also changed by the same factor:

$$\text{if} \quad R = \beta R_0 , \qquad \text{then} \quad \tau_B = \beta \tau_{B_0} . \tag{4.2}$$

The velocity of an arbitrary particle can thus be expressed as a function of ϵ_0 and τ_{B_0} using Eqs. 4.1 and 4.2:

$$v(\epsilon, \tau_B) = v(\alpha\epsilon_0, \beta\tau_{B_0}) . \tag{4.3}$$

In Secs. 4.3 to 4.5, we will present results in terms of scaled velocities $v^*(\epsilon_0)$, which are simply given by the ratio of the velocity of the particle, $v(\epsilon, \tau_B)$, and the fundamental velocity unit of the system a/τ_{B_0}, which is the ratio between the reference length $R_0 = a$ divided by the reference time unit τ_{B_0} (the Brownian time of a particle of size R_0):

$$v^*(Q, R, \epsilon_0) = \frac{v(\alpha\epsilon_0, \beta\tau_{B_0})}{a/\tau_{B_0}} . \tag{4.4}$$

Note that we chose a unique normalization factor a/τ_{B_0} in order to have the same proportionality factor for all types of particles.

4.2 The Debye Layer

The theoretical elements of the previous section actually implied an approximation that we did not mention:

> *The Debye length λ_D, which is the thickness of the cloud of counter-ions surrounding the charged particle (Fig. 4.1), is large compared to the particle size R.*

The Debye length is defined as [3]:

$$\lambda_D = \left(\frac{\varepsilon_b \varepsilon_0 k_B T}{e^2 \sum z_i^2 C_i} \right)^{1/2} . \tag{4.5}$$

where ε_b is the dielectric constant of the fluid, ε_0 is the permittivity of vacuum, ez is the charge of the counter-ions and C is their concentration. The sum is over the ionic species (i). If this hypothesis is valid (this is called the thick diffuse layer limit), the free-flow electrophoretic velocity of the particle is simply related to the applied electric force $F_E(Q, E)$ and the (mechanical) friction coefficient $f(R)$ (Eq. 1.11):

$$v = \frac{F_E(Q, E)}{f(R)} = \frac{QE}{f(R)} . \tag{4.6}$$

The viscous drag coefficient $f(R)$ of a spherical particle is given by $6\pi\eta R$, where η is the solvent viscosity (alternatively, R can be seen as the hydrodynamic radius R_H of the particle if the latter is not spherical). The velocity then scales like $\sim Q/R$, which is consistent with the transformations that we defined in the previous section ($v \sim \epsilon/\tau_B$, with $\epsilon \sim Q$ and $\tau_B \sim R$). The results of Secs. 4.3 and 4.4 will be analyzed using this hypothesis ($\lambda_D \gg R$).

However, it is also possible to study separation techniques in the thin diffuse layer limit ($\lambda_D \ll R$) using our calculation method. The only difference would then be in the dependence of the velocity upon the particle size and charge. Without going into details, let's just say that, in such a case, the velocity will scale as $\sim \sigma\lambda_D$ [3, 36], where σ is the surface charge density of the particle. For example, if Q and R are varied simultaneously

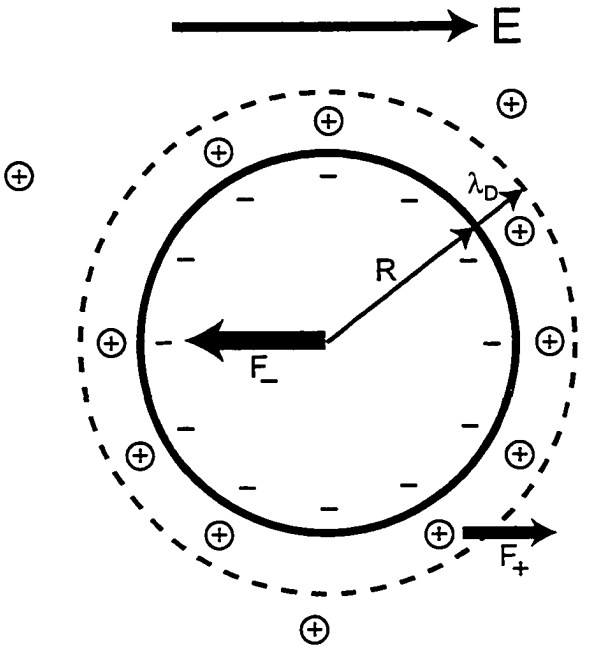

Figure 4.1: Schematic representation of the Debye length λ_D of a negatively charged spherical particle of radius R and its surrounding positive counter-ions in presence of an external field E.

in order to keep a constant surface charge density $\sigma \sim Q/R^2$, only the Debye length λ_D has an effect on the velocity.

4.3 Spatial separations

In this section, we will present examples of sieving and trapping systems. The electrophoretic velocity of particles with different charges and/or sizes will be computed for these particular distributions of immobile obstacles. As we will see, the velocity will be a nonlinear function of the applied field ϵ_0 (i.e., the electrophoretic mobility will be increasing or decreasing with the field intensity ϵ_0). We will demonstrate that biased, time-asymmetric AC fields can be used to produce new types of separations in this nonlinear regime. Finally, we will show that our approach can also be used to study the effect of the concentration of particles on their velocity. This will be illustrated by a simple example of particles jamming in narrow funnels.

It is important to stress the fact that there are many ways to vary Q and/or R when we want to compare different particles. Here, for example, we chose to give the same charge over size ratio $Q/R = Q_0/R_0$ to all particles. When we will compare small (1×1) and large (2×2) particles, we will attribute the reference charge Q_0 to the small particle of size $R_0 = a$. Then the large particle of size $R = 2R_0$ ($\beta = 2$) will have a charge $Q = 2Q_0$ ($\alpha = 2$) in order to respect the condition $Q/R = Q_0/R_0$. One can legitimately argue that, in many real situations, two different sized particles should have different charges, but the same surface charge density. Our choice is based on the fact that if the ratio Q/R is conserved, it is impossible to separate different sized particles using constant-field free flow electrophoresis (without a sieving matrix) due to fact that they then have the very same velocity (see Eq. 4.6). Thus, the separation effects that we obtain are entirely due to the lattice of obstacles and not to a difference of free flow velocities. It is straightforward to interpret our numerical results in the framework of other assumptions given the scaling relations derived in Sec. 4.1. The field intensity will thus be given by $\epsilon_0 = Q_0 E a/(2k_B T)$, i.e. by the relative change in potential energy between two adjacent sites for the small particle of charge Q_0 and size $R_0 = a$.

Sieves: Periodic obstacles

As we already mentioned, if the ratio Q/R is conserved, it is impossible to separate different particles without sieving matrices because they will all have the same net velocity proportional to the field ϵ_0. Let's now look at the effect of the simplest gel that we can use, i.e. a periodic distribution of obstacles. Figure 4.2 shows the net velocities of a small and a large particle in such a periodic gel. We see that the collisions with the obstacles induce a retardation factor that is a function of the particle size. However, the small particle is only $\approx 25\%$ faster than the large one. The velocities are almost linear functions of the field.

Sieves: Staggered filters

In order to describe how nonlinear dynamics can be exploited to separate different particles, we start with a simple example of sieving. The distribution of obstacles is presented in the inset of Fig. 4.3. It is essentially a stack of filters aligned along the y-axis. The filters have

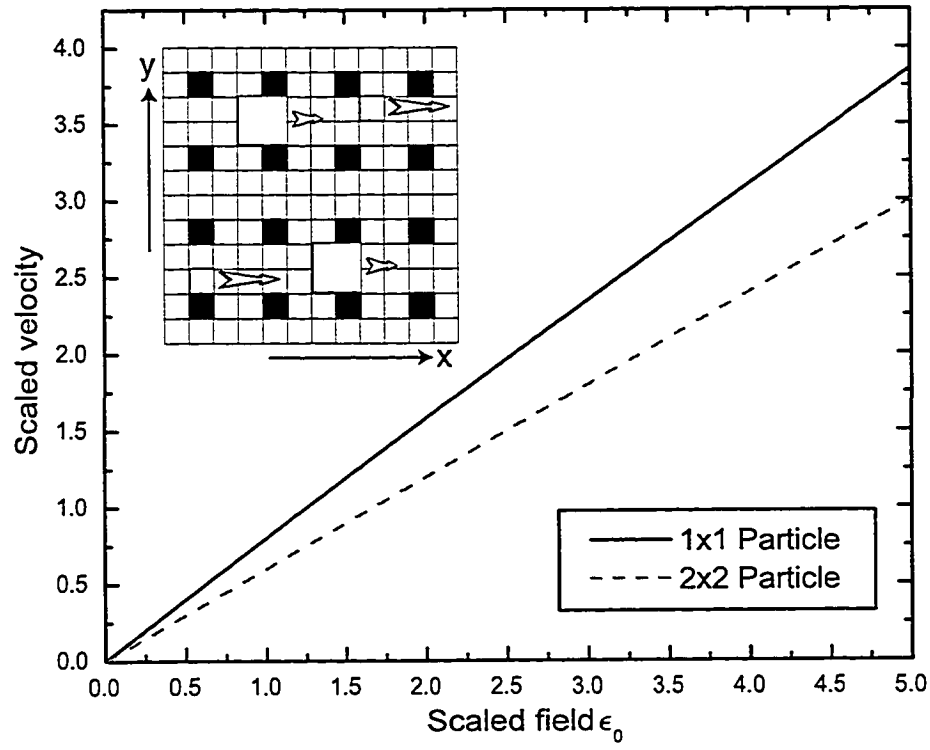

Figure 4.2: Scaled velocities vs scaled external field ϵ_0 for 1×1 and 2×2 particles in the distribution of periodic obstacles shown in the inset (DC field). The small particles are always faster than the large ones.

two types of holes (of sizes $1a$ and $3a$), and they are staggered so that holes of the same size are not facing each other. Each obstacle can be seen as a post that is orthogonal to the plane (as in the microfluidic sieves of Ref. [37]). Clearly, there is a +/- symmetry along the x-axis. First, we examine the DC velocity, along the x-axis, of small (1×1) and large (2×2) particles (the field is itself pointing in the $+x$ direction). For small systems like this one (i.e., the periodic cell of the geometric pattern is small), exact analytical results can still be obtained using mathematical softwares like Maple. For example, the scaled velocity of the large particle ($\alpha = 2$ and $\beta = 2$) in this system is given by:

$$v_x^*(\epsilon_0) = \frac{\alpha\epsilon_0}{\beta} \frac{6\sinh 3\alpha\epsilon_0}{12\alpha\epsilon_0 \cosh 3\alpha\epsilon_0 + 10\sinh 3\alpha\epsilon_0 + 8\alpha\epsilon_0 \cosh \alpha\epsilon_0} \tag{4.7}$$

$$\simeq \frac{\alpha\epsilon_0}{\beta}\left(\frac{9}{25} - \frac{126}{625}\alpha^2\epsilon_0^2 + \frac{3414}{15625}\alpha^4\epsilon_0^4 + O(\alpha^6\epsilon_0^6)\right). \tag{4.8}$$

Note that the series in the parenthesis is an even function of ϵ_0 because the distribution of obstacles is symmetric along the x-axis. The result for the smaller particle gives a function too long to reproduce here. These two functions, which correspond to the velocities in the presence of a DC external field, are compared in Fig. 4.3a. The small particle is always faster than the large one.

Let us now examine what happens if we use low-frequency pulsed electric fields. Obviously, if an unbiased AC field is applied, the particle will have the same absolute velocity in both the positive and the negative part of the cycle and the net velocity will be zero. However, we can exploit the non-linearity of Eq. 4.7 to get net motion, even in the absence of a net applied force. This can be done with a time-asymmetric pulsed field like the one shown in Fig. 4.4 (there is no net field if we choose $\gamma_1 = 1/\gamma_2$). If we assume that the pulse durations are large compared to the microscopic relaxation times of the particles, the net scaled velocity is simply given by:

$$v^*_{net} = \frac{v^*_x(\epsilon) + \gamma_2 v^*_x(-\gamma_1 \epsilon)}{1 + \gamma_2}. \tag{4.9}$$

When $\gamma_1 = 1/\gamma_2$, we have a ratchet system where nonlinear dynamics lead to net particle displacement in absence of a net external force (the positive and negative pulses have different amplitudes and time durations but the average applied field is zero). Such an example (with $\gamma_1 = 2$ and $\gamma_2 = 1/2$) is presented in Fig. 4.3b. We see that the velocities are smaller than with the DC field, but the use of a time-asymmetric pulsed field let us choose which particle will elude first. Indeed, there is a critical field $\epsilon_{c_1} \approx 1.25$ where the two particles have the same net scaled velocity v^*_x. Thus, it is possible to choose which particle will move faster just by changing the value of ϵ_0 (the 1×1 particles move faster if $\epsilon_0 > \epsilon_{c_1}$, and vice versa).

Finally, Fig. 4.3c shows a case where the pulsed field is negatively biased (with $\gamma_1 = 2$ and $\gamma_2 = 0.6$). Here, there is a critical field $\epsilon_{c_2} \approx 0.22$ above which the two particles move in opposite directions. It is thus possible to design a system and a pulsed field sequence to separate particles and even select a particular size. Since our results are in fact analytical functions, it is possible to study the exact conditions for the existence (in terms of γ_1 and γ_2) of the critical field ϵ_{c_2}. The slope of the net scaled velocity of the 2×2 particle at the

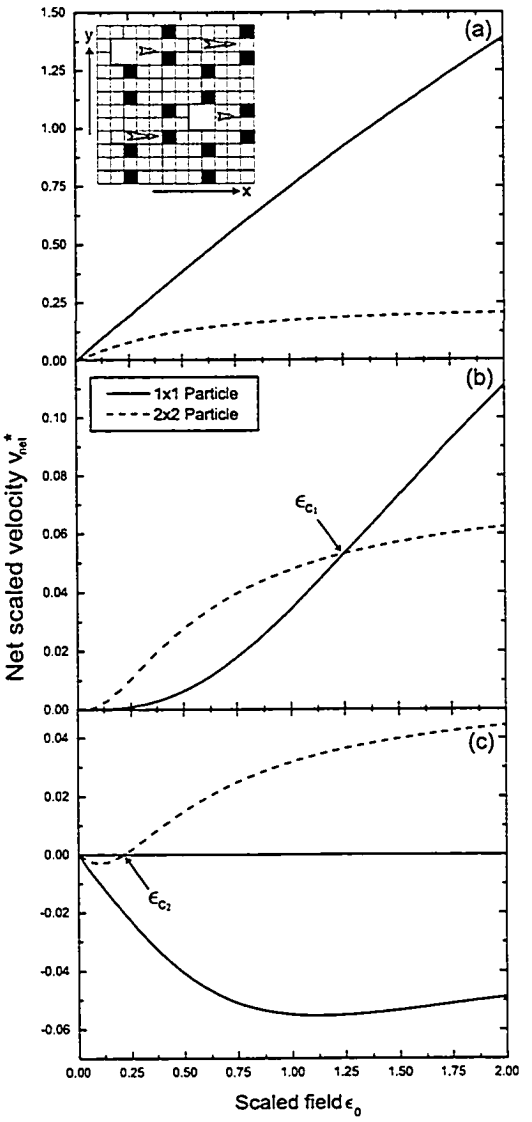

Figure 4.3: (a) Velocities of 1×1 and 2×2 particles driven by a DC field applied along the x-axis. The distribution of obstacles is shown in the inset. The small particles go faster than the large ones. (b) Net velocities of 1×1 and 2×2 particles driven by an unbiased time-asymmetric pulsed field applied along the x-axis ($\gamma_1 = 2$ and $\gamma_2 = 1/2$; see Fig. 4.4). There is a critical value of the external field $\epsilon_{c_1} \approx 1.25$ for which both particles have the same velocity. (c) Same as in (b) except that the field is negatively biased ($\gamma_1 = 2$ and $\gamma_2 = 0.6$). There is a critical value of the external field $\epsilon_{c_2} \approx 0.22$ above which the two kinds of particles migrate in opposite directions.

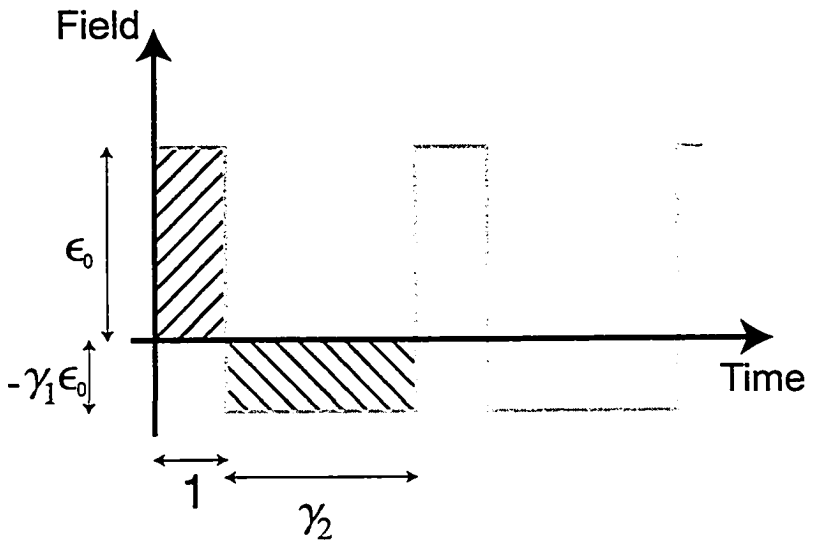

Figure 4.4: The square pulse AC field used in this article. The pulse durations are assumed to be much larger than the microscopic relaxation times in the system. The dimensionless parameters γ_1 and γ_2 can be adjusted to generate various types of biased and/or asymmetric pulsed fields. In the particular case where $\gamma_1\gamma_2 = 1$, the two dashed regions have the same surface areas and the net (average) field is zero; we then say that the field is unbiased. A special example is the time-symmetric unbiased pulsed field where $\gamma_1 = 1/\gamma_2 = 1$. When $\gamma_1\gamma_2 > 1$, the field is biased in the negative direction, while it is biased in the positive direction if $\gamma_1\gamma_2 < 1$.

origin (combining Eqs. 4.7 and 4.9) is given by:

$$\left.\frac{\partial v^*_{net}(\epsilon_0,\gamma_1,\gamma_2)}{\partial\epsilon_0}\right|_{\epsilon_0=0} = \frac{9}{25}\times\frac{1-\gamma_1\gamma_2}{1+\gamma_2}. \tag{4.10}$$

Therefore, the condition for the existence of a non-zero critical value ϵ_{c_2} is $\gamma_1\gamma_2 > 1$ (a negative slope at the origin), whereas $\epsilon_{c_2} = 0$ for $\gamma_1\gamma_2 \leq 1$. The limiting case is given by $\gamma_1\gamma_2 = 1$, which is an unbiased (time-asymmetric or not) field. All negatively biased pulsed sequences thus give rise to the type of curve shown in Fig. 4.3c.

Traps

In the previous example, the distribution of obstacles was symmetric for motion along the x-direction. Separation could be achieved in the presence of a DC field. Furthermore, a net ratchet drift was obtained using a time-asymmetric pulsed field with a zero mean value. We now present an example of an asymmetric distribution of obstacles (see inset of Fig. 4.5).

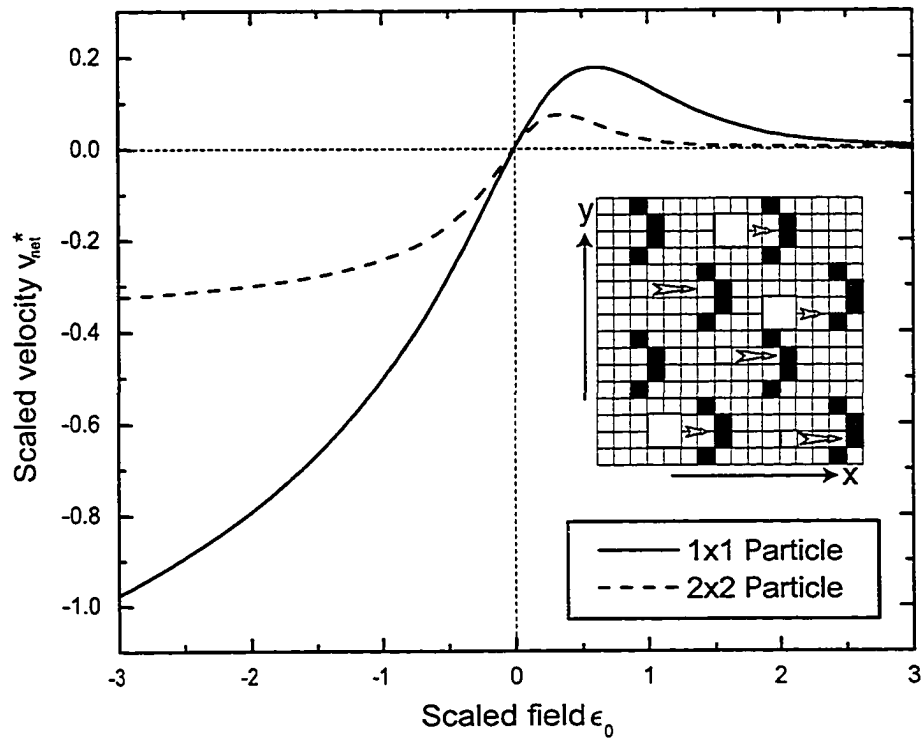

Figure 4.5: Scaled velocities vs scaled external field ϵ_0 for 1×1 and 2×2 particles in the distribution of traps shown in the inset. The small particles are always faster than the large ones.

Here, the obstacles form trapping regions in which the particles can enter when moving in the $+x$ direction; there is no such traps when moving in the opposite $(-x)$ direction. This obviously induces an asymmetry in the DC velocity along the x-axis (Fig. 4.5): particles tend to move faster in the $-x$ direction for a fixed field intensity. When $\epsilon_0 \gg 0$, the velocity decreases exponentially with the field intensity because the electric force pulls the particle inside the $\supset$ shaped traps (thermally activated escape from such traps becomes less likely at high field). When $\epsilon_0 < 0$, the particle simply slides off these obstacles. Clearly, a negative field is preferable here to obtain a good separation with a DC field, and the resulting separation is comparable to that obtained with DC fields in the previous section.

Here, again, we can exploit the nonlinear nature of the migration of the particles in the system of obstacles. For instance, we can get net motion in the $-x$ direction simply by using an unbiased and symmetric AC field ($\gamma_1 = \gamma_2 = 1$ in Fig. 4.4). As in the previous

example, different sized particles can be separated using this ratchet process because they move at different velocities (Fig. 4.6a).

However, it is possible to better control the separation with a biased AC field. When the AC field is unbiased ($\gamma_1 = \gamma_2 = 1$), both particles move in the $-x$ direction for all values of ϵ_0 and it is possible to set the value of the field to decide which particle will be the fastest. In contrast, when a positive bias (e.g., $\gamma_1 = 1$ and $\gamma_2 = 1/2$) is imposed on the external field, a particle moves in the $+x$ direction for ϵ_0 smaller than a critical value ϵ_c, and in the opposite direction otherwise. The interesting point is that the critical field ϵ_c is function of the type of particle used so there is a range of values of $\epsilon_{c_1} < \epsilon_0 < \epsilon_{c_2}$ where the two particles move in opposite directions. This result was also obtained in the previous section but with an AC field that was both time-asymmetric and biased. Here, only one of these conditions has to be satisfied to achieve motion in opposite directions. The results for 1×1 and 2×2 particles are presented in Fig. 4.6b. Since our technique allows us to obtain analytical results, the values of γ_1 and γ_2 can easily be optimized given the requirements for the separation. Again, we can calculate the slope at the origin (like in Eq. 4.10) to find the conditions for the existence of ϵ_{c_1} and ϵ_{c_2}. Here, we find that $\gamma_1\gamma_2 < 1$ (i.e., a positive bias) is necessary to obtain non-zero critical fields, whereas $\epsilon_c = 0$ for $\gamma_1\gamma_2 \geq 1$. Finally, we also note that there is a region $\epsilon_{c_2} < \epsilon_0 < \epsilon_{c_3}$ where the largest particle moves faster while both move in the same direction.

A qualitatively similar experiment has been reported by Serwer and Griess [38]. They performed the fractionation of latex spheres using an asymmetric pulsed field during gel electrophoresis. In this particular case, the use of a gel means that trapping occurs randomly for both polarities. They demonstrated that it is possible to separate spheres close to some critical radius (which is dependent upon the concentration of the gel) by inducing motion in opposite directions for beads smaller or larger than this critical size. Finally, Austin *et al.* [39] have also experimentally studied the dynamics of particles in trapping systems. More precisely, they studied the percolative migration of DNA molecules in random distributions of traps. This constitutes another experimental setup that we could model using our calculation technique.

This distribution of traps can also be used to illustrate how it is possible to manipulate two particles of the same size but with different electric charges. Figure 4.7 shows a similar

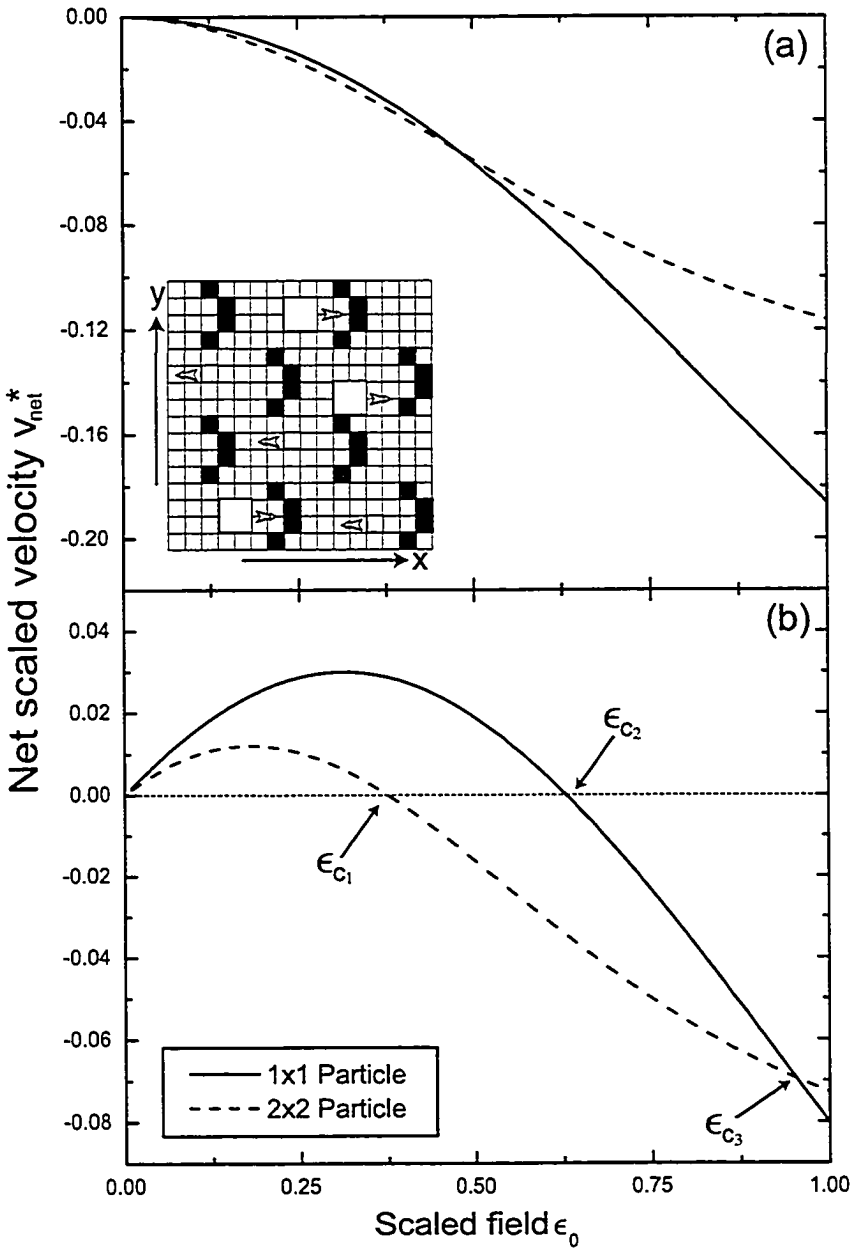

Figure 4.6: (a) Net velocities of 1×1 and 2×2 particles driven by a unbiased AC external field applied along the x-axis ($\gamma_1 = 1$ and $\gamma_2 = 1$; see Fig. 4.4). The trapping distribution of obstacles is shown in the inset. The two lines cross at $\epsilon_0 \approx 0.48$. (b) We now apply a positively biased AC field ($\gamma_1 = 1$ and $\gamma_2 = 1/2$). There is a region $\epsilon_{c_1} < \epsilon_0 < \epsilon_{c_2}$ where the two particles move in opposite directions. Here, $\epsilon_{c_1} \approx 0.37$ and $\epsilon_{c_2} \approx 0.63$. Furthermore, in the region $\epsilon_{c_2} < \epsilon_0 < \epsilon_{c_3}$, with $\epsilon_{c_3} \approx 0.95$, both particles move in the same direction but the large particle migrate faster than the small one.

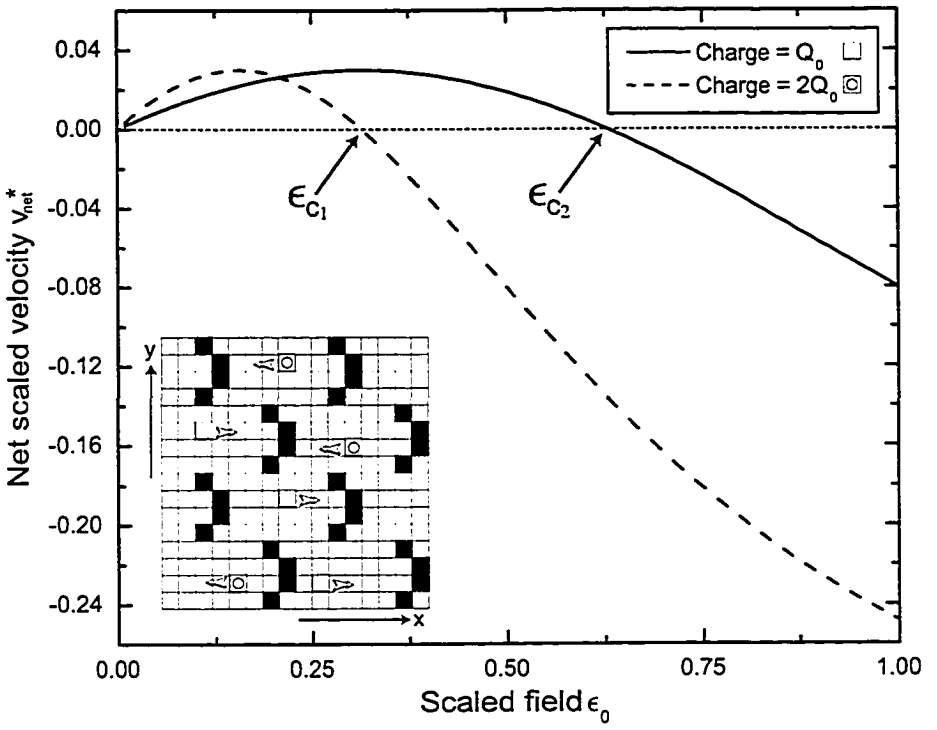

Figure 4.7: Net velocities of two 1×1 particles of charge Q_0 and $2Q_0$ driven by a biased AC external field applied along the x-axis ($\gamma_1 = 1$ and $\gamma_2 = 1/2$; see Fig. 4.4). The trapping distribution of obstacles is shown in the inset. The particles move in opposite directions if the field is in the region $\epsilon_{c_1} < \epsilon_0 < \epsilon_{c_2}$, with $\epsilon_{c_1} \approx 0.31$ and $\epsilon_{c_2} \approx 0.63$.

system, but this time for two particles of size 1×1 with different charges (Q_0 and $2Q_0$). The second curve is actually similar to the first one, except for the change of variable $\epsilon = 2\epsilon_0$. Since the original curve has a non-zero critical value $\epsilon_{c_2} \approx 0.63$, the second curve has a different critical value $\epsilon_{c_1} \approx 0.31$ and there is a large range of field intensities ϵ_0 where the two particles move in opposite directions. This would certainly be the best possible situation for separation purposes!

Funnels

The next example is also an asymmetric distribution of obstacles (see inset of Fig. 4.8). Here, the obstacles form asymmetric funnels with two different sizes of openings. Notice that the smaller funnels act like traps in the $+x$ direction for the 2×2 particles due to

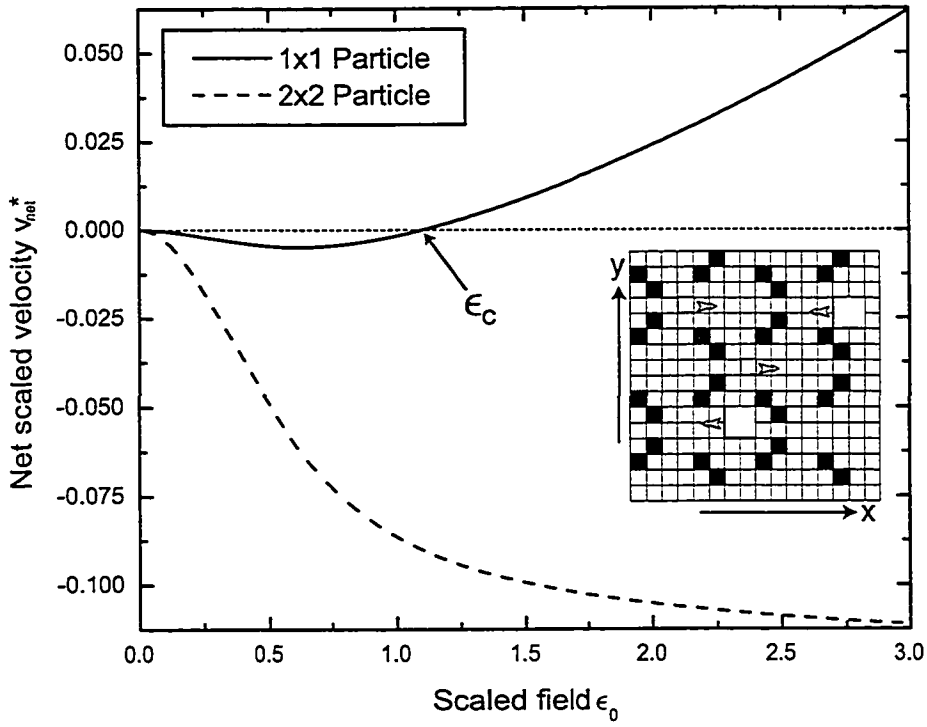

Figure 4.8: Net velocities of 1 × 1 and 2 × 2 particles driven by a non-biased AC external field applied along the x-axis ($\gamma_1 = \gamma_2 = 1$: see Fig. 4.4). The funnel-like obstacles are shown in the inset. For fields $\epsilon_0 > \epsilon_c \approx 1.1$, the particles move in opposite directions.

their small aperture. In the opposite direction, we have wider funnels that cannot trap either particle. This specially designed sieve has a major effect on the velocity of the larger particle. In fact, it is now possible to get velocities of opposite signs just by using a non-biased time-symmetric AC field. Results for a square AC field (with $\gamma_1 = \gamma_2 = 1$) are presented in Fig. 4.8. We can see that there is a critical value of the external field $\epsilon_c \approx 1.1$ above which the two kind of particles move in opposite directions. Notice that this spatial separation is performed without any net external force. In this case, the absolute difference in velocity always increases with the field ϵ_0.

4.4 Angular separations

The three systems presented previously were used to perform standard separations parallel to the direction of the external field. Separation is achieved because different molecular

species migrate over different distances in a fixed amount of time. The fact that the net displacement along the field direction is due to the symmetry of sieving systems along the y-axis. We will now present y-asymmetric deflecting distributions of obstacles where different sized particles have different velocities along the y-axis in response to a field ϵ_0 along the x-axis. In other words, the electrophoretic mobility becomes a tensor. This non-colinear velocity means that the particles can be separated along different angles.

Our first system is shown in the inset of Fig. 4.9. The obstacles form deflectors so that, if a constant external field is applied along the x-axis, the particles will have a non-zero velocity along the y-axis. For instance, consider a particle that tries to go from one corridor (the free rows between the rows of deflectors) to the next. If this particle diffuses in the $+y$-direction, the deflectors favor a transition to the upper corridor whereas if it is diffusing in the $-y$-direction, the obstacles force the particle to get back into its original corridor. A similar effect would obviously take place if the field were pointing, e.g., in the $+y$ direction.

Figure 4.9 presents the angular deflection (in degrees) with respect to the x-axis for 1×1 and 2×2 particles in this system of *deflectors*. We first notice that the deflection angle decreases when the external field ϵ_0 increases. This is explained by the fact that the lateral probability of transition (given by $P_\perp$) decreases when ϵ_0 increases. In the limit of very high field intensities, the ratio between the number of jumps along the y axis and the number of jumps along the x axis, which is directly related to the deflection angle, goes to zero. Secondly, Fig. 4.9 shows that small particles are always more deflected than large ones. This difference is explained by the fact that the deflection, as we mentioned in the previous paragraph, is due to the lateral diffusion of the particles. Since the 2×2 particles have a smaller diffusion coefficient than the 1×1 ones, they are less deflected.

This system is qualitatively similar to the microfabricated DNA angular sieves studied by Austin and co-workers [40, 41, 42, 43]. These authors observed the electrophoretic trajectories of DNA molecules in a series of deflectors similar to the ones shown in the inset of Fig. 4.9. They recorded the number of row changes (up and down) and the number of deflectors met along the path. The difference between the up and down transitions then give a probability per deflector (Δp) to move to another row, which is equivalent to our deflection angle. Typical experimental results [42] show that Δp seems to start at a finite value for $\epsilon_0 = 0$ and then decreases to zero when the external field increases. In short, these

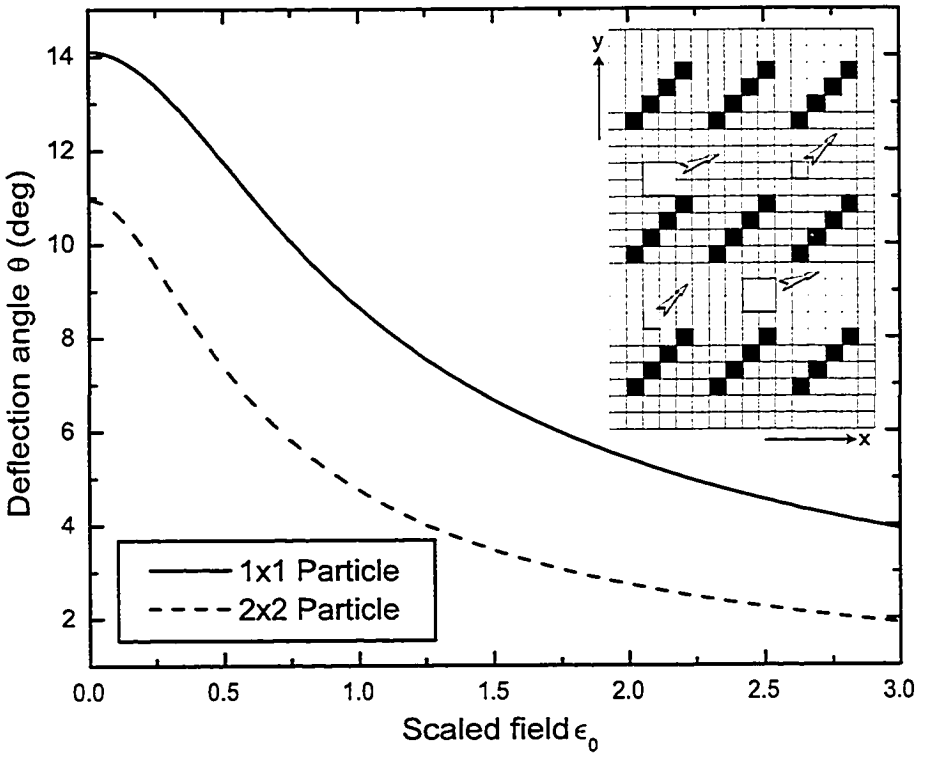

Figure 4.9: Deflection angle in degrees ($\theta = \arctan(v_y^*/v_x^*)$) of 1×1 and 2×2 particles driven by a constant (DC) external field pointing in the $+x$ direction. The distribution of tilted obstacles is shown in the inset. Note that the small particle is more deflected than the large one.

experimental results are qualitatively similar to our Fig. 4.9. However, the theoretical curve [41] proposed by Austin *et al.* seems to fail when $\epsilon_0 \to 0$. In fact, their theory predicts no deflection when $\epsilon_0 = 0$ whereas the data clearly shows a finite (maximum) deflection angle in this limit. These authors attribute this discrepancy [42] to several simplifying assumptions of their theory. For example, they suppose that the field is uniform (even near the non-conducting obstacles). Although this assumption is clearly inaccurate (see Ref. [43] for a discussion about the curvature of the field lines near the deflectors), our results indicate that the discrepancy is not due to this since we too have assumed straight field lines. Indeed, we do reproduce a finite deflection angle at $\epsilon_0 = 0$. Instead, we think that the failure of their original model to predict this feature is due to their neglect of the diffusion along the direction of the external field. In the high field limit this approximation

is acceptable because motion due to diffusion along the field direction is negligible compared to the net drift. This is no longer true when the field is very small. For example, the mean first passage time between one column of deflectors and the next does not increase to infinity when ϵ_0 goes to zero. Instead, it is limited to the Brownian time for free diffusion. In fact, we can intuitively understand the deflection at $\epsilon_0 = 0$ just by taking a look at the angular dispersion of particles after an unbiased random walk in a distribution of deflectors: the gas of particles then presents a preferential orientation (see Fig. 4.10). In other words, the particles spread in an elliptic cloud inclined with respect to the x-axis. Contrary to the case of a free solution, where all diffusion directions are equiprobable, deflectors induce a preferential diffusion direction which correspond to the deflection direction when $\epsilon_0 = 0$. In an anisotropic system, the diffusion tensor is not diagonal, even at zero field.

Finally, we present a second example of deflectors in which the large particles, contrary to what we saw in the previous system, are more deflected than the small ones (Fig. 4.11). The results show that the 2×2 particles are more deflected than the 1×1 ones even though their lateral diffusion coefficient is smaller. This qualitative change in the performance of the angular sieve is due to the fact that the distance between the rows of deflectors is now smaller than the size of the large particles. Therefore, when a 2×2 particle goes around a deflector, it has to diffuse laterally (downward) to avoid the next one while the 1×1 particles can actually drift pass several deflectors before they diffuse laterally and hit another deflector. The velocity of the larger particles is thus reduced along the x-axis and increased along the y-axis, giving large deflection angles. This shows that one can design deflector sieves to work in different ways, an idea that has yet to be tested.

4.5 Jamming in many-particles problems

We will now show that it is possible to use our calculation technique to study the impact of the concentration of particles on their average velocity. Up to now, all the results presented in this thesis were obtained for a single particle migrating through specific distributions of immobile obstacles with periodic boundary conditions. As we saw, our method simply lists the sites the particle can occupy and then uses simple master equations to calculate the probabilities for the particle to be on each of these sites. In a language more typical of

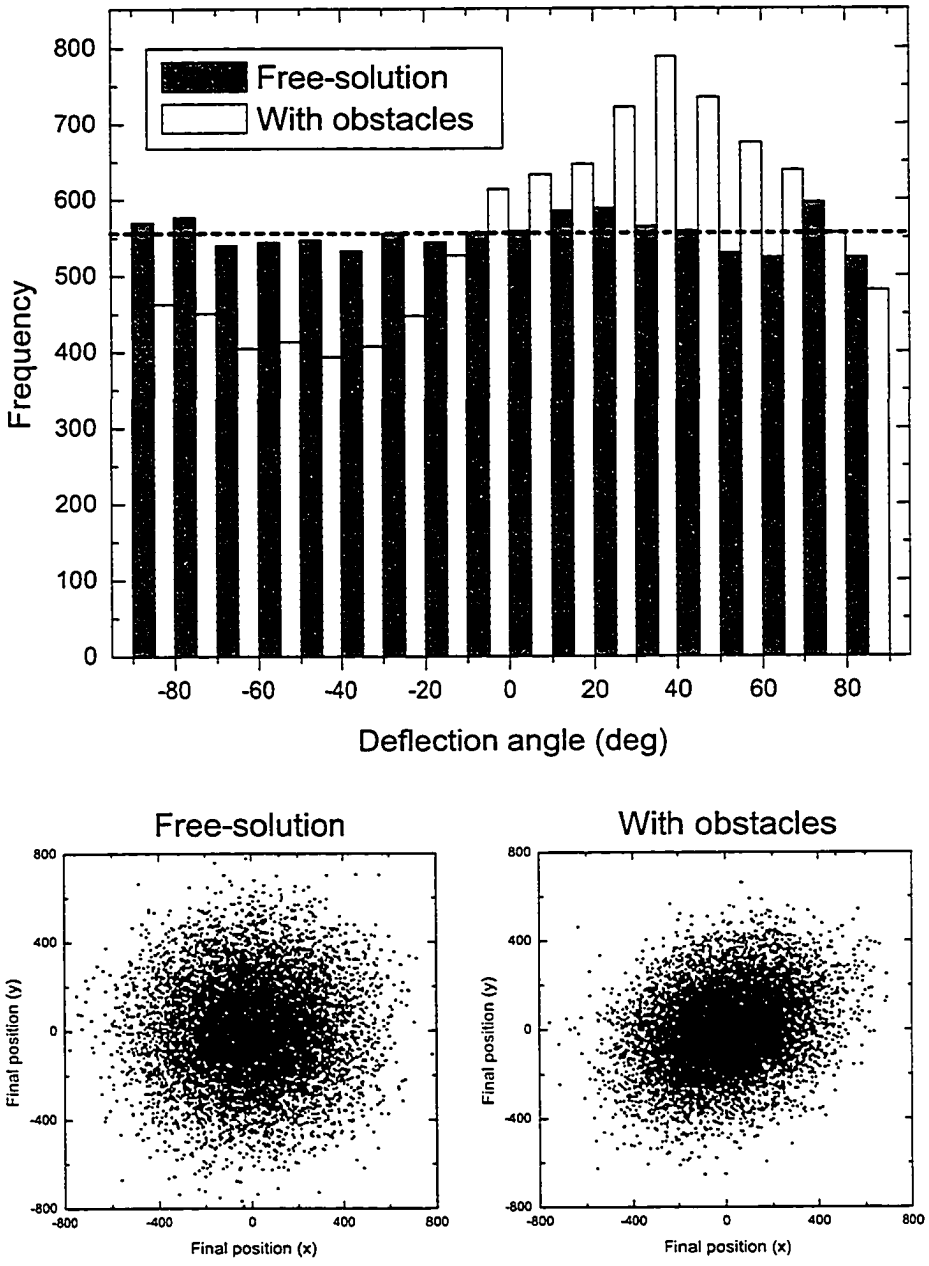

Figure 4.10: Comparison of the field-free trajectories of 10000 particles for a free-solution case and a distribution of deflectors (the one shown in the inset Fig. 4.9). The histograms represent the distribution of the final angular position of the particles in both systems. The dashed line shows the uniform expected result for free-solution. These histograms clearly show that the presence of deflectors induces a preferential angular direction, even without any driving force. The two bottom graphs show the spatial distributions of the particles. The calculation of the correlation coefficient for these two distributions ($\rho = 0.023$ and $\rho = 0.276$, respectively [44]) also confirms the influence of the deflectors on the field-free angular position.

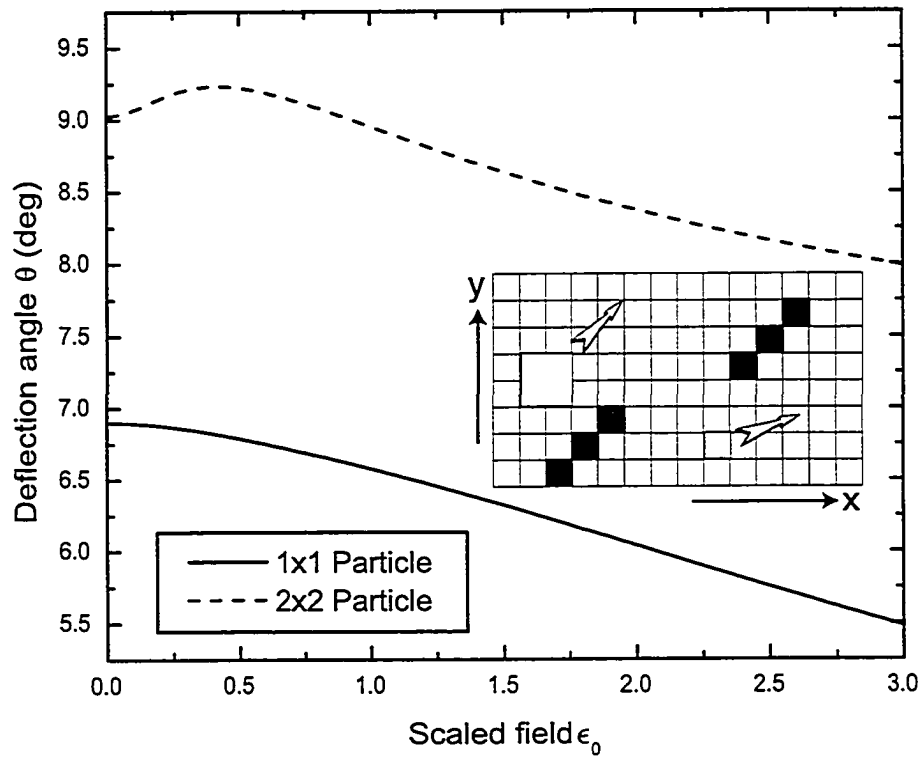

Figure 4.11: Deflection angle in degrees ($\theta = \arctan(v_y^*/v_x^*)$) of 1×1 and 2×2 particles driven by a constant (DC) external field applied along the x-axis. The distribution of tilted obstacles is shown in the inset. Here, the small particles are less deflected than the large ones. The y-velocity of the large particles is increased by the fact that the corridors between the rows of deflectors are only one unit in height.

statistical physics, we enumerate all the states in the phase space of the system as well as all the possible transitions between these states. Once these elements are known, it is possible to calculate exactly all the transport properties (as well as the average configurational properties) of the system.

If we want to study a system with $n > 1$ particles, we still have to list the sites that can be occupied by the particles. However, we must also enumerate all the different ways one can place n particles simultaneously on these sites. This give the number of *configurations* for the system of particles and obstacles. We must then enumerate the one-particle transitions that are possible between these configurations. Finally, we can use master equations to calculate the probability to find a particular configuration of the phase space during the migration of the particles in response to the external field . Although this approach is

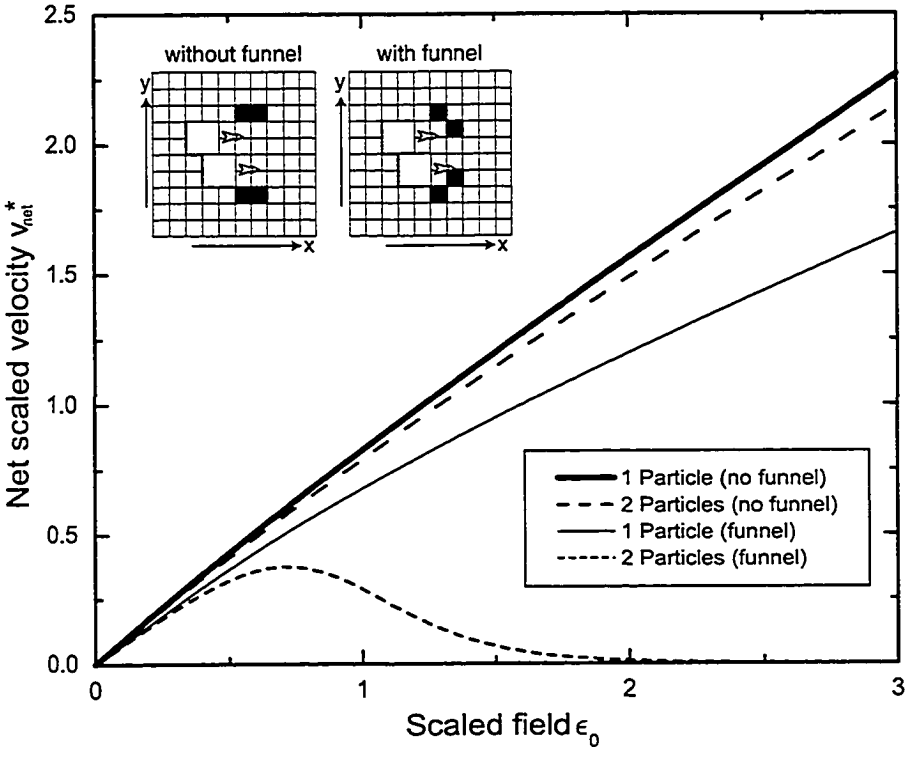

Figure 4.12: Scaled velocities v_x^* vs scaled external field ϵ_0 for 2×2 particles in the two different distributions of obstacles shown in the inset. The top two curves show the mean velocity of one and two particles in a system where jamming cannot be observed (no funnel). The two other curves were obtained with the second system where two particles can be trapped together in a funnel. The exponential decrease of the velocity at high field is a direct consequence of the jamming.

rather straightforward, the size of the resulting matrices (which is actually the number of configurations in the phase space) one must solve increases as $\sim N^n$, where N is the number of sites that can be occupied by the n particles. Therefore, we are limited to small values of n (the number of particles) and N (proportional to the lattice size) with the currently available computers.

There are two reasons to study finite concentrations of analytes. First, it is well-known that steric interactions between analytes decrease their mobility and diffusion coefficient. Second, some non-trivial *cooperative* effects can take place at finite concentrations. Figure 4.12 presents an example of such a non-trivial effect. The top two curves give the mean velocity when we have one or two particles of size 2×2 migrating through the distribution

of obstacles shown in the left-hand side of the inset. The velocity is slightly reduced by the increased concentration of particles (the curve shifts downward when we go from $n = 1$ to $n = 2$). This slight decrease was expected since each particle acts as an obstacle for the other one. Notice that the curve is not qualitatively affected by the addition of a second particle.

Let's now compare these results to the one obtained with a slightly different distribution of obstacles (see the right-hand side of the inset in Fig. 4.12) where two particles can be trapped together in a narrow funnel. The concentration of obstacles has not changed. The mean velocities found for one and two particles are given by the bottom two curves in Fig. 4.12. The qualitative differences between these two curves clearly illustrates the impact of the jamming at high field and the importance to have a model that can deal with such situations. The velocity decreases exponentially with the field intensity in the presence of jamming, a characteristic of thermally activated trapping systems. Here, the trap auto-organizes when the two particles are driven towards the bottom of the funnel by the electric forces.

4.6 Discussion

In previous chapters, we presented the basic elements of our new method to calculate the exact (lattice) velocity of a single particle in the presence of a field of arbitrary intensity, but no comparison between different species of particles was made. One of the key points of the current chapter is thus that one must be very careful when *scaling* the velocities of different sized or charged particles. Indeed, velocities cannot be compared, and sieving systems analyzed, if the microscopic parameters that characterize the particles are not properly included in the model's renormalized parameters. We believe that our model can now be used to assist in the development of high-field electrophoretic separation technologies, at least at the qualitative and semi-quantitative level. As such, it allows us to study a variety of nonlinear phenomena and new separation concepts.

We presented many non-trivial examples in the limit of a thick Debye layer ($\lambda_D \gg R$), where the separation factors are normally the particle's size R and charge Q. We showed a few examples using the scaling factors α and β, but the number of possibilities is extremely

large and specific experimental systems would have to be carefully analyzed. Treating three-dimensional cases is no more difficult than treating two-dimensional systems; we chose the latter for simplicity and because they nicely correspond to simple microfluidic systems. We also showed how the scaling could be done in the thin diffuse layer limit (also called the Smoluchowski limit), in which case the only relevant separation parameter is the surface charge density σ. However, generalization beyond (i.e., intermediate between) these limits is not straightforward due to the complexity of the relation between the velocity and the fundamental parameters characterizing the particles [45].

Our model is quite useful to understand high-field experimental results. Some of our examples included strong trapping in dead-ends, an effect that has been exploited for the fractionation of particles by pulsed field gel electrophoresis [38]. Using our approach, it is now possible to carry out a complete modelling study of such nonlinear effects and suggest new separation ideas. We also showed that deflector systems can be better understood using our calculations. In particular, we could qualitatively explain the experimental results obtained by Austin *et al.* [40, 41, 42, 43], even when $\epsilon_0 \to 0$; previous theoretical work could not explain the finite deflection angle in this limit. Other novel ratchet and separation systems we could study using our model include those of Astumian [46] and Ertas [47].

In Sec. 4.5, we further generalized our model, using the concept of a multi-particles phase-space, to study the effect of a finite concentration of particles (analytes) on their collective average velocity. This aspect of the problem has not been looked at before. We showed that quantitative and qualitative changes can be observed in the dynamics in some distributions of obstacles, including jamming in narrow passages (a phenomenon that is well-known in granular materials). However, the computational needs for this type of calculations increase extremely rapidly with the concentration C of analytes, and we are currently limited to rather small systems. An interesting complement to this approach would be to study the dynamics of *holes* when the concentration of particles is very high. In other words, we could easily apply the calculation technique for a mirror system of 3 holes to study N-3 particles (where N is the number of free sites). This idea remains to be explored. Of course, we can always use Monte Carlo simulations and our theoretical equations to obtain approximate numerical results where exact matrix calculations cannot be done with the current computing equipment.

The pulsed-field results presented here are only valid in the limit were the time duration of the pulses are much larger than the microscopic relaxation times of the particles (this is called the zero-frequency limit). This is not always the case [34]. Anomalous diffusion (which takes place at short times in disordered systems [48]) and finite-frequency pulses can be studied using a non-steady-state enumeration approach. The combination of both techniques can allow us to cover a large part of the spectrum of possible frequencies and time scales.

A major advantage of our calculation technique is that we can sometimes obtain exact analytical functions for the various DC and AC velocities using softwares like Maple. This can be quite useful for optimization purposes. For instance, exact numerical or (preferably) analytical results can provide a better understanding of the effects of the control parameters (like γ_1 and γ_2) on the quality of the separation. Moreover, exact calculations allow us to study subtle effects, which is not necessarily the case when we use Monte Carlo simulations. For example, the small difference between the two curves at low field in Fig. 4.6a would probably be hidden by the statistical error bars that characterize Monte Carlo data. Similarly, the small negative velocity of the 1×1 particle at low field ($\epsilon_0 < \epsilon_c$) in Fig. 4.8 would probably be impossible to observe.

However, the model is not yet complete. First, without changing the fundamental elements of the model itself, it is possible to represent more realistic systems (like circular or cylindrical obstacles) by using finer mesh sizes a to extrapolate towards the limit of the continuum ($a \rightarrow 0$) [19]. Obviously, this operation will require more computational resources, but it is doable numerically with current supercomputers. Secondly, a major improvement would be the introduction of curved field lines to treat the case of non-conducting obstacles (this was done in the limit where $\epsilon_0 \rightarrow 0$ [12]). Our present technique is limited to systems where the field is applied along one the principal orthogonal axes. Trapping systems build with insulating materials present completely different dynamical properties (in high field conditions) due to the fact that the field lines (and consequently the particles) find their way out of the dead ends (see Ref. [43] for example). The incorporation of curved field lines in a high field situation will be discussed in chapter 6. Finally, we still don't know how to obtain the exact diffusion coefficient D in the presence of an high external field. This coefficient would tell us about the dispersion of the particles around the exact average

position obtained from the velocity calculation. Note that the diffusion coefficient will be field-dependent under such conditions. Dispersion is a major limiting factor for separation processes, and a complete theory requires a calculation of D. Even with a Monte Carlo algorithm, the evaluation of the diffusion coefficient in the presence of a high external field is not straightforward. Current algorithms are limited to small values of the field (we discussed this issue in chapter 2). However, it is indeed the limit of very high field intensities that is relevant for the modelling of sieving and microfluidic systems.

Chapter 5 Diffusion in the Presence of a Drift

Diffusion plays an important role in a great number of physical, chemical and biological phenomena. It is thus relevant to develop simulation models for these dynamical processes that allow us to calculate the diffusion coefficient. One of the most commonly used approach is to discretize the space with a lattice on which a random-walker can evolve (like the method we presented in chapter 2). We demonstrated that this discretization is relatively simple when we are interested in the average velocity of the particle. However, as we will show in this chapter, the calculation of the diffusion coefficient is then quite subtle. Our objective is to derive a model and a calculation technique that give the right free-solution diffusion coefficient when an external field is applied. If this is achieved, our method could be, at least, used with a Monte Carlo simulation algorithm to obtain both the velocity and the diffusion coefficient in the presence of any distribution of obstacles.

5.1 Diffusion in one dimension

In order to fully understand the diffusion properties of a random walk, it is convenient to start with a one-dimensional ($1D$) study of the problem. As we mentioned in Sec. 2.1, Eqs. 2.1 and 2.3 allow us to correctly evaluate the velocity of our random walker in $1D$ with respect to the external field ϵ. We will now try to use these equations to calculate the free-solution diffusion coefficient D_0, which is generally given by:

$$D_0 = \frac{\langle \Delta x^2 \rangle}{2\tau}, \tag{5.1}$$

where $\langle \Delta x^2 \rangle$ is variance of the displacement of the particle along the x-axis during the time step τ. This variance can be obtained from the transition probabilities (Eq. 2.3) via the calculation of the average displacement $\langle x \rangle$ and the average squared displacement $\langle x^2 \rangle$:

$$\begin{aligned}\langle \Delta x^2 \rangle &= \langle x^2 \rangle - \langle x \rangle^2 \\ &= a^2(p_+ + p_-) - (a(p_+ - p_-))^2 \\ &= a^2 - (a \tanh \epsilon)^2 \\ &= a^2 \operatorname{sech}^2 \epsilon \,.\end{aligned} \tag{5.2}$$

The free-solution diffusion coefficient is then given by:

$$\begin{aligned}D_0 &= \frac{\langle \Delta x^2 \rangle}{2\tau} \\ &= \frac{a^2 \operatorname{sech}^2 \epsilon}{2\tau_B} \frac{\epsilon}{\tanh \epsilon} \\ &= \frac{a^2}{2\tau_B} \left(\frac{\epsilon}{\sinh \epsilon \cosh \epsilon} \right) \\ &= \frac{a^2}{2\tau_B} \left(1 - \frac{2}{3}\epsilon^2 + \frac{14}{45}\epsilon^4 + O(\epsilon^6) \right) .\end{aligned} \tag{5.3}$$

where we used τ given by Eq. 2.1. However, the free-solution diffusion coefficient characterizes the spreading of the particles around their average position. It is thus expected that the diffusion coefficient will be constant whatever the value of the external field (the field only affects the average position, or the velocity, of the particles). Therefore, the result of Eq. 5.3, which is a decreasing function of ϵ, is clearly incorrect. More precisely, Eq. 5.3 gives the right value of $a^2/2\tau_B$ only when $\epsilon = 0$, or up to the first order in ϵ.

This discrepancy with the expected result can be explained by the fact that Eq. 5.1 only takes into account of the spatial fluctuations $\langle \Delta x^2 \rangle$ coming from the Brownian motion of the particles along the path. However, in presence of an external force, a second source of diffusion has to be considered: the fluctuations in the time duration of a jump, $\langle \Delta \tau^2 \rangle$. It has been shown [35] that, in presence of an external field, both spatial and temporal fluctuations have to be considered in the calculation of the diffusion coefficient using the following expression:

$$D_0 = \frac{\langle \Delta x^2 \rangle}{2\tau} + \frac{v_0^2 \langle \Delta \tau^2 \rangle}{2\tau} \,, \tag{5.4}$$

where $v_0 = \epsilon a / \tau_B$ is the steady-state velocity of the particle (Eq. 2.4). Thus, in order to get the right diffusion coefficient, we need the expression for the variance of the time duration of a jump $\langle \Delta \tau^2 \rangle$. This value was also previously obtained from the resolution of the first passage problem in $1D$ (like τ and $p_\pm$; see Ref.[20] for details):

$$\langle \Delta \tau^2 \rangle = \frac{\tanh \epsilon - \epsilon \operatorname{sech}^2 \epsilon}{\epsilon^3} \tau_B^2 \,. \tag{5.5}$$

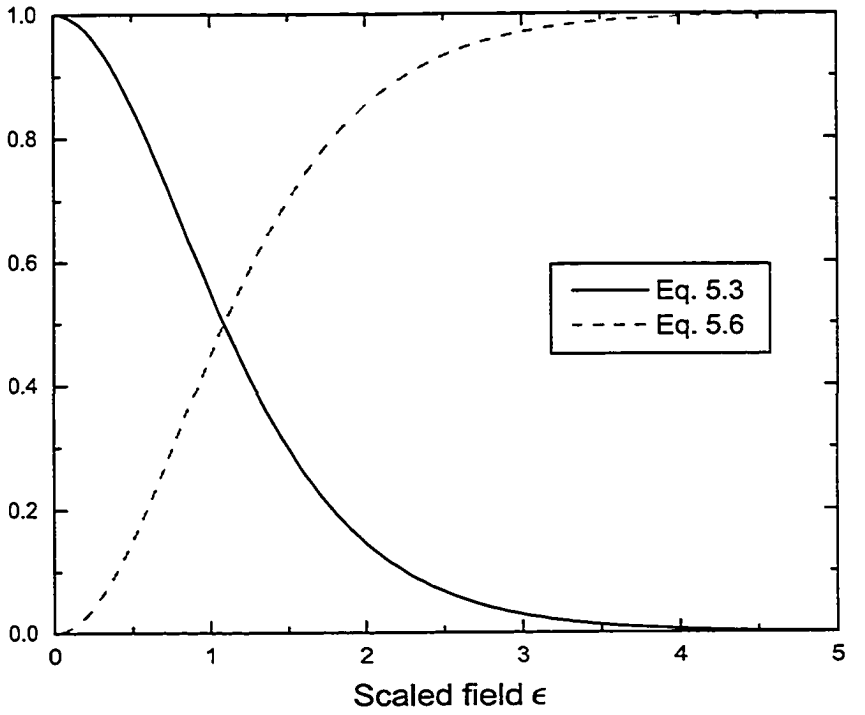

Figure 5.1: Equations 5.3 and 5.7 (in units of $a^2/2\tau_B$) vs the scaled field ϵ.

In the limit of $\epsilon \to 0$, we have:

$$\langle \Delta\tau^2 \rangle \big|_{\epsilon \to 0} = \frac{2}{3}\tau_B^2 \,. \tag{5.6}$$

In a free solution, the second term of Eq. 5.4 thus reduces to:

$$\frac{v_0^2 \langle \Delta\tau^2 \rangle}{2\tau} = \frac{a^2}{2\tau_B}\left(1 - \frac{\epsilon}{\sinh\epsilon\cosh\epsilon}\right) . \tag{5.7}$$

This last expression and the first term of Eq. 5.4 are plotted in Fig. 5.1. The first curve (Eq. 5.3) illustrates why we get the right diffusion coefficient only for $\epsilon = 0$ when we ignore the temporal fluctuations. According to Eq. 5.4, the correct free-solution diffusion coefficient D_0 is simply given by the sum of Eqs. 5.3 and 5.7 (respectively the spatial and temporal fluctuation terms):

$$D_0 = \frac{a^2}{2\tau_B}\left(\frac{\epsilon}{\sinh\epsilon\cosh\epsilon}\right) + \frac{a^2}{2\tau_B}\left(1 - \frac{\epsilon}{\sinh\epsilon\cosh\epsilon}\right) = \frac{a^2}{2\tau_B} , \tag{5.8}$$

which is not a function of the external field, as it should.

In conclusion, the fluctuations of the jumping time τ are a necessary feature that we have to integrate in our random walk model when we want to study the diffusion properties of a particle in the presence of a net drift. Obviously, this is also true when we perform Monte Carlo simulations. For instance, if we simulate the trajectories of a large number of particles (using $p_\pm$ for the transition probabilities and τ for the time step) and evaluate the spatial dispersion of these particles after a given period of time, the resulting diffusion coefficient is not constant as we change the external field. The only way to get the correct results is to introduce the temporal fluctuations using any time distribution function that has a mean value and a variance given by Eqs. 2.1 and 5.5, respectively. In a simulation, this condition can be minimally satisfied by changing the time step τ for the random increment $\tau \pm \sqrt{\langle \Delta\tau^2 \rangle}$ (where the sign is chosen randomly).

5.2 Time fluctuations with constant time steps in one dimension

As we demonstrated in the previous section, the time fluctuations have to be considered to get the proper diffusion properties. However, the calculation technique that we are trying to extend (chapter 2) needs a fixed time step to allow us to solve exactly the Monte Carlo algorithm. We will now present how we can introduce the temporal fluctuations without changing the time increment simply by adding a probability to remain on the same lattice site.

In the model described in chapter 2, the particle always tries to jump onto one of the neighboring sites. Let's now introduce a probability $s'_\pm$ for the particle to stay on the same lattice site during the given time step. In order to respect the normalization condition, the two new transitions probabilities $p'_\pm$ are then given by:

$$p'_\pm = (1 - s'_\pm)p_\pm \,. \tag{5.9}$$

The time increment has also to be rescaled by the same factor

$$\tau' = (1 - s'_\pm)\tau \,, \tag{5.10}$$

in order to conserve the value of the free-solution velocity of the particle:

$$v'_0 = \frac{(p_+{}' - p_-{}')a}{\tau'} = \frac{(p_+ - p_-)a}{\tau} = v_0 \,. \tag{5.11}$$

We now have a system in which, at each time step τ', the particle jumps onto one of the $\pm$ sites with the probability $p'_{\pm}$ or stay on the same site with the probability $s'_{\pm}$. Our idea here is to use the probability $s'_{\pm}$ as a free parameter that we set in order to get the desired variance of the average *real* jumping time. To do so, we just have to evaluate the average period of time $\langle\tau\rangle$ between two jumps of the particle as a function of $s'_{\pm}$:

$$\begin{aligned}
\langle\tau\rangle &= \overbrace{(1-s'_{\pm})\tau'}^{1^{st}\text{attempt}} + \overbrace{s'_{\pm}(1-s'_{\pm})2\tau'}^{2^{nd}\text{attempt}} + \overbrace{{s'_{\pm}}^2(1-s'_{\pm})3\tau'}^{3^{rd}\text{attempt}} + \dots \\
&= (1-s'_{\pm})\tau' \sum_{i=1}^{\infty} i {s'_{\pm}}^{i-1} \\
&= \frac{\tau'}{1-s'_{\pm}} \\
&= \tau\,,
\end{aligned} \tag{5.12}$$

which is equal to τ, as it should. We also easily obtain that $\langle\tau^2\rangle$ is given by:

$$\begin{aligned}
\langle\tau^2\rangle &= \overbrace{(1-s'_{\pm})\tau'^2}^{1^{st}\text{attempt}} + \overbrace{s'_{\pm}(1-s'_{\pm})4\tau'^2}^{2^{nd}\text{attempt}} + \overbrace{{s'_{\pm}}^2(1-s'_{\pm})9\tau'^2}^{3^{rd}\text{attempt}} + \dots \\
&= (1-s'_{\pm})\tau'^2 \sum_{i=1}^{\infty} i^2 {s'_{\pm}}^{i-1} \\
&= \frac{(1+s'_{\pm})\tau'^2}{(1-s'_{\pm})^2} \\
&= (1+s'_{\pm})\tau^2\,.
\end{aligned} \tag{5.13}$$

Using the two last results, we can determine the required probability $s'_{\pm}$ as follows:

$$s'_{\pm} = \frac{\langle\tau^2\rangle - \langle\tau\rangle^2}{\langle\tau\rangle^2} = \frac{\langle\Delta\tau^2\rangle}{\tau^2}\,. \tag{5.14}$$

So the probability to stay put has to be equal to the ratio of Eqs. 5.5 and 2.1 to get the proper temporal fluctuations in the net jumping rate:

$$s'_{\pm} = \frac{\coth\epsilon}{\epsilon} - \operatorname{csch}^2\epsilon\,. \tag{5.15}$$

In the limit of $\epsilon \to 0$, this result becomes:

$$s'_{\pm}\big|_{\epsilon\to 0} = \frac{2}{3}\,. \tag{5.16}$$

It is now possible to correctly evaluate the free-solution diffusion coefficient using only the

spatial part of Eq. 5.4 (first term):

$$D_0 = \frac{\langle \Delta x^2 \rangle'}{2\tau'} = \frac{\langle x^2 \rangle' - \langle x \rangle'^2}{2\tau'} = \frac{a^2}{2\tau'}\left(p'_+ + p'_- - (p'_+ - p'_-)^2\right) = \frac{a^2}{2\tau_B}, \tag{5.17}$$

which is the expected result (see Eq. 5.8). We used $\langle x^2 \rangle' = a^2(p'_+ + p'_-)$ and $\langle x \rangle' = a(p'_+ - p'_-)$. Notice that we get the right result even though the jumps are attempted at a constant rate, which was not the case before.

Finally, we want to point out that the probability to stay put given by Eq. 5.15 is the unique solution that gives the correct values for both v and D_0. That means that any other value of $s'_\pm$ will lead to an incorrect velocity or diffusion coefficient (depending how we renormalize the other probabilities).

5.3 Higher-dimensional models

In Sec. 2.4, we presented transition probabilities ($P_\pm$ and $P_\perp$) and a time duration (T) valid in any dimension d for the calculation of the mobility. We already showed that these probabilities and time duration give the proper lateral diffusion coefficient (i.e., any direction perpendicular to the external field). However, in the direction of the field, we cannot get the right free-solution diffusion coefficient using only the spatial fluctuations:

$$\begin{aligned} D_{0_x} &= \frac{\langle \Delta X^2 \rangle}{2T} \\ &= \frac{\langle X^2 \rangle - \langle X \rangle^2}{2T} \\ &= \frac{a^2}{2T}\left(P_+ + P_- - (P_+ - P_-)^2\right) \\ &= \frac{a^2}{2\tau_B}\left(\epsilon \coth \epsilon - \frac{\epsilon^2}{d - 1 + \epsilon \coth \epsilon}\right) \\ &= \frac{a^2}{2\tau_B}\left(1 + \left(\frac{1}{3} - \frac{1}{d}\right)\epsilon^2 + \left(\frac{1}{3d^2} - \frac{1}{45}\right)\epsilon^4 + O(\epsilon^6)\right). \end{aligned} \tag{5.18}$$

In order to obtain the proper free-solution diffusion in d dimensions, we have to generalize the approach that we derived in the previous section.

Our objective is to add a probability to stay put (S') for a period of time (T') to introduce fluctuations in the net transition time in the direction of the field. We can carry

out the same calculations as we did in Sec. 5.2 with the following elements:

$$\begin{aligned} T' &= (1 - S')T\,, \\ P'_{\pm} &= (1 - S')P_{\pm}\,, \\ P'_{\perp} &= (1 - S')P_{\perp}\,, \end{aligned} \tag{5.19}$$

and look at this system as a one-dimensional problem in the direction of the external field. By that we mean that the lateral displacements in d dimensions (described by the probabilities $P'_{\perp}$ for all of the $2(d-1)$ non-biased directions) have to be considered as non-motion in the direction of the field. In other words, if we want to project a dynamical system ($P'_{\pm}$, $P'_{\perp}$ and S') onto a 1D system ($p'_{\pm}$ and $s'_{\pm}$), we need the following correspondence relations:

$$\begin{aligned} p'_{\pm} &= P'_{\pm}\,. \\ s'_{\pm} &= S' + 2(d-1)P'_{\perp}\,. \end{aligned} \tag{5.20}$$

The probability to stay put is then obtained by solving for S' in the following equation coming from Eqs. 5.19 and 5.20:

$$\frac{p'_{\pm}}{P_{\pm}(1 - S')} = \frac{s'_{\pm}}{S' + 2(d-1)P_{\perp}(1 - S')}\,. \tag{5.21}$$

The solution gives:

$$S' = \frac{(d-1) - \epsilon(d-2)\coth\epsilon}{\epsilon^2} - \operatorname{csch}^2\epsilon\,. \tag{5.22}$$

The free-solution diffusion coefficient in the direction of the field (the x-direction for example) is then obtained as described previously in Eq. 5.18:

$$D_{0_x} = \frac{\langle \Delta X^2 \rangle'}{2T'} = \frac{a^2}{2T}\left(P'_{+} + P'_{-} - (P'_{+} - P'_{-})^2\right) = \frac{a^2}{2\tau_B}\,. \tag{5.23}$$

Notice also that the diffusion coefficient along the y-axis is not affected by the addition of the probability S':

$$D_{0_y} = \frac{\langle \Delta Y^2 \rangle'}{2T'} = \frac{a^2}{2T}\left(P'_{\perp} + P'_{\perp} - (P'_{\perp} - P'_{\perp})^2\right) = \frac{a^2}{2\tau_B}\,. \tag{5.24}$$

Eqs. 5.23 and 5.24 will be satisfied in any dimensions as long as the field is along one of the cartesian axes. We also want to point out that the probability to stay put does not affect the calculation of the mobility because the transition probabilities and the jumping time

are rescaled with the same factor $(1 - S')$ in Eq. 5.19. We note that Eq. 5.22 reduces to Eq. 5.15 when $d = 1$.

However, there is a major problem with the last derivation: the probability to stay on the same site S' can be negative for $d \geq 3$. It is thus impossible to use these transition probabilities in more than $2D$ because the sum of all the other probabilities is greater than one ($P'_+ + P'_- + 2(d-1)P'_\perp > 1$). Finally, as we mentioned at the end of Sec. 5.2, it is not possible to renormalize these probabilities while preserving the proper free-solution mobility and diffusion coefficients simultaneously because the solution for $s'_\pm$ is unique.

This limitation can be understood when we start from $1D$. In fact, the probabilities are given by $P'_\pm = p'_\pm$ and $2(d-1)P'_\perp + S' = s'_\pm$. When we go from $1D$ to $2D$, we keep $p'_\pm$ but we reduce the probability to stay put to generate lateral motion. When we pass to higher dimensions, the new probabilities are subtracted from the remaining probability to stay put and so on. So, by definition, this approach has to be limited to a maximum number of dimensions. Unfortunately, this limit is for $d = 2$, which is very restrictive. We thus have to review the fundamental assumptions of our model if we want a method that will work for all dimensions d.

Appendix B presents another proof of the fact that we cannot derive a generalized set of probabilities in more than two dimensions. In short, we solved the basic equations that our model has to satisfy (normalization, free-solution velocity and diffusion) for transition probabilities and transition times, without any prior knowledge about these quantities. We demonstrate that, even though we have an infinite number of solutions, it is impossible get all the probabilities, for all values of the external field, bounded between 0 and 1 when $d \geq 3$.

The 2D case

The method presented in this section is limited to two-dimensional systems, but it still constitutes a major improvement since it is the first approach valid for any values of the external field. Monte Carlo simulations can now be performed on $2D$ systems with the following transition probabilities and time durations:

$$S' = \epsilon^{-2} - \operatorname{csch}^2 \epsilon \,, \tag{5.25}$$

$$P'_{\pm} = (1 - S')P_{\pm} = \frac{\coth^2 \epsilon - \epsilon^{-2}}{(1 + e^{\mp 2\epsilon})(1 + \tau/\tau_B)}, \tag{5.26}$$

$$P'_{\perp} = (1 - S')P_{\perp} = \frac{\coth^2 \epsilon - \epsilon^{-2}}{2(1 + \tau_B/\tau)}. \tag{5.27}$$

$$T' = (1 - S')T = \frac{(\coth^2 \epsilon - \epsilon^{-2})\tau\tau_B}{\tau + \tau_B}. \tag{5.28}$$

The algorithm is really simple and consists in these three steps:

1. On a square two-dimensional lattice, the displacement of the particle for the current iteration is selected according to the probabilities $P'_{\pm}$, $P'_{\perp}$ and S'.

2. If the destination site is free, the particle is moved, otherwise, it remains on the same site.

3. The clock is increased with the constant jumping time duration T'.

After a large number of iterations and with a large number of particles, the mobility and diffusion coefficients can be obtained from the statistics on the final positions of the particles. This approach is sufficient to study any two-dimensional system. In the next section, we will present a new algorithm that allows us to go beyond the $d = 2$ limit.

5.4 A new set of probabilities

The results of the previous section demonstrate that we need to derive a new way to describe the dynamics of a random walker if we want to study drift and diffusion properties in more than $2D$. We will now present a new approach to obtain the transition probabilities of an analyte that gives the right mobility and diffusion coefficients for all dimensions ($d \geq 1$).

The simultaneity principle

When we look carefully at the model derived in chapter 2, a basic rule of the random walk in more than $1D$ seems to be violated: *the statistical independence of the different directions.* Indeed, a jump in one direction appears to prohibit a jump in an orthogonal direction to

occur during the same period of time. Obviously, this is not quite true because the net rates of jump in each direction corresponds to the correct one-dimensional rates. It is a standard Monte Carlo rule that the jumps must be made along one direction at each time step (we never allow two or more simultaneous jumps in several directions). Since we demonstrated in Sec. 5.2 that we can correctly reproduce the dynamics in $1D$, we now derive a new set of probabilities where all the possible jumps in all the directions are simultaneously possible (or attempted) at each time step.

The free-solution case

Our new approach is to decouple the d dimensions in order to treat the dynamics in each direction using Eqs. 5.9, 5.10 and 5.15. The external field still has to be parallel to one of the cartesian axes. In the dimension parallel to the external field, the dynamics is governed by $p'_{\pm}$, $s'_{\pm}$ and τ', whereas in all other dimensions, the displacement is described by $p_{\perp} = 1/2$ and τ_B. For the moment, we do not need a probability to stay put in the orthogonal (unbiased) directions to get the right diffusion coefficient. As we will see in Eq. 5.30, the probability to stay put in this direction will be introduced via a temporal rescaling of the lateral dynamics.

The idea is to use the time step of the fastest process (τ') as the time step of our new set of probabilities. We thus have to rescale the probability $p_{\perp}$ using the time step τ':

$$p'_{\perp} = p_{\perp}\frac{\tau'}{\tau_B}\,. \tag{5.29}$$

We then have a probability to stay put in these directions given by:

$$s'_{\perp} = 1 - 2p'_{\perp}\,. \tag{5.30}$$

In the limit of $\epsilon \to 0$ and $\epsilon \to \infty$, this result becomes:

$$s'_{\perp}\big|_{\epsilon\to 0} = \frac{2}{3}\,, \tag{5.31}$$

$$s'_{\perp}\big|_{\epsilon\to \infty} = 1\,. \tag{5.32}$$

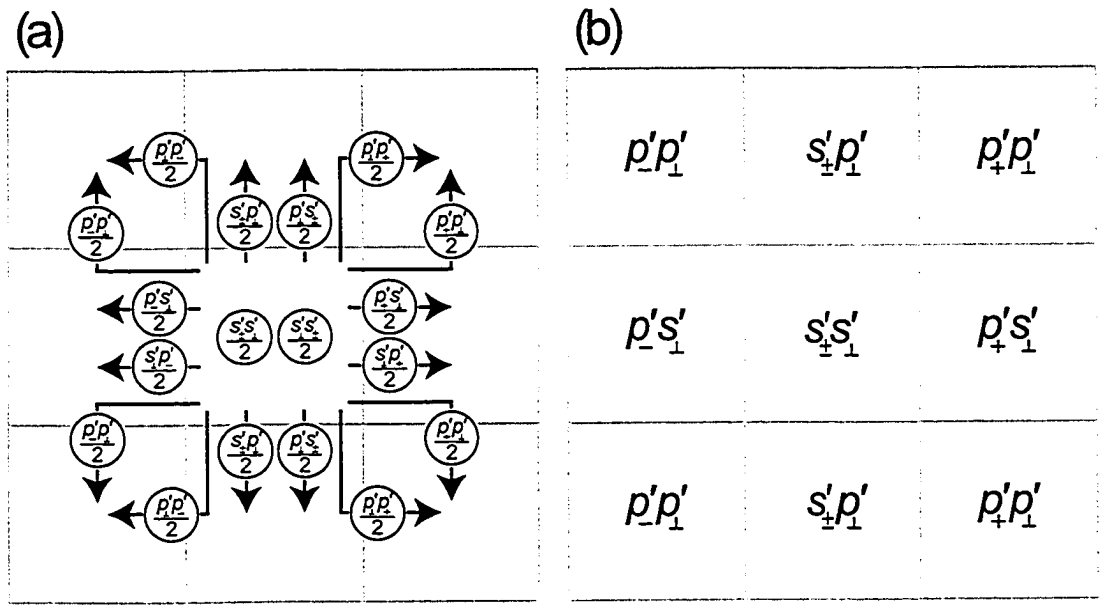

Figure 5.2: (a) Representation of all the possible paths that the particle can follow during a time step τ' if the jumps in all the directions are tried in free-solution. (b) The resulting transition probabilities.

We can now use these one-dimensional probabilities to develop the transition probabilities in d dimensions using the simultaneity principle (the d directions are statistically independent). Therefore, if a jump is attempted in all directions at each time step, the set of accessible sites where the particle can land now includes the diagonal neighbors. Figure 5.2 illustrates this approach for the $2D$ case with a free solution. This figure shows the different paths that the particle can follow during the time step τ'. These paths consist in all the possible combinations of the transition probabilities parallel and perpendicular to the field. Also, for each combination, we consider that all the permutations are equiprobable (this explains the factors of 1/2 in Fig. 5.2a). The representation of all these paths could seem useless (the final transition probabilities of Fig. 5.2b could directly be obtained from the one-dimensional probabilities), but these trajectories will be essential to determine the dynamics in presence of obstacles. It is straightforward to extend this approach to any other dimensions ($d > 2$). It is also easy to verify that all the probabilities will be bounded between 0 and 1 because they are obtained from the product of the correctly bounded one-dimensional probabilities.

Finally, we can verify that this set of probabilities gives the right free-solution velocity and diffusion coefficients in the field direction. It is easy to see that, whatever the value of d, the values of $\langle \Delta X \rangle'$ and $\langle \Delta X^2 \rangle'$ will always be given by $(p'_+ - p'_-)a = \langle \Delta x \rangle'$ and $(p'_+ + p'_-)^2 a^2 = \langle \Delta x^2 \rangle'$ respectively. These values will thus lead to the same results that we obtained in Eqs. 5.11 and 5.17. Therefore, the model introduced here does work for all dimensions $d \geq 2$. The problems faced in Sec. 5.3, which were due to the fact that the different spatial directions were indirectly coupled by the requirement that only one uni-axial jump can be made per time step, have been eliminated by making the d directions independent from each other and choosing τ' as the fundamental time step.

The collisions with the obstacles

Since this new model works fine in free-solution, the next step is to define how to deal with the presence of obstacles. The rule that we have to follow in case of a collision is the same as before, i.e. if a selected site is occupied by an obstacle, the corresponding jump is rejected and the analyte remains on the same site for this time step. So, when we want to write the transition probabilities in presence of an obstacle, we have to look carefully at all the possible paths that the particle can follow because some of the d attempted jumps that compose the complete jump could be rejected. An example of this procedure is illustrated in Fig. 5.3. We see that the two different trajectories that lead to the upper right corner now lead to different final positions due to the rejection of one of the two jumps that generate these paths. All other distributions of obstacles (in any dimensions) can be studied using the same approach.

The continuum limit

Obviously, this new way to define a collision with an obstacle has an influence on the dynamics of the particle near the obstacle. In fact, if we were to repeat the calculation of the mobility that we presented in Sec. 2.5 with our new set of probabilities, we would obtain slightly different mobilities. We can verify that this difference is only due to the definition of the collisions by comparing the two approaches in the continuum limit. This procedure consists in performing the same calculation for different lattice parameters ξa

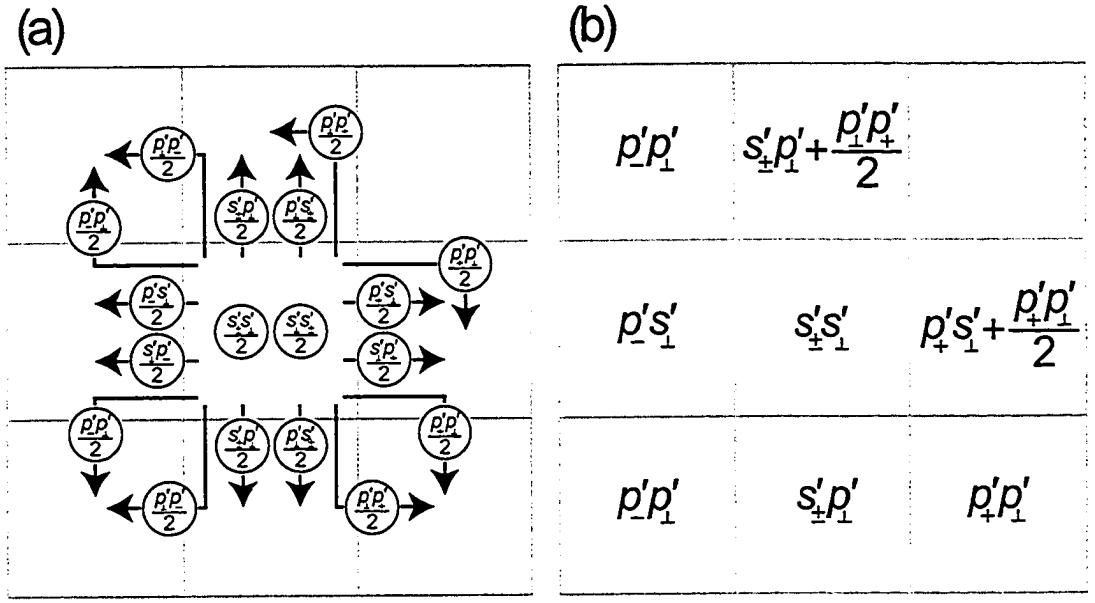

Figure 5.3: (a) Representation of all the possible paths that the particle can follow during a time step τ' if the jumps in all the directions are tried in presence of an obstacle. (b) The resulting transition probabilities. There are two ways to move to the forbidden site in upper right corner: "jump right + jump up" or "jump up + jump right". In both cases, the second jump is rejected and the final positions are now different (contrary to the free-solution case).

(with $0 < \xi \leq 1$) while the obstacle size a remains constant. We then extrapolate in the limit where $\xi \to 0$. Figure 5.4 shows the lattice representation of a square obstacle for three different values of ξ (the surface concentration of obstacles is kept constant to $C = 1/9$).

We compared the mobilities obtained with the transition probabilities of Secs. 2.2 and 5.4 for a wide range of ξ. Notice that the value of the field ϵ, which is proportional to the lattice parameter (Eq. 2.2), has to be rescaled by the factor ξ. Figure 5.5 presents four of these comparisons for different values of the field ϵ. We clearly see that the two approaches always converge in the limit where $\xi \to 0$. This new algorithm is thus equivalent to the one derived in chapter 2 in the continuum limit. Moreover, our new approach now gives the proper diffusion coefficient of a small analyte in free-solution and can thus be used to study mobility and diffusion coefficients simultaneously.

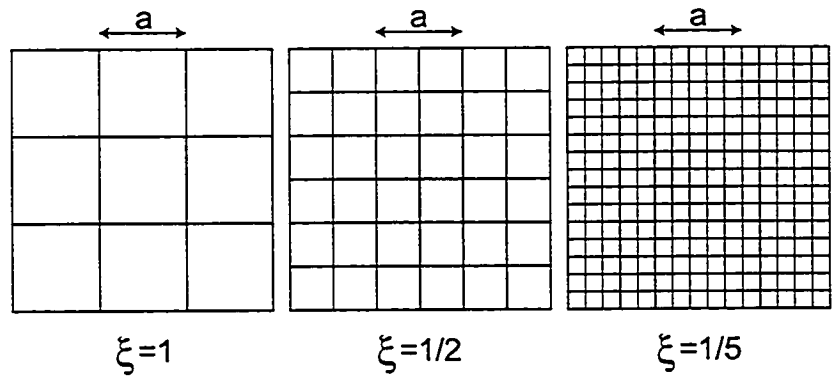

Figure 5.4: Variation of the lattice parameter ξa to study continuum limit ($\xi \to 0$) for a square obstacle and a surface concentration $C = 1/9$. The size of the analyte corresponds to one lattice site ($\xi a \times \xi a$).

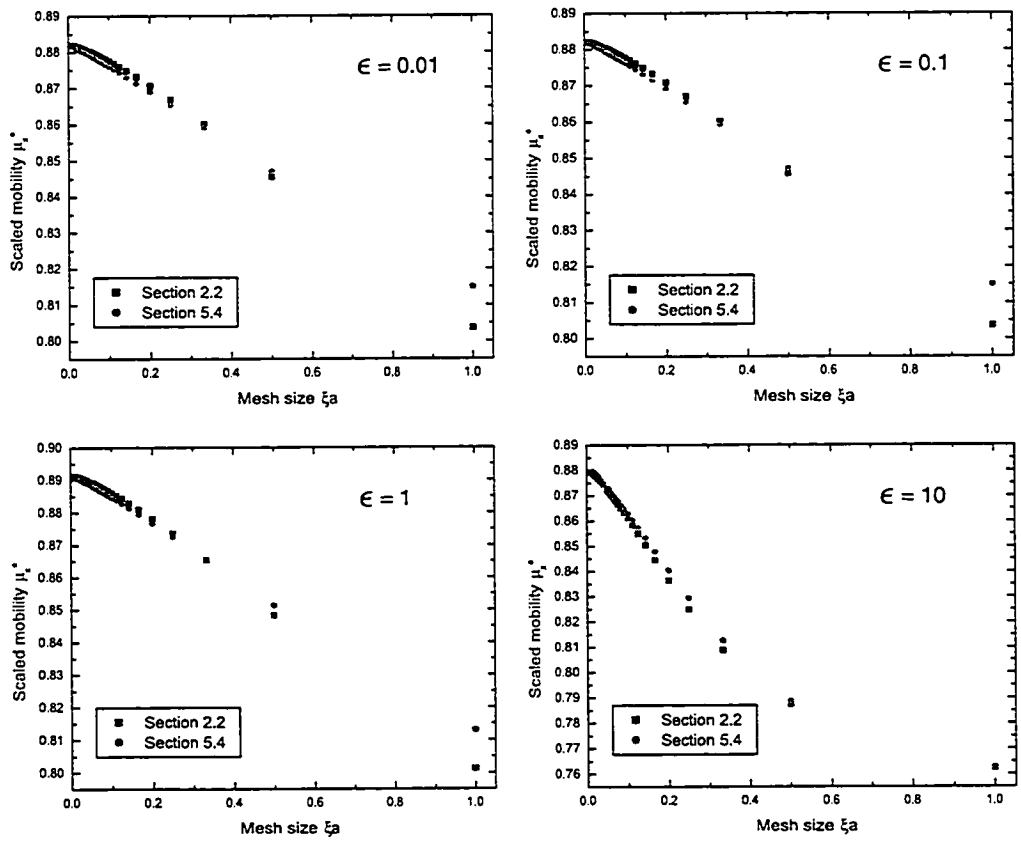

Figure 5.5: Scaled mobility μ_x^* vs the mesh size ξ for four different scaled fields ϵ. The calculations used the approaches presented in Sec. 2.2 and Sec. 5.4.

5.5 Discussion

In this chapter, we first demonstrated that the transition probabilities and the mean jump duration derived in chapter 2 cannot be used to study the diffusion of an analyte in the presence of an external field because they do not lead to the proper diffusion coefficient in free-solution. We explained that this failure of the model is due to the fact that we did not include the temporal fluctuations of the transition time $\langle \Delta\tau^2 \rangle$ in the description of the dynamics of the particle. We showed that, when both spatial and temporal fluctuations are explicitly used in the calculation of D_0, the correct (and constant) diffusion coefficient can be obtained (see Eq. 5.8). The fluctuations of the jump duration can be introduced via a stochastic time increment in a Monte Carlo simulation. This increment could be obtained from a normal distribution of mean τ and variance $\langle \Delta\tau^2 \rangle$ or simply from a dichotomous distribution given by $\tau \pm \sqrt{\langle \Delta\tau^2 \rangle}$.

However, it may be advantageous to have a constant time step (like when we want to write master equations similar to Eq. 2.21). Obviously, the absence of time fluctuations in our model is caused by the fact that a jump is made at each iteration (furthermore, all the jumps have the exact same time duration τ). We showed that a temporal fluctuation can be introduced in the model if we modify the transition probabilities in order to add a probability to stay on the same lattice site. This probability of not moving leads to a fluctuation of the time duration between two consecutive jumps. We showed how to obtain the value of this probability to stay put that gives the right time variance for one-dimensional systems and demonstrated that this solution is unique when we need to compute both the mobility and the diffusion coefficient.

In Sec. 5.3, we presented a mathematical generalization to higher dimensions. In short, this generalization consists in spreading the one-dimensional probability to stay put among the various probabilities for orthogonal motion (which is considered as a probability to stay put in the direction of the field). However, the resulting transition probabilities cannot be used in more than $2D$ because the probability to remain on the same lattice site is then negative.

We believe that this limitation is due to the fact that, in our first approach, jumps were only made in one direction at each time step. This does not quite respect what

we called the *simultaneity principle* for the jumps. Of course, the independence of the jumps in all directions is respected in our first approach, but we need to look at longer periods to observe multidirectional motion. This is why we presented a new way to define the transition probabilities where motion along all directions are allowed during each time step. This approach leads to a slightly more complicated analysis of the collisions with the obstacles but it has the advantage of giving the right mobility and diffusion coefficients in all directions, in any dimensions and for all values of the field ϵ. The new algorithm does not give the same mobility as our first approach due to the new way to deal with collisions, but we showed that the two methods are equivalent in the limit of the continuum. This does not constitute a problem since the objective of this calculation technique is to study realistic models, which means that we *must* work in this limit.

This problem with the simultaneity principle was encountered previously by Hong Guo [49] in his attempt to calculate the diffusion coefficient using Monte Carlo algorithms. His approach was to use the one-dimensional transition probabilities with a stochastic time step to simulate the dynamics in each direction. At each iteration, an axis was selected randomly and the motion along this direction was computed. However, in order to get the proper free-solution diffusion coefficient, he had to use different clocks for the different directions. When the jump was made along the x-axis, only the clock associated to this axis was incremented and only this clock was used in the calculation of the diffusion coefficient. This particular procedure, the use of *vectorial clocks*, was the only way to get the right diffusivities using the probabilities $p_{\pm}$. The new method that we presented in Sec. 5.4 represents a clear improvement over this algorithm because we eliminated the need for stochastic time increments and vectorial clocks.

As far as we know, our approach is the first that allows the calculation of the diffusion coefficient for any arbitrary field. As we already mentioned in previous chapters, most of the other methods used to study this kind of problems, like the repton model, use a time scale which is equal to ours only up to the first order in ϵ. These approaches are thus only valid for low fields ($\epsilon \ll 1$). Another example of this limitation is presented in the method proposed by Keller *et al.* [50] where they, like us, used a probability to stay put to study the diffusion coefficient. Without going into the details, let's just say that their approach assumed that $v_0/2 \ll D_0$, which corresponds to $\epsilon \ll 1$.

Chapter 6 Possible Extensions

In this last chapter, we would like to briefly describe two possible extensions of our model. These improvements have for objective to make our model even more versatile. We will present some ideas that can be used jointly with the approaches presented in chapters 2 and 5 to eliminate two limitations inherent to the current model:

1. The field lines have to be parallel to one of the cartesian axes. We cannot treat curved field lines and, consequently, insulating obstacles.

2. The system has to have an homogeneous viscosity. We cannot study systems with viscosity gradients or domains with different properties.

In the next sections, we will present detailed suggestions on how to tackle these particular situations.

6.1 Curved field lines

The problem of the curvature of the field lines is directly related to the nature of the obstacles. If the obstacles are perfect electrical conductors, the field lines are not affected by their presence and remain straight and parallel. It is thus possible to set one of the cartesian axes parallel to these field lines and use our calculation technique. However, if the obstacles are partially or completely insulating, the field lines are no longer straight and parallel and they must go around the obstacles.

The projection approach

The model presented in this thesis constitutes a generalization of a previous model that was only valid for vanishing fields [5]. In this latter model, the question of the curvature of the field lines was not a major problem since all calculations were performed in the limit

where $\epsilon \to 0$. In fact, it was demonstrated in Ref. [12] that in this limit, conducting and insulating obstacles lead to the very same mobility coefficients.

We can now ask ourselves whether our generalized approach presented in chapter 2 can be directly used with projections of the curved field lines along the cartesian axes. Let's examine a two-dimensional system in which the local field is not parallel to the x-axis. Locally, $\overrightarrow{\epsilon}$ makes a angle θ_ϵ with this axis. We also define two new orthogonal axes, x' and y', tilted by an angle θ_ϵ such that the x'-axis is parallel to the local field line. The transition probabilities along the x and y axes (i.e. along the grid) would now be given by (using Eq. 2.3):

$$p_{\pm x} = \frac{1}{1 + e^{\mp 2\epsilon \cos\theta_\epsilon}} , \tag{6.1}$$

$$p_{\pm y} = \frac{1}{1 + e^{\mp 2\epsilon \sin\theta_\epsilon}} , \tag{6.2}$$

and the corresponding transition times would be given by (using Eq. 2.1):

$$\tau_x = \frac{\tanh(\epsilon \cos\theta_\epsilon)}{\epsilon \cos\theta_\epsilon} \tau_B . \tag{6.3}$$

$$\tau_y = \frac{\tanh(\epsilon \sin\theta_\epsilon)}{\epsilon \sin\theta_\epsilon} \tau_B . \tag{6.4}$$

If we carry out the calculation that we derived in Sec. 2.2, we now obtain these new two-dimensional transition times and probabilities:

$$T \equiv \frac{\tau_x \tau_y}{\tau_x + \tau_y} . \tag{6.5}$$

$$P_{\pm x} = \frac{1}{(1 + e^{\mp 2\epsilon \cos\theta_\epsilon})(1 + \tau_x/\tau_y)} , \tag{6.6}$$

$$P_{\pm y} = \frac{1}{(1 + e^{\mp 2\epsilon \sin\theta_\epsilon})(1 + \tau_y/\tau_x)} . \tag{6.7}$$

These equations are equivalent to Eqs. 2.10–2.12 when $\theta_\epsilon = 0$. We can calculate the free-solution velocity along the field axis (the x'-axis) and verify that it is still given by Eq. 2.4:

$$v_{0_{x'}} = \frac{\langle x' \rangle}{T} = \frac{a}{T}\left((P_{+x} - P_{-x})\cos\theta_\epsilon + (P_{+y} - P_{-y})\sin\theta_\epsilon\right) = \frac{\epsilon a}{\tau_B} . \tag{6.8}$$

However, the lateral (perpendicular to the field) free-solution diffusion coefficient along the y'-axis is no longer given by $a^2/2\tau_B$:

$$\begin{aligned} D_{0_{y'}} &= \frac{\langle y'^2\rangle - \langle y'\rangle^2}{2T} \\ &= \frac{a^2}{2T}\left((P_{+y}+P_{-y})\cos\theta_\epsilon + (P_{-x}+P_{+x})\sin\theta_\epsilon\right) \\ &\quad -\frac{a^2}{2T}\left((P_{+y}-P_{-y})\cos\theta_\epsilon + (P_{-x}-P_{+x})\sin\theta_\epsilon\right)^2 \neq \frac{a^2}{2\tau_B}. \end{aligned} \tag{6.9}$$

The exact result is too large to be presented here, but we show an example of this result in the bottom part of Fig. 6.1. One can argue that the field-dependence of $D_{0_{y'}}$ is not really a problem since it was also the case for the diffusion coefficient D_{0_x} in our model in chapter 2 (see Eq. 5.18 or the first graph of Fig. 6.1). Indeed, our previous model gave the proper free-solution values for v_{0_x}, v_{0_y} and D_{0_y} but not for D_{0_x} when we use non-vanishing fields. For instance, the first graph of Fig 6.1 shows that D_{0_x} was finite for all values of the field ϵ and, since we were only interested in the calculation of the mobility coefficient, the spurious field-dependence of D_{0_x} did not affect our calculations (the diffusion coefficient merely describe the spreading of the particles around their average position). Moreover, we did verify that the changes to the transition time and the probabilities of transition that follow the addition of a probability to stay put (which changes the diffusion coefficient D_{0_x}) do not affect the calculation of the mobility, even in the presence of obstacles.

On the other hand, the derivation presented here does not give the right free-solution diffusion in both the x' and y' directions when the field is not parallel to one of the axes ($\theta_\epsilon \neq n\pi/2$, where n is an integer). In fact, the free-solution diffusion coefficients $D_{0_{x'}}$ and $D_{0_{y'}}$ diverge linearly with ϵ when $\epsilon \to \infty$ (see the bottom part of Fig. 6.1). It is thus impossible to use Eqs. 6.5 to 6.7 even for the calculation of the mobility because the error on the average position of the particles tends to infinity as the field increases. Another argument is that the lateral diffusion is directly related to the time needed to move around an obstacle. If this coefficient diverges at high field, we will not be able to observe the reduction of the mobility due to successive collisions between the analyte and an obstacle.

The increase of $D_{0_{y'}}$ can be understood in a simple way. The field does not bias the motion in the y'-direction, but all the jumps now take a shorter period of time. Therefore, the presence of the field speeds up the diffusion process in the y' (and x') direction, a simple

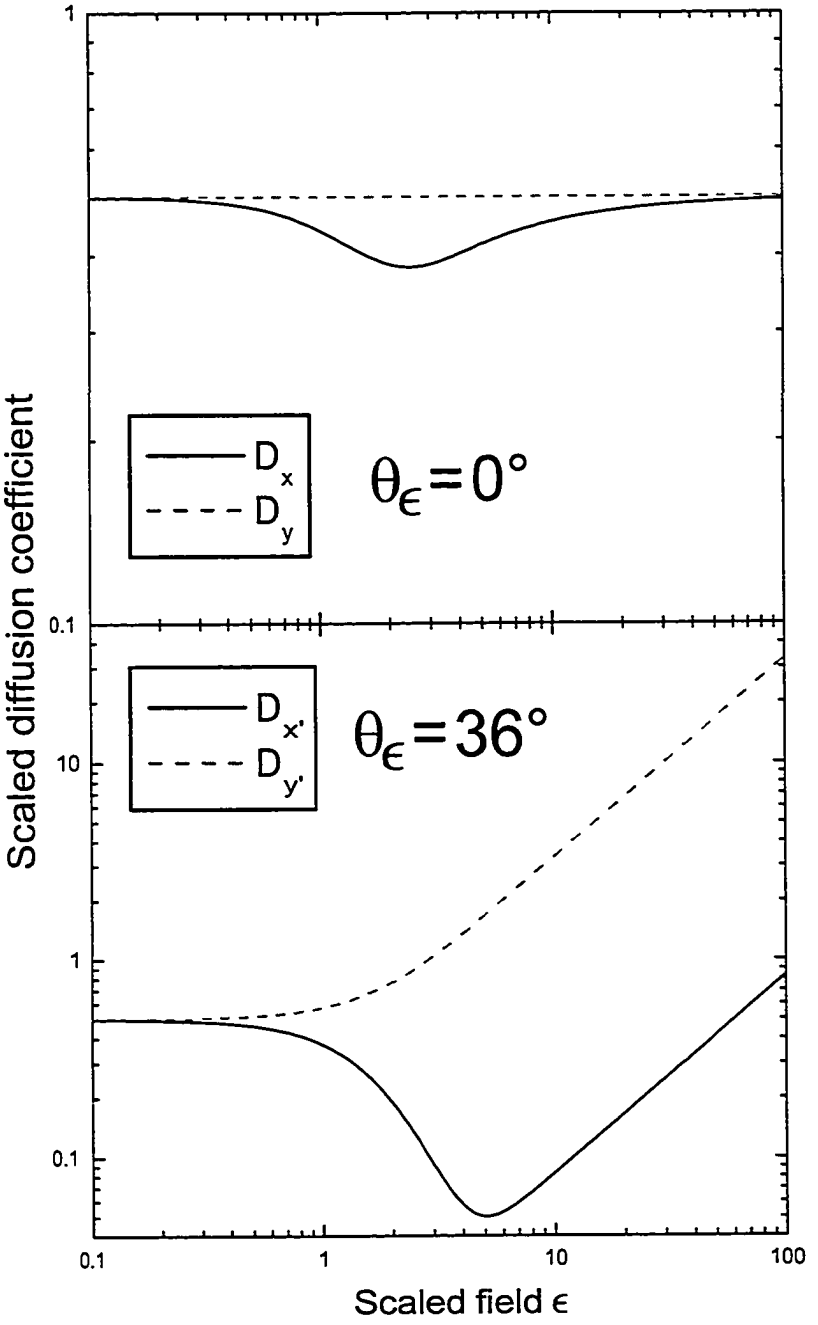

Figure 6.1: The free-solution scaled diffusion coefficients vs the scaled field ϵ for two different values of θ_ϵ. The first graph was obtained with $\theta_\epsilon = 0$ and corresponds to the model presented in chapter 2. We can see that only D_{0_y} gives the right (constant) value of 1/2, while D_{0_x} gives incorrect but finite values for all field intensities (except when $\epsilon = 0$). The second graph shows the same two curves for $\theta_\epsilon = \pi/5$ (obtained from Eqs. 6.5 to 6.7). We observe that these two curves give incorrect values, even when $\epsilon = 0$, and that they diverge when $\epsilon \to \infty$.

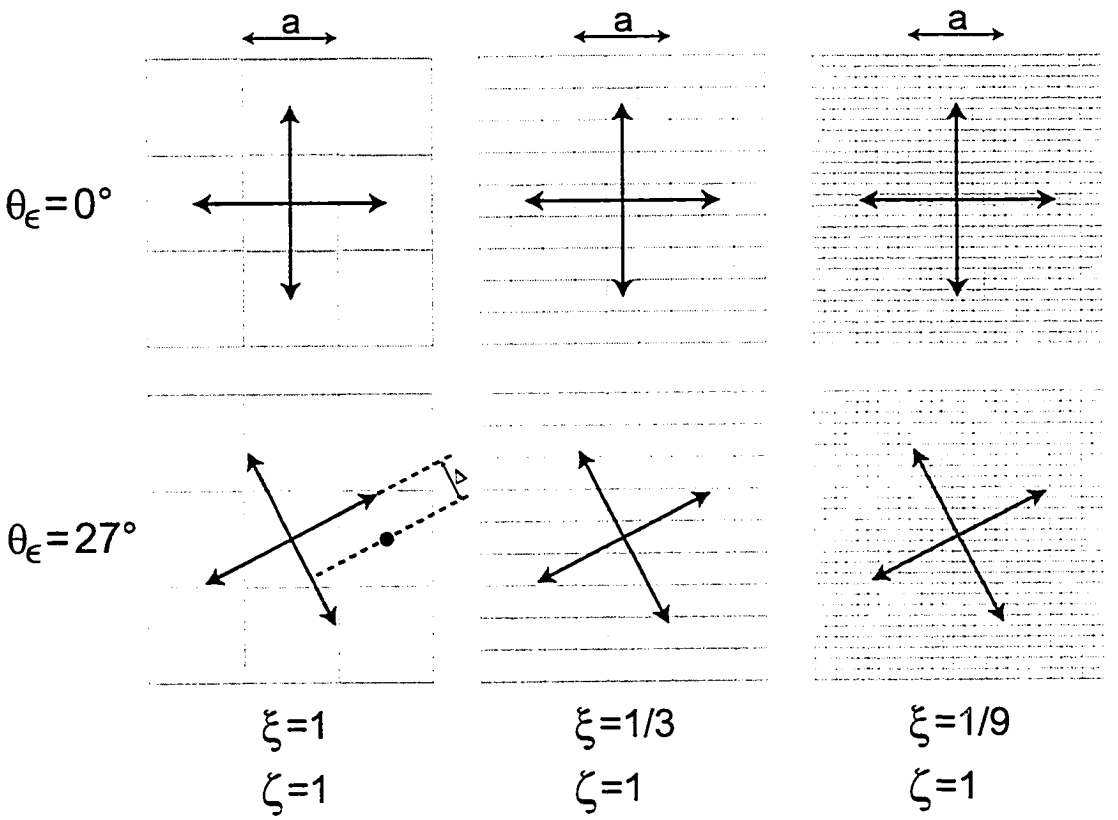

Figure 6.2: Illustration of the resulting displacements for two different orientations of the allowed jumps ($\theta_\epsilon = 0$ and $3\pi/20$) for three different values of the lattice parameter ($\xi a = a$, $a/3$ and $a/9$). The length of the jump ζa is not reduced as we decrease the lattice parameter. We see that, in the continuum limit ($\xi \to 0$), the final positions (shaded squares) of the particle tend to be along the axis of the field θ_ϵ. In other words, the offset $\Delta \to 0$ as $\xi \to 0$.

artefact of the use of misaligned cartesian axes. In fact, both diffusion coefficients increase linearly with the field intensity ϵ when $\epsilon \gg 1$ because $T \sim 1/\epsilon$ in this limit. Obviously, this will also be the case if we use the same approach with the set of probabilities developed in Sec. 5.4 instead.

Locally inclined set of probabilities

We demonstrated in the previous section that, when the field orientation is not parallel to the grid, we cannot use a projection on the cartesian axes in any of our approaches (Secs. 2.2 or 5.4) due to the fact that the diffusion coefficients then diverge.

We thus suggest a new algorithm where the jumps are not along the cartesian axes anymore. By that we mean that we tilt our orthogonal set of probabilities in order for the $P_{\pm}$ transitions to remain parallel to the direction of the field even though the orientation of the grid is left unchanged. Obviously, this approach will only be valid in the continuum limit ($\xi \to 0$), as we show in Fig. 6.2. This figure compares the resulting displacements for two different orientations of the set of probabilities ($\theta_\epsilon = 0$ and $3\pi/20$) for three different values of the lattice parameter ($\xi a = a$, $a/3$ and $a/9$). Notice that, contrary to what we did in Sec. 5.4, we reduce the lattice parameter without reducing the length of a jump (which is given by $\zeta a = a$ for the three examples). This figure illustrates that, when the field is inclined ($\theta_\epsilon \neq 0$) and the lattice parameter is large ($\xi \to 1$), the final position of the particle after a jump cannot be exactly along the field axis because the lattice is too coarse. This offset (Δ) will lead to incorrect mobility and diffusion coefficients but this error will decrease to zero as the size of the lattice parameter ξa is reduced. It is also important to mention that the analyte has to be a point-like particle. If this is not the case and the field is curved, there will be a net torque applied on the particle and our model is then incorrect. This approach can be used with more complicated sets of probabilities, like the one developed for diffusion in Sec. 5.4, as long as we reach the continuum limit ($\xi \to 0$).

Finally, realistic obstacle shapes can still be studied with this method. The idea is to study the *two continuum limits* of ξ and ζ, i.e. we have to reduce both the lattice parameter and length of a jump to obtain realistic systems. First, to observe physically correct effects related to the obstacle shape, we need a very small jump length ($\zeta \ll 1$). In addition to this first condition, in order to get the right displacement in the presence of an inclined field, we need a lattice parameter that is much smaller than the length of a jump ($\xi \ll \zeta$). So the continuum limit for curved field lines and realistic obstacle shapes is reached when:

$$\xi \ll \zeta \ll 1 . \tag{6.10}$$

An example for $\xi = 1/15$ and $\zeta = 9/15$ is illustrated in Fig. 6.3.

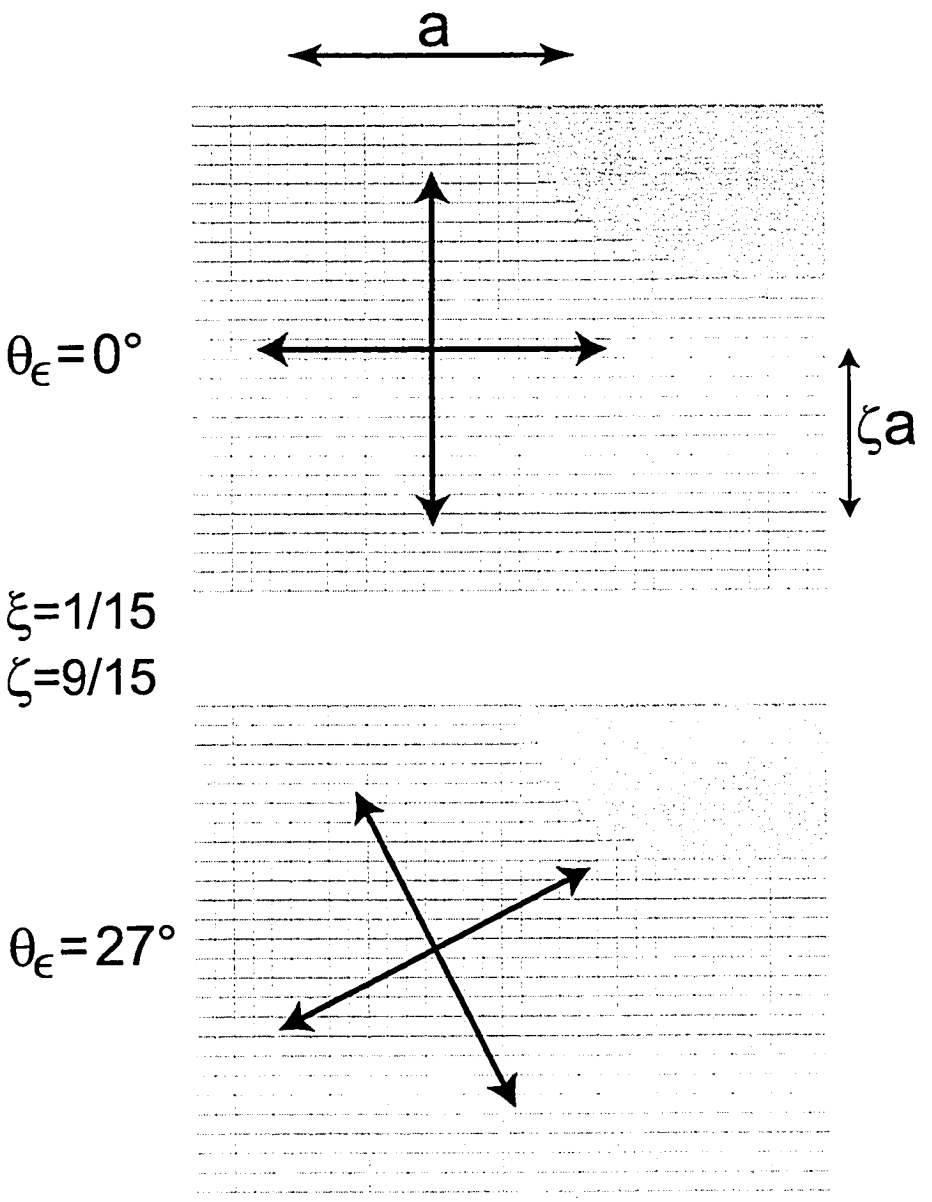

Figure 6.3: Lattice representation of the two continuum limits ($\xi \ll \zeta \ll 1$) with locally curved field lines where both the lattice parameter ξa and the length of a jump ζa are reduced. In the upper right corner, we can partially see a spherical obstacle of radius $R = a$.

6.2 Viscosity gradients

The second problem treated in this chapter is the case where there is a viscosity gradient or a domain structure (see Fig. 6.4). Our model is based on the assumption of an homogeneous environment where, in the absence of obstacles, the velocity and the diffusion coefficient are constant ($\epsilon a/\tau_B$ and $a^2/2\tau_B$, respectively). In this section, we would like to show how we can deal with a medium where these quantities are no longer uniform.

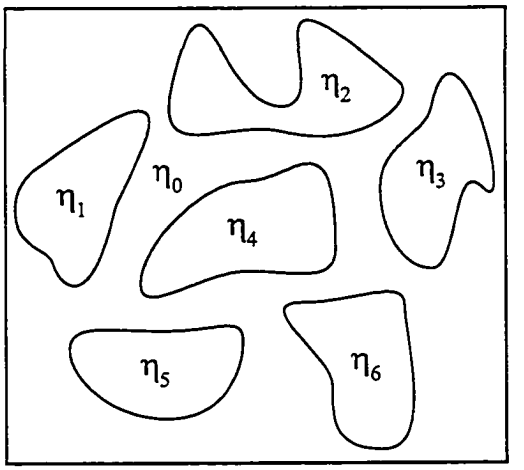

Figure 6.4: Example of a domain structure. The different zones have different viscosity properties.

Simulation algorithms

It is easy to include the effect of the viscosity of the medium in our transition times and probabilities in order to perform Monte Carlo simulations. The idea is to determine a reference viscosity η_0 and the relation between the Brownian time τ_B and the viscosity η. Since the diffusion coefficient is inversely proportional to the viscosity (see Eq. 1.9) as well as inversely proportional to the Brownian time (see Sec. 2.1), we have $\tau_B \sim \eta$. So, when the viscosity η_0 is changed by a factor γ, the Brownian time τ_{B_0} is also changed by the same multiplicative factor:

$$\text{if} \quad \eta = \gamma\eta_0 , \qquad \text{then} \quad \tau_B = \gamma\tau_{B_0} , \tag{6.11}$$

where τ_{B_0} is the Brownian time corresponding to the reference viscosity η_0. It is thus possible to carry out Monte Carlo simulations where the local dynamics of the particle is always described in terms of the local viscosity. In principle, this approach can be used with the sets of probabilities developed in chapters 2 (if we are interested in the calculation of the mobility only) or 5 (if we want both mobility and diffusion coefficients).

Exact mobility calculations

However, if we want to obtain exact mobilities using the method described in chapters 2 to 4, we cannot have an inhomogeneous transition time. Since our exact calculation method is only valid for the calculation of the mobility, we can use the probability to stay put to model the effect of the viscosity gradient instead of the diffusion coefficient. We know that the velocity of a particle is inversely proportional to the viscosity (see Eq. 1.11) but proportional to the transition probabilities. Then, if the viscosity η_0 is changed by a factor γ, the transition probabilities $P_\pm$ and $P_\perp$ are changed by the inverse of this multiplicative factor:

$$\text{if} \quad \eta = \gamma\eta_0 , \qquad \text{then} \quad \begin{cases} P'_\pm = \frac{1}{\gamma} P_\pm \\ P'_\perp = \frac{1}{\gamma} P_\perp \end{cases} , \tag{6.12}$$

and the normalization condition imposes that:

$$S' = 1 - \frac{1}{\gamma} . \tag{6.13}$$

This last equation shows that we have to choose our arbitrary reference viscosity η_0 in order to have $\gamma \geq 1$ everywhere if we are to get properly bounded probabilities. This could be done by setting η_0 equal to the lowest viscosity of the media (the fastest region). Notice that the diffusion coefficient along the field is still incorrect (S' does not have the right value), but, since the time step is now the same everywhere, we can write master equations and calculate the exact mobility as we did in chapter 2 (see Eq. 2.21) using a constant time step T (unaffected by the value of the local viscosity, but still function of ϵ).

Detailed balance

For models that simulate spatial variations of the viscosity, a fundamental constraint that has to be satisfied is the *detailed balance* between two neighboring cells:

When the system has reached the thermodynamic equilibrium (i.e., at $\epsilon = 0$), the net flux of particles Φ between any two adjacent cells should be zero.

We can verify that the two methods presented above respect this condition by calculating the net transfer rate of particles at the boundary between any two cells. An example of this calculation for one iteration (one time step T) is illustrated below:

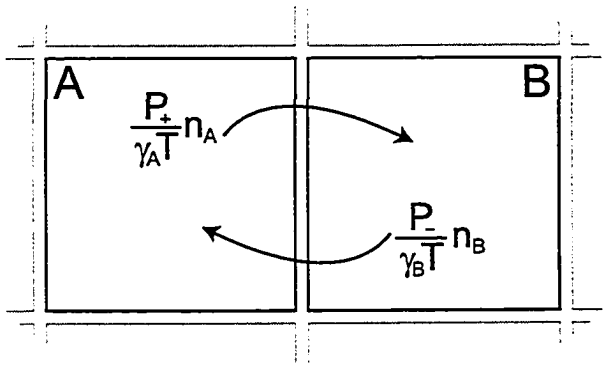

Here, the transition rates are given by $P_\pm/\gamma_{A,B}T$ and the probability of presence in the cells by $n_{A,B}$. The net flux through the interface is then:

$$\Phi = \frac{P_+}{\gamma_A T} n_A - \frac{P_-}{\gamma_B T} n_B = 0\,. \tag{6.14}$$

But when $\epsilon = 0$ (the thermodynamic equilibrium), the probabilities P_+ and P_- are equal and we obtain:

$$\frac{n_A}{n_B} = \frac{\gamma_A}{\gamma_B}\,, \tag{6.15}$$

as expected because the probability of presence in a cell is then necessarily proportional to the viscosity in this cell. In other words, the particle spends more time in a cell if the local viscosity is higher. Note that we assumed that $P_+ = P_-$ across the interface when $\epsilon = 0$. In other words, we did not model the effect of the interface on the jumping probabilities in this simple model.

Permeable membranes and interfacial effects

Finally, it is also possible to model the physics of permeable membranes (or interfacial effects) dividing domains with different viscosities simply by using an (additional) probability to accept a jump when this jump means trying to move through the membrane. If the

attempted jump is rejected, the particle remains on the same site as if the neighbor were an obstacle. If this kind of membrane is inserted between cells A and B of our previous example, the detailed balance is now illustrated by the following diagram:

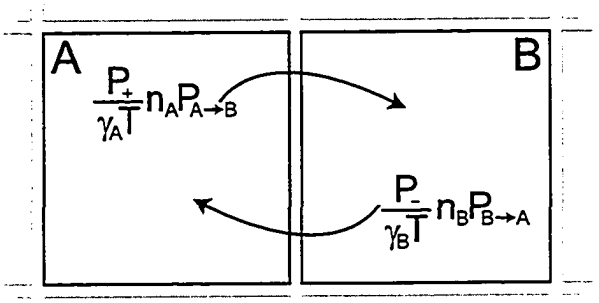

where P_{A-B} and P_{B-A} are the directional probabilities to accept the jumps across the membrane during the current iteration. In this case, Eq. 6.15 becomes:

$$\frac{n_A}{n_B} = \frac{\gamma_A P_{B-A}}{\gamma_B P_{A-B}}. \tag{6.16}$$

We notice that detailed balance is respected if $P_{A-B} = P_{B-A}$. Otherwise, the membrane is active and the ratio P_{A-B}/P_{B-A}, together with the viscosities, affects the probabilities of presence at thermodynamic equilibrium.

As expected, Eq. 6.16 shows that the probability of presence in a cell of type A is inversely proportional to the probability to jump across the membrane from A to B, and vice versa. In other words, the probability to be in a particular cell is inversely proportional to the probability to exit from this cell. In the extreme case where one of these probabilities is equal to zero, all the particles will be in the same domain (the one from which it is impossible to escape) at the thermodynamic equilibrium.

Theoretical models for the study of spatial viscosity domains could be useful to interpret and analyze many experimental observations made on lipid systems (see Refs. [51, 52] for examples). We believe that this is very promising.

Chapter 7 Conclusions

This thesis presents a new lattice model of a highly biased random walk. Our main motivation was the calculation of the mobility and diffusion coefficients of small particles in the presence of a sieving media or an array of obstacles, either through exact calculation techniques or Monte Carlo algorithms.

The starting point of our model is the anisotropy of the time duration of the jumps in presence of an external bias. We demonstrated that our approach is equivalent to the discretization of the continuous dynamics of a Brownian walker. Our new model allows us to compute the exact (analytical or numerical) mobility coefficient in any dimensions and for any value of the external field. This last point constitutes the most significant advance because all the current models are fundamentally limited to low field values. Our model is thus the first one that allows us to study the impact of the electric field on the mobilities in the presence of obstacles.

The possibility of calculating exact analytical mobilities using software packages like Maple is a useful *diagnostic* tool, even if it is restricted to small systems. These exact functions give us the opportunity to compute asymptotic series as a function of the external field ($\epsilon \to 0$ or $\epsilon \to \infty$) and to detect the exact positions of maxima or minima, which is extremely useful. We can also design simpler versions of complex systems and use exact results for optimization purposes.

Our new model was used to investigate generic two-dimensional electrophoresis gel systems and to extend the previous results obtained for vanishing fields to arbitrary values of the external bias. Periodic distributions of obstacles have been widely studied in the limit of zero-field ($\epsilon \to 0$) [5, 6, 8, 11, 25]. These studies showed that, when the field tends towards zero, the the mobility μ can be expressed as a polynomial function of the concentration of obstacles, C. We extended these results to high field intensities and we observed a surprising qualitative change in the nature of the power series for $\mu(C)$ as the field is

increased (the series changes from integer power of C to half-integer powers of C).

We also investigated the effect of trapping regions in the presence of high external fields using random distributions of obstacles. Such distributions have also been studied in the zero-field limit [5, 11] and the effect of the trapping regions on the mobility was found to be related solely to the percolating properties of the medium. However, at high field, the presence of traps should induce an exponential decrease of the mobility. We demonstrated this effect using the exact analytical mobilities obtained for small periodic *trap* systems and showed that the exponential factor increases with the trap depth. We also showed that this exponential decay is a characteristic of random distributions by comparing pure random systems with random maze distributions. The latter were specially designed to be free of such trapping regions. In these mazes, we did not observe any exponential decay, contrary to pure random systems. The effect of the traps was observed with the increase with both the field intensity and the obstacle concentration.

Our model can be used to compare the electrophoretic velocity of particles with different electric charges and/or physical sizes. We investigated specific two-dimensional distributions of obstacles that can be used to separate particles, e.g. in a microfluidic device. More precisely, we compared the velocity of differently charged or sized analytes in sieving, trapping and deflecting systems to model various electrophoretic separation techniques. In particular, we studied the nonlinear effects present in ratchet systems and how they can be combined with time-asymmetric pulsed fields to provide new modes of separation. We demonstrated that our model can be a useful tool to develop, optimize or understand new separation devices. The utility of our approach was illustrated by our study of the deflecting system designed by Austin and co-workers [40, 41, 42, 43]. Even with a rough approximation of this system, we were able to predict the finite deflection angle observed in the zero-field limit, a feature that was not explained by their own theoretical model.

In this thesis, we also studied the problems related to the calculation of the diffusion coefficients using lattice random walks. In chapter 5, we presented a more general model that can be used to compute exact free-solution diffusion coefficients. We focused our attention on the importance of taking into account the fluctuations of the jumping time to obtain the proper diffusivity, and how this could be done by adding a probability to remain on the same lattice site. We showed how to extend these concepts from $1D$ to any other

dimension. We mentioned the challenges that we encountered when we tried to introduce the effect of obstacles on the diffusion of the particles. In spite of these efforts, we still do not know how to calculate exactly the diffusion coefficient. The models proposed in this thesis can only be used with Monte Carlo algorithms if we are interested in both mobility and diffusion coefficients. This still constitutes a huge development since, to the best of our knowledge, this is the first time that such a general approach, valid for any value of the field, is proposed. This model could also be of great interest in the development of separation technologies since the diffusion coefficient is directly related to the resolution of such devices.

It is important to emphasize the fact that if we want to study real systems, we need to reach the continuum limit. In this limit, we can obtain the mobility and/or diffusion coefficient of point-like particles in distributions of obstacles with realistic shapes. It is also possible to study finite size spherical objets by increasing the dimensions of the obstacles by the radius of the particle. Reaching the continuum limit increases the computational costs of the calculations but, with the increasing availability of supercomputers and parallel programming resources, we believe that our approaches constitute promising directions for further studies.

With minimum modifications, our model can be used to investigate many different problems. First, in all the cases presented in this thesis, we used hard-core repulsive interactions to represent the effect of the obstacles on the analyte, but, as it was demonstrated for the zero-field limit in Ref. [9], many other forms of gel-analyte interactions, like attractive binding, could be studied. We could also use our calculation technique to study the effect of the concentration of particles on their average mobility. However, the computational requirements for such calculations increase extremely rapidly with the size of the system. Another possibility that we did not mention in this thesis is the study of the mobility of polymers (two or more analytes linked to each other). A description of this kind of study is presented in Ref. [10] for vanishing fields, and it is straightforward to adapt it to our high field algorithms.

Finally, we proposed two possible extensions to our model that could allow us to treat even more realistic situations. The first one is the addition of curve field lines, which is necessary to study the impact of the conductivity of the obstacles. This is an important

point because it was demonstrated [43] that similar shaped obstacles, but with different conducting properties, could lead to very different sieving phenomena. This nuance could be a crucial point in separation technologies. The second improvement that we proposed is the study of spatial viscosity domains. We showed that it is easy to consider the impact of a non-homogeneous fluid by changing locally the Brownian time or the transition probabilities. Again, such systems could be studied using either exact calculations or Monte Carlo simulations, depending if we are interested in the mobility only or in both mobility and diffusion coefficients. This improvement opens the door to a lot of new projects like the study of membranes between different media or the use of viscosity gradients as a separation tool.

Appendix A Maple Code

The following lines give the Maple code used to obtain Eqs. 2.30 and 2.31.

```
> with(linalg) :
> with(plots) :
> A := array(1..5, 1..5, [[−1 + q, q, 0, 2 ∗ r, 0], [p, −1 + p, 0, 0, 2 ∗ r],
  [0, 0, −1 + 2 ∗ r, q, p], [2 ∗ r, 0, p, −1, q], [1, 1, 1, 1, 1]]);
> b := vector([0, 0, 0, 0, 1]);
> vx := vector([p ∗ a/T, −q ∗ a/T, (p − q) ∗ a/T, (p − q) ∗ a/T, (p − q) ∗ a/T]):
> vy := vector([0 ∗ a/T, 0 ∗ a/T, 0 ∗ a/T, 0 ∗ a/T, 0 ∗ a/T]);
> n := linsolve(A, b) :
> vx_avg := simplify(evalm(n& ∗ vx)) :
> simplify(subs(p = 1/((1 + exp(−2 ∗ epsilon)) ∗ (1 + tau/tauB)),
  q = 1/((1 + exp(2 ∗ epsilon)) ∗ (1 + tau/tauB)), r = 1/(2 ∗ (1 + tauB/tau)),
  T = tau ∗ tauB/(tau + tauB), tau = tauB ∗ tanh(epsilon)/epsilon,
  (vx_avg/epsilon)/(a/tauB))):
> vy_avg := simplify(evalm(n& ∗ vy)) :
> simplify(subs(p = 1/((1 + exp(−2 ∗ epsilon)) ∗ (1 + tau/tauB)),
  q = 1/((1 + exp(2 ∗ epsilon)) ∗ (1 + tau/tauB)), r = 1/(2 ∗ (1 + tauB/tau)),
  T = tau ∗ tauB/(tau + tauB), tau = tauB ∗ tanh(epsilon)/epsilon,
  (vy_avg/epsilon)/(a/tauB)));
```

Appendix B Negative orthogonal probabilities for $d > 2$

In Sec. 5.3, we demonstrated that the model described in chapter 2 cannot be adapted to work in more than two dimensions if we are interested in both velocities and diffusion coefficients. In this appendix, we will give a general proof of this fundamental restriction:

> *Even with a probability to stay put, it is impossible to derive a set of biased orthogonal transition probabilities and the corresponding transition time that give the right velocities and diffusion coefficients for all values of the external field when $d > 2$.*

By orthogonal transition probabilities, we mean that the field is applied along one of the cartesian axes and that all other directions are perpendicular to the field. Also, the jumps are made in only one direction at each time step.

Let us try to find the functions $P_{\pm}(\epsilon)$, $P_{\perp}(\epsilon)$, $S(\epsilon)$ and $T(\epsilon)$ that would satisfy the equations for the free-solution velocity and diffusion coefficients in d dimensions. We assume that we don't have any prior knowledge of the form of these expressions. We thus have five variables:

$$[P_{+}(\epsilon)\,,\, P_{-}(\epsilon)\,,\, P_{\perp}(\epsilon)\,,\, S(\epsilon)\,,\, T(\epsilon)]\,, \tag{B.1}$$

and five equations to satisfy (dimensionless):

1. The normalization condition:

$$P_{+}(\epsilon) + P_{-}(\epsilon) + 2(d-1)P_{\perp}(\epsilon) + S(\epsilon) = 1\,. \tag{B.2}$$

2. The free-solution diffusion coefficient along the field:

$$D_{0_x}(\epsilon) = \frac{P_{+}(\epsilon) + P_{-}(\epsilon) - (P_{+}(\epsilon) - P_{-}(\epsilon))^2}{2T(\epsilon)} = \frac{1}{2}\,. \tag{B.3}$$

3. The free-solution velocity along the field:

$$v_{0_x}(\epsilon) = \frac{P_+(\epsilon) - P_-(\epsilon)}{T(\epsilon)} = \epsilon\,. \tag{B.4}$$

4. The free-solution diffusion coefficient orthogonal to the field:

$$D_{0_\perp}(\epsilon) = \frac{P_\perp(\epsilon) + P_\perp(\epsilon) - (P_\perp(\epsilon) - P_\perp(\epsilon))^2}{2T(\epsilon)} = \frac{P_\perp(\epsilon) + P_\perp(\epsilon)}{2T(\epsilon)} = \frac{1}{2}\,. \tag{B.5}$$

5. The free-solution velocity orthogonal to the field:

$$v_{0_\perp}(\epsilon) = \frac{P_\perp(\epsilon) - P_\perp(\epsilon)}{T(\epsilon)} = 0\,. \tag{B.6}$$

The field direction is chosen to be x. However, the last equation is always satisfied. We thus have 5 variables and only 4 equations. So we can find an infinity of solutions for Eqs. B.2 to B.5. Without going into the details, the solutions for $P_\pm(\epsilon)$, $P_\perp(\epsilon)$ and $T(\epsilon)$ as a function of $S(\epsilon)$ are:

$$P_\pm(\epsilon) = \frac{2\epsilon^2\,(1 - S(\epsilon)) + (d - 1 \mp \epsilon)\left(d - \sqrt{d^2 + 4\epsilon^2\,(1 - S(\epsilon))}\right)}{4\epsilon^2}\,. \tag{B.7}$$

$$P_\perp(\epsilon) = \frac{-d + \sqrt{d^2 + 4\epsilon^2\,(1 - S(\epsilon))}}{4\epsilon^2}\,. \tag{B.8}$$

$$T(\epsilon) = \frac{-d + \sqrt{d^2 + 4\epsilon^2\,(1 - S(\epsilon))}}{2\epsilon^2}\,. \tag{B.9}$$

It is easy to verify that:

$$\text{if} \quad \begin{cases} d \geq 1 \\ \text{and} \\ 0 < S(\epsilon) < 1 \end{cases}, \quad \text{then} \quad 0 < \begin{matrix} P_+(\epsilon) \\ P_\perp(\epsilon) \\ T(\epsilon) \end{matrix} < 1\,. \tag{B.10}$$

However, when $d > 2$, it is impossible to find a function $S(\epsilon)$ bounded between 0 and 1 that gives a positive probability to move backward ($P_-(\epsilon)$) for all values of ϵ. Figure B.1 shows how the probability $P_-(\epsilon)$ (Eq. B.7) varies with the probability to stay put $S(\epsilon)$ for

different values of the dimension d and the external field ϵ. In the first graph of this figure (d=2), we can always find a region where $P_{-}(\epsilon)$ and $S(\epsilon)$ are both bounded between 0 and 1 whatever the value of the field (we present only three curves for reasons of clarity). The second graph shows that, when $d = 3$, there is a critical value of the field ($\epsilon_c = 2$) above which there is no positive solution for $P_{-}(\epsilon)$ in the range $0 \leq S(\epsilon) < 1$. For higher dimensions, the value of ϵ_c decreases as d increases. In fact, one can use Eq. B.7 to show that the value of the critical field ϵ_c, as a function of the dimension d, is given by:

$$\epsilon_c = \frac{d-1}{d-2} = 1 + \frac{1}{d-2}, \tag{B.11}$$

for $d \geq 2$. So, even with the probability to stay put as a free parameter, it is impossible to find a generalized set of probabilities and a transition time that are valid for all values of the field for $d > 2$ when the jumps are attempted in only one direction at each step. However, Eq. B.11 tells us that this approach will be at least valid for fields ϵ up to one, whatever the dimension d.

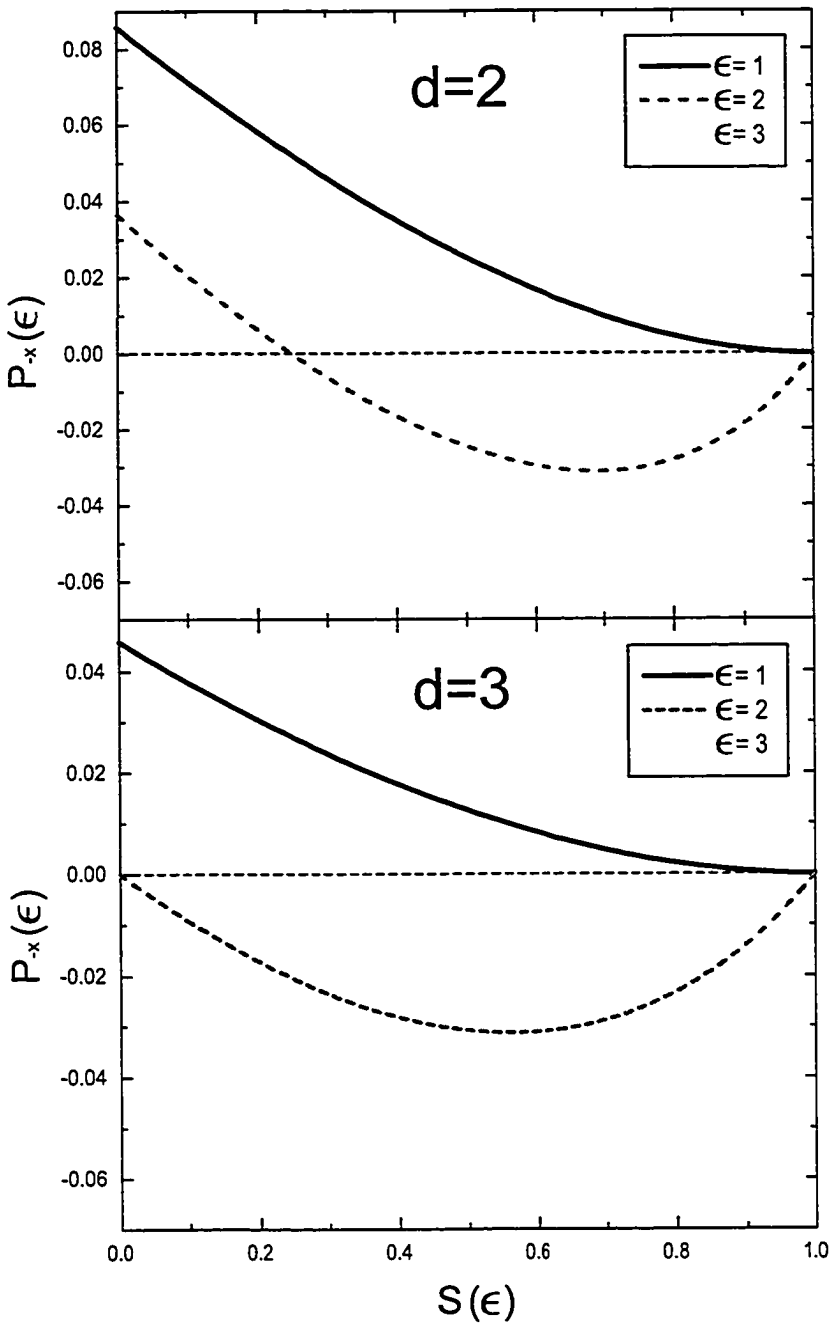

Figure B.1: Probability $P_{-}(\epsilon)$ (Eq. B.7) vs the probability to stay put, $S(\epsilon)$, for different values of the dimension d and the external field ϵ.

Bibliography

[1] Pathria, R. H. *Statistical Mechanics, Second Edition.* Butterworth-Heinemann, (1996).

[2] Reif, F. *Fundamentals of statistical and thermal physics.* McGraw-Hill, (1965).

[3] Viovy, J.-L. "Electrophoresis of dna and other polyelectrolytes: Physical mechanisms". *Review of Modern Physics* **72**, 813–872 (2000).

[4] Chicurel, M. "Faster, better, cheaper genotyping". *Nature* **412**, 580–582 (2001).

[5] Slater, G. W. and Guo, H. L. "An exacly solvable ogston model of gel electrophoresis: I. the role of the symmetry and randomness of the gel structure". *Electrophoresis* **17**, 977–988 (1996).

[6] Slater, G. W. and Guo, H. L. "An exacly solvable ogston model of gel electrophoresis: II. sieving through periodic gels". *Electrophoresis* **17**, 1407–1415 (1996).

[7] Slater, G. W. and Treurniet, J. R. "An exacly solvable ogston model of gel electrophoresis: III. percolation and sieving through two-dimensional gels". *Journal of Chromatography A* **772**, 39–48 (1997).

[8] Mercier, J.-F. and Slater, G. W. "An exactly solvable ogston model of gel electrophoresis IV: Sieving through periodic three-dimensional gels". *Electrophoresis* **19**, 1560–1565 (1998).

[9] Labrie, J., Mercier, J.-F., and Slater, G. W. "An exacly solvable ogston model of gel electrophoresis: V. attractive gel-analyte interactions and their effect on the ferguson plot". *Electrophoresis* **21**, 823–833 (2000).

[10] Boileau, J. and Slater, G. W. "An exacly solvable ogston model of gel electrophoresis: VI. towards a theory for flexible mocromolecules". *Electrophoresis* **22**, 673–683 (2001).

[11] Mercier, J.-F. and Slater, G. W. "An exactly solvable ogston model of gel electrophoresis. 7. diffusion and mobility of hard spherical particles in three-dimensional gels". *Macromolecules* **34**, 3437–3445 (2001).

[12] Mercier, J.-F., Tessier, F., and Slater, G. W. "An exactly solvable ogston model of gel electrophoresis: VIII. nonconducting gel fibers, curved field lines, and the nernst-einstein relation". *Electrophoresis* **22**, 2631–2638 (2001).

[13] Ogston, A. G. "The space in a uniform random suspension of fibers". *Trans. Faraday Soc.* **54**, 1754–1756 (1958).

[14] Morris, C. J. O. R. *Protides of the Biological Fluids, 14th Colloquium.* Elsevier, New York, (1967).

[15] Rodbard, D. and Chrambach, A. "Unified theory of gel electrophoresis and gel filtration.". *Proc. Natl. Acad. Sci. USA* **65**, 970–977 (1970).

[16] Tietz, D. *Advances in Electrophoresis*, volume 2. VCH, Weinhei, (1988).

[17] Mercier, J.-F., Slater, G. W., and Guo, H. L. "Numerically exact diffusion coefficients for lattice systems with periodic boundary conditions. I. theory". *Journal of Chemical Physics* **110**, 6050–6056 (1999).

[18] Mercier, J.-F. and Slater, G. W. "Numerically exact diffusion coefficients for lattice systems with periodic boundary conditions. II. numerical approach and applications". *Journal of Chemical Physics* **110**, 6057–6065 (1999).

[19] Mercier, J.-F. and Slater, G. W. "Random walk and diffusion of hard spherical particles in quenched systems: Reaching the continuum limit on a lattice". *Journal of Chemical Physics* **113**, 9109–9112 (2000).

[20] Slater, G. W. "Theory of band broadening for dna gel electrophoresis and sequencing". *Electrophoresis* **14**, 1–7 (1993).

[21] Binder, K., editor. *Monte Carlo and Dynamics Simulations in Polymer Science.* Oxford University Press, (1995).

[22] Bortz, A. B., Kalos, M. H., and Lebowitz, J. L. "A new algorithm for monte carlosimulation of ising spin systems.". *Journal of Computational Physics* **17**, 10–18 (1975).

[23] Newman, M. E. J. and Barkema, G. T. *Monte Carlo Methods in Statistical Physics.* Clarendin Press, (1999).

[24] Griess, G. A. and Serwer, P. "Gel-electrophoresis of micron-sized particles - a problem and a solution". *Biopolymers* **29**, 1863–1866 (1990).

[25] Ernst, M. H., Nieuwenhuizen, T. M., and van Velthoven, P. F. J. "Density expansion of transport coefficients on a 2d site-disordered lattice. II". *J. Phys. A* **20**, 5335–5350 (1987).

[26] Amsden, B. "Solute diffusion within hydrogels. mechanisms and models". *Macromolecules* **31**, 8382–8395 (1998).

[27] Amsden, B. "An obstruction-scaling model for diffusion in homogeneous hydrogels". *Macromolecules* **32**, 874–879 (1999).

[28] Amsden, B. "Diffusion in polyelectrolyte hydrogels: Application of an obstruction-scaling model to solute diffusion in calcium alginate". *Macromolecules* **34**, 1430–1435 (2001).

[29] Serwer, P. and Griess, G. A. "Large particle gel-electrophoresis". *Analusis* **21**, M16 (1993).

[30] Griess, G. A., Harris, R. A., and Serwer, P. "The trajectories of spheres during agarose gel electrophoresis.". *Applied and Theoretical Electrophoresis* **3**, 305–315 (1993).

[31] Griess, G. A., Guiseley, K. B., and Serwer, P. "The relationship of agarose-gel structure to the sieving of spheres during agarose-gel electrophoresis". *Biophysical Journal* **65**, 138–148 (1993).

[32] Serwer, P., Khan, S. A., and Griess, G. A. "Nondenaturing gel-electrophoresis of biological nanoparticles - viruses". *Journal of Chromatography A* **698**, 251–261 (1995).

[33] Griess, G. A., Rogers, E., and Serwer, P. "Application of the concept of an electrophoretic ratchet". *Electrophoresis* **22**, 981–989 (2001).

[34] To, K.-Y. and Boyde, T. R. C. "Pulsed-field acceleration - the electrophoretic behavior of large spherical-particles in agarose gels". *Electrophoresis* **14**, 597–600 (1993).

[35] Bouchaud, J.-P. and Georges, A. "Anomalous diffusion in disordered media - statistical mechanisms, models and physical applications". *Physics Reports* **195**, 127–293 (1990).

[36] Russel, W. B., Saville, D. A., and Schowalter, W. R. *Colloidal Dispersions*. Cambridge University Press, New York, (1995).

[37] Turner, S. W. P., Cabodi, M., and Craighead, H. G. "Confinement-induced entropic recoil of single dna molecules in a nanofluidic structure". *Physical Review Letters* **88**, 128103 (2002).

[38] Serwer, P. and Griess, G. A. "Adaptation of pulsed-field gel electrophoresis for the improved fractionation of spheres". *Analytica Chimica Acta* **372**, 299–306 (1998).

[39] Brody, J. P., Yager, P., Goldstein, R. E., and Austin, R. H. "Biotechnology at low reynolds numbers". *Biophysical Journal* **71**, 3430–3441 (1996).

[40] Austin, R. H. and Volkmuth, W. D. "Dna electrophoresis in microlithographic arrays". *Nature* **358**, 600–602 (1992).

[41] Duke, T. A. J. and Austin, R. H. "Microfabricated sieve for the continuous sorting of macromolecules". *Physical Review Letters* **80**, 1552–1555 (1998).

[42] Chou, C.-F., Bakajin, O., Turner, S. W. P., Duke, T. A. J., Chan, S. S., Cox, E. C., Craighead, H. G., and Austin, R. H. "Sorting by diffusion: An asymmetric obstacle course for continuous molecular separation". *PNAS* **96**, 13762–13765 (1999).

[43] Austin, R. H., Darnton, N., Huang, R., Sturm, J., Bakajin, O., and Duke, T. "Ratchets: the problems with boundary conditions in insulating fluids". *Applied Physics A* **75**, 279–284 (2002).

[44] Cowan, G. *Statistical Data Analysis*. Clarendon Press, Oxford, (1998).

[45] Hoagland, D. A., Arvanitidou, E., and Welch, C. "Capillary electrophoresis measurements of the free solution mobility for several model polyelectrolyte systems". *Macromolecules* **32**, 6180–6190 (1999).

[46] Derenyi, I. and Astumian, R. D. "ac separation of particles by biased brownian motion in a two-dimensional sieve". *Physical Review E* **58**, 7781–7784 (1998).

[47] Ertas, D. "Lateral separation of macromolecules and polyelectrolytes in microlithographic arrays". *Physical Review Letters* **80**, 1548–1551 (1998).

[48] Starchev, K., Sturm, J., and Weill, G. "Brownian motion and electrophoretic transport in agarose gels studied by epifluorescence microscopy and single particle tracking analysis". *Journal of Physical Chemistry B* **101**, 5659–5663 (1997).

[49] Guo, H. L. *Sieving of Spherical Particles during Gel electrophoresis: A New Computer simulation Algorithm.* Master's thesis, University of Ottawa, (1994).

[50] Keller, C., Marquardt, F., and Bruder, C. "Separation quality of a geometric ratchet". *Physical Review E* **65**, 041927 (2002).

[51] Tamada, K., Kim, S., and Yu, H. "Lateral diffusion of probe lipid in biphasic phospholipid monolayers: Liquid/gas coexistence films". *Langmuir* **9**, 1545–1550 (1993).

[52] Dietrich, C., an T. Fujiwara, B. Y., Kusumi, A., and Jacobson, K. "Relationship of lipid rafts to transient confinement zones detected by single particle tracking". *Biophysical Journal* **82**, 274–284 (2002).